

ENGR 445: Leadership in Technology

**LOFT-E® Raised Loft Leg Strength, Stress and Thermal
Simulation Tests**

**In collaboration with Cumbria Loft Boarding (part of UK Loft
Boarding Ltd)**

Names:

Cole Chesterton

Naeem Khan

Harrison Beaumont

Mackenzie Clark

Greg Wray

Supervisor: Professor Jianqiao Ye

Submission Date: 17/03/2021

Executive Summary

Cumbria Loft Boarding requested that analysis of the LOFT-E be conducted, assessing both the mechanical and thermal performance of the component, such that maximum operational conditions could be identified and further recommend improvements to the design. This report contains of a comprehensive documentation of the process utilised in delivering the data needed for the company's request and all resulting data. Upon successful analytical processing, both mechanical and thermal data yielded useful information regarding maximum limitations and areas of improvement. Regarding the mechanical performance, it was shown that the current design operates safely in a loft space environment with compressive loading capabilities of significant magnitudes. However, bending stress showed a significant drop in performance and low factor of safety, thus suggesting an area for further investigation and physical testing. Furthermore, other materials were applied to the component design assessing both thermal and mechanical performance. As a result, other materials were suggested for utilisation in the component. Materials identified as suitable alternatives were; Stainless Steel 316, as it demonstrated superior heat retention, and Low Alloy Steel, for demonstrating significantly improved performance regarding loading and bending capabilities.

Contents

Executive Summary	i
List of Figures	iv
List of Tables	vi
1. Introduction	1
2. Literature Review	1
2.1. Loft Insulation	1
2.2. Thermal Regulations	3
2.3. Materials	3
3. Component Replication and Rendering	4
3.1. 3D Model and Render	4
4. Mechanical Aspects	7
4.1. Mesh	7
4.1.1. Mesh Generation	7
4.1.2. Mesh Refinement	8
4.2. Yield Stress Analysis	11
4.2.1. Simulation Set Up	11
4.2.2. Boundary Conditions	12
4.3. Results	12
4.3.1. Maximum Equivalent Stress	12
4.3.2. Whole Body	13
4.3.3. Threaded Rod	15
4.3.4. Maximum Deformation	16
4.3.5. Discussion	17
4.4. Maximum Loading Conditions for an Array	17
4.5. Stability Analysis	19
4.6. Stress Due to Bending	20
4.6.1. Loading Scenario	20
4.7. Results	21
4.7.1. Maximum Equivalent Stress	21
4.7.2. Discussion	22
4.8. Recommendations/Design Optimisation	23
4.8.1. Different Material Simulations	23
4.8.2. Material Selection for Bending Optimisation	33
5. Thermal Aspects	35
5.1. Mesh	35

5.1.1.	The Simulation Concept	35
5.1.2.	Mesh Generation and Refinement	36
5.2.	Steady State Thermal	39
5.2.1.	Boundary Conditions and Configuration	39
5.2.2.	Simulation Results	41
5.2.3.	Design Optimisation	45
5.3.	Thermal Expansion.....	49
5.4.	Thermal Stress.....	50
5.5.	Numerical Calculations	54
5.5.1.	Steady-State Thermal Calculations.....	54
5.6.	Further Thermal Simulation- Ambient Temperatures and Directional Heat Flux	55
5.6.1.	Motivation and Methodology.....	55
5.6.2.	Results	56
5.6.3.	Calculations and U values.....	59
5.7.	Maximum Thermal Conductivity Calculation.....	60
5.8.	Recommendations/Design Optimisation.....	62
6.	Concluding Statement and Suggestions of Further Work	62
7.	Reflection	63
8.	References	65
9.	Appendices.....	67
	Appendix A – Loft-E drawing.....	67
	Appendix B – Work Breakdown Structure	68
	Appendix C – Gantt Chart	69
	Appendix D – Presentation Slides	70
	Appendix E – Initial Meeting Agenda.....	81

List of Figures

- Figure 1: Typical Installation Cost of Loft Insulation (OVO Energy, 2020)
- Figure 2: Carbon Dioxide Saving per Year with Loft Insulation (OVO Energy, 2020)
- Figure 3: Energy Bill Savings per Year with Loft Insulation (OVO Energy, 2020)
- Figure 4: LOFT-E Leg Parts/Features.
- Figure 5: Rendered 3D model
- Figure 6: Steady-state thermal FEA model
- Figure 7: Static structural FEA model
- Figure 8: Initial mesh of support with hexagonal boss
- Figure 9: Boundary conditions applied to structure
- Figure 10: Convergence history of maximum stress through mesh refinement of hexagonal boss model
- Figure 11: Convergence history of maximum deformation through mesh refinement of hexagonal boss model
- Figure 12: Simplified support geometry
- Figure 13: Convergence history of maximum stress through mesh refinement of cylindrical boss model
- Figure 14: Boundary conditions applied to support
- Figure 15: Maximum stress experienced by the whole structure when loaded from 0-10000N (structural steel)
- Figure 16: Stress contours on the base of the saddle
- Figure 17: Stress contours on the top of the saddle
- Figure 18: Stress contours of the whole body
- Figure 19: Maximum stress experienced by the rod when loaded from 0-10000N (structural steel)
- Figure 20: Maximum deformation experienced by the whole body and the rod for loading conditions of 0-10000N (structural steel)
- Figure 21: Deformation contour plots of whole body (left) and isolated rod (right)
- Figure 22: Maximum allowable load for an array of legs
- Figure 23: Maximum allowable mass for an array of legs
- Figure 24: Bending loading scenario
- Figure 25: Boundary conditions of bending loading
- Figure 26: Stress distribution from bending loading on the whole body and isolated rod
- Figure 27: Location of maximum stress from bending loading
- Figure 28: Maximum stress experienced when additional loading is applied away from the geometry
- Figure 29: Maximum stress experienced by the whole structure when loaded from 0-10000N (bronze)
- Figure 30: Maximum stress experienced by the rod when loaded from 0-10000N (bronze)
- Figure 31: Maximum deformation experienced by the whole body and the rod for loading conditions of 0-10000N (bronze)
- Figure 32: Maximum stress experienced by the whole structure when loaded from 0-10000N (carbon steel)
- Figure 33: Maximum stress experienced by the rod when loaded from 0-10000N (carbon steel)
- Figure 34: Maximum deformation experienced by the whole body and the rod for loading conditions of 0-10000N (carbon steel)
- Figure 35: Maximum stress experienced by the whole structure when loaded from 0-10000N (low alloy steel)
- Figure 36: Maximum stress experienced by the rod when loaded from 0-10000N (low alloy steel)

Figure 37: Maximum deformation experienced by the whole body and the rod for loading conditions of 0-10000N (low alloy steel)

Figure 38: Maximum stress experienced by the whole structure when loaded from 0-10000N (stainless steel)

Figure 39: Maximum stress experienced by the rod when loaded from 0-10000N (stainless steel)

Figure 40: Maximum deformation experienced by the whole body and the rod for loading conditions of 0-10000N (stainless steel)

Figure 41: Maximum stress experienced by the whole structure when loaded from 0-10000N (titanium alloy)

Figure 42: Maximum stress experienced by the rod when loaded from 0-10000N (titanium alloy)

Figure 43: Maximum deformation experienced by the whole body and the rod for loading conditions of 0-10000N (titanium alloy)

Figure 44: Comparison of uniform and non-uniform loading for stainless steel

Figure 45: Comparison of uniform and non-uniform loading for low alloy steel

Figure 46: Factor of safety comparison for different materials subjected to non-uniform loading

Figure 47: Block diagram for intended model simulation

Figure 48: CAD model and default mesh application

Figure 49: Final meshing of component

Figure 50: Thermal model conditions configuration

Figure 51: Thermal model temperature results (with insulation layer)

Figure 52: Thermal model temperature results (hidden insulation layer)

Figure 53: Direction of total heat flux through component

Figure 54: Thermal error in the model

Figure 55: Thermal distributions for a range of temperature differentials

Figure 56: Thermal distributions for isolated component

Figure 57: Temperature distribution results for the range of selected material applications

Figure 58: Temperature distribution results for the range of selected material applications

Figure 59: Labelled sampling probe points for data comparison

Figure 60: Temperature differential results from sample points

Figure 61: Total Deformation of Loft Support without attachments

Figure 62: Total Deformation of Loft Support with attachments

Figure 63: Equivalent Stress of Loft Support Without Attachments

Figure 64: Close up of rod with saddle hidden.

Figure 65: Equivalent Stress of Loft Support With Attachments

Figure 66: Equivalent Stress Close-Up of Saddle.

Figure 67: Temperature at Each Point in the Geometry Compared to Distance.

Figure 68: Temperature and directional heat flux simulations on eight materials of decreasing thermal conductivity: copper, structural steel, carbon steel, low alloy steel, stainless steel, titanium alloy, concrete and HDPE. Temperature left, heat flux right

List of Tables

Table 1: Mechanical Properties of Common Steel Types (Tubecon, n.d.)

Table 2: Mesh metric details

Table 3: Material properties of structural steel

Table 4: Initial mesh statistics

Table 5: Details of iterations

Table 6: Statistical changes of mesh through iterations

Table 7: Material assignment and properties

Table 8: Isolated component meshing statistics

Table 9: Material properties of chosen material range

Table 10: Material thermal performance data

Table 11: Thermal conductivity and average directional heat flux data for different materials

Table 12: U values for different materials

Table 13: Thermal conductivity, average directional heat flux and final U value data for each material

Table 14: U values for simulated supports with a range of thermal conductivities

1. Introduction

Cumbria Loft Boarding specialises in the construction of loft space for residential homes, including both old and new build homes. The company has created a new product, titled the LOFT-E adjustable loft leg. The product is unique in its ability to be applied to loft spaces in which the flooring and foundational supports are not entirely linear or flat in the horizontal plane. Observations made within the industry, due to uneven ceiling surface, have noted results such as the tearing of the ceiling plasterboard upon drilling the foundational timbers or having to crudely even the surface by packing further material into empty space. This is not an overly efficient method, leading to the LOFT-E being created. However, with the newness of this product the company lacked a large variety of data to include in the marketing of this component, with physical testing postponed due to the COVID-19 pandemic. Consequently, the company requested initial analysis of the component regarding mechanical and thermal properties.

The purpose of this report is to analyse the suitability of the LOFT-E adjustable loft leg for its use in loft spaces. This analysis is split into two main parts: mechanical analysis and thermal analysis. The mechanical section contains yield stress analysis, stability analysis and bending analysis, in addition to finding the maximum loading conditions for an array of supports. The thermal portion of this report investigates the thermal expansion, thermal stress, and heat transfer properties of the design. A range of materials have been investigated to find potential alternative materials for future designs. The analysis in this report is based on simulations and numerical calculations and the results have been used to make recommendations for design improvements and future testing.

2. Literature Review

Energy efficiency is an important factor in housing as these can determine the heating costs. Having a high energy efficiency will help lower those heating costs thus, research into what allows these costs to be lowered is carried out as well as understanding the most appropriate material to use in supporting the loft boards as well as maintaining heat well within the material.

2.1. Loft Insulation

These are essentially barriers of material within roof space which can be laid between the joists or the rafters. This is to slow heat transfer between living space and outside world which allows a warmer home during colder periods.

Insulation between the joists keeps warmth in living space below creating a cold loft while insulation in the rafters keep warmth in the roof space creating a warmer loft.

Benefits of roof insulation include:

- Lowers heating bills
- Improve energy efficiency
- Increase home value
- Reduced carbon footprint due to more efficient heating system

A quarter of the heat is lost through the roof thus having insulation in the loft reduces that amount of heat loss and they last long for a long time helping to pay off the energy bill savings since the cost of loft insulation is low.

Figure 1 Figure 2 and Figure 3 show the benefits of installing loft insulation of up to 270mm (OVO Energy, 2020).

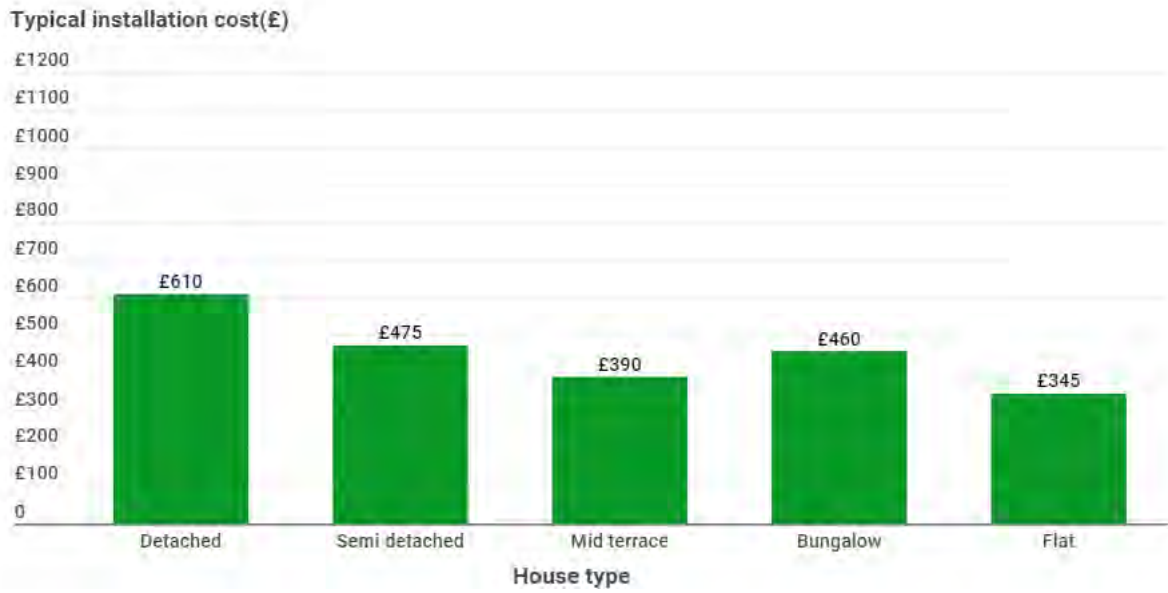


Figure 1: Typical Installation Cost of Loft Insulation (OVO Energy, 2020)

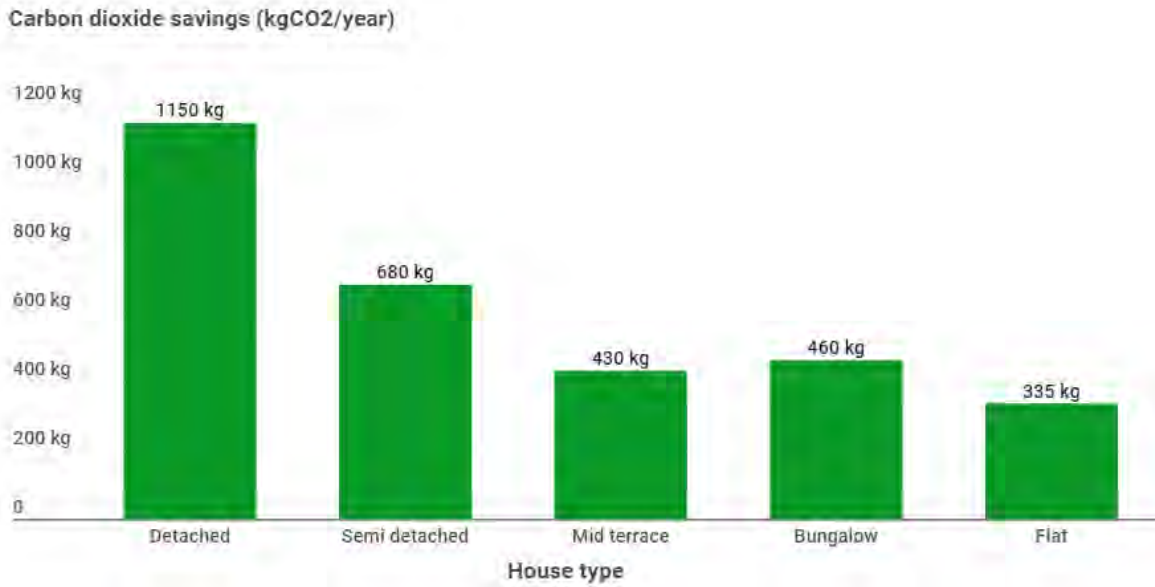


Figure 2: Carbon Dioxide Saving per Year with Loft Insulation (OVO Energy, 2020)

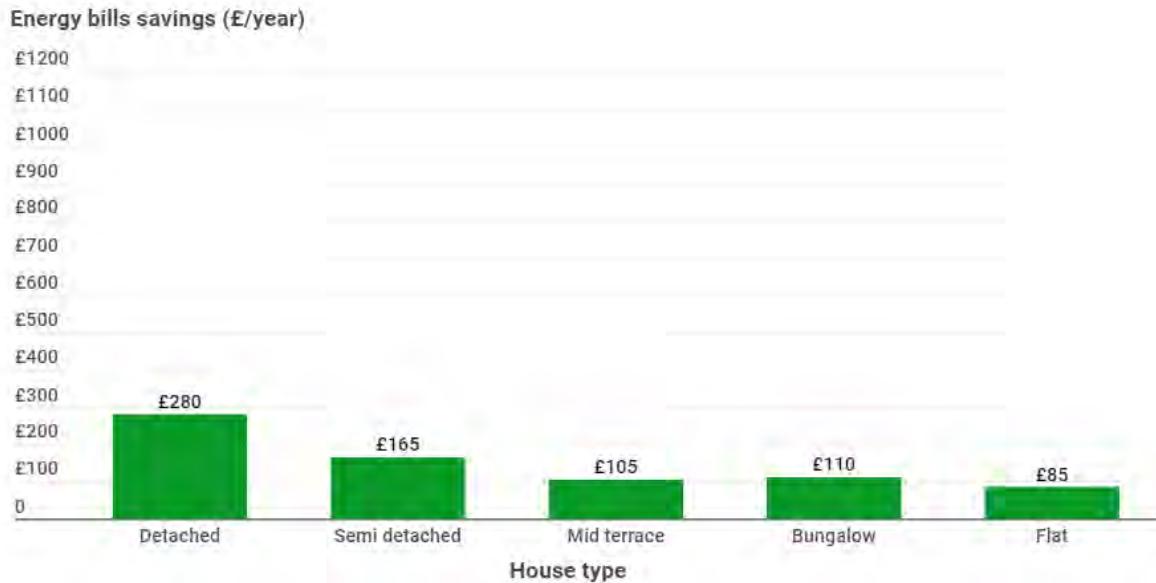


Figure 3: Energy Bill Savings per Year with Loft Insulation (OVO Energy, 2020)

It may seem expensive at first to install loft insulation but as Figure 3 shows, the energy saving per year will eventually surpass the installation cost after around about 3-4 years' time.

Care must be taken however to ensure that the insulation is not squashed otherwise the effectiveness of the insulation will reduce and this can also lead into condensation which results in damp and mould. (Roofing Superstore, n.d.)

2.2. Thermal Regulations

Since 2003, regulations for loft insulation require the material to be at least 270mm thick. This is a way to ensure larger savings. Whereas 1995, the recommended depth was 200mm and before that it was 100mm thus the correlation of increasing thickness of insulation to ensure better energy savings was positive. (Evergreen Energy, n.d.)

U-Values indicate the level of heat loss within a material. The lower the U-value, the lower the heat loss. Current regulations for new buildings that the roof element must have a maximum U-value of $0.16\text{W/m}^2\text{K}$. Without insulation, the U-value is approximately $2.5\text{W/m}^2\text{K}$ indicating a very large amount of heat loss and with the recommended thickness of 270mm insulation, fibreglass or Knauf space blanket can be used to reduce the U-value to its targeted value of $0.16\text{W/m}^2\text{K}$. (The Greenage, 2013)

2.3. Materials

Commonly used material for loft insulation is fibreglass which is a plastic matrix reinforced by tiny glass fibres. This makes the material lightweight and strong. As fibreglass is a good insulator, it reduces the effect of conductive heat transfer meaning the transfer of heat through solid objects. Fibreglass traps heat when it moves to a colder area (outside to inside the house in summer and from inside to outside the house in winter). (Tidewater Insulators, 2014)

The Loft-E device is made of a structural steel which is typically a strong material in holding the floor platform of the loft in place without squashing the insulation material which would hinder its function of reducing heat transfer. Material properties of steel are as listed below.

- High tensile and yield strength
- Low weight
- Durable
- Ductile
- Resistant to corrosion

(Total Materia, n.d.)

Common types of steel shown in Table 1 could be useful in this sort of application to withstand a large load. These document the yield strength which would be important in understanding if the material can withstand the loading in the loft environment via simulations. In addition, simulation of thermal properties would also be useful in understanding how heat transfer is performed within the material allowing comparisons to be drawn up which would further help in recommending which material is acceptable to use.

Table 1: Mechanical Properties of Common Steel Types (Tubecon, n.d.)

Material properties		SAE1010	SAE1008	SAE1012	S00WA	JISGV132	DD11	S355	S235	S275	Corten_A
Tensile strength, ultimate (Mpa)	min	310	303		300	390		490	340	410	470
Tensile strength, ultimate (Mpa)	max	360	358	370		540	440	530	470	560	630
Tensile strength, Yield (Mpa)	min	180	180		160		170	355	235	275	
Tensile strength, Yield (Mpa)	max	240	240	310	320	270	340				355
Elongation Break in (%)	at min	32	42					12	17	14	
Elongation Break in (%)	at max	48	48	19	20	25	23	22	26	22	29
Modulus of Elasticity, GPA		200	200	205							

3. Component Replication and Rendering

3.1. 3D Model and Render

The first and most geometrically accurate CAD model was created on SolidWorks from a 2D technical drawing provided by UK Loft Boarding Ltd. This model consists of four parts: the saddle, boss, rod, and the foot. The saddle and foot are constructed from 3mm sheet steel which is bent at a 90 angle to support the timber flooring. The saddle supports an area of 100mm by 45mm whereas the foot sits on an area half that size 50mm by 45mm.

Connecting the saddle and foot together are the boss and rod which is where the stress of the loft load is concentrated. The boss and rod provide the adjustability of the leg as the rod can retract into the boss and into the saddle due to the threading. Welding is used to join the boss to the saddle whereas the rod

is connected to the foot by a M10 welded nut. A feature of the boss shown in Figure 4 is the 5mm view hole which is used to determine when the rod is at full extension.

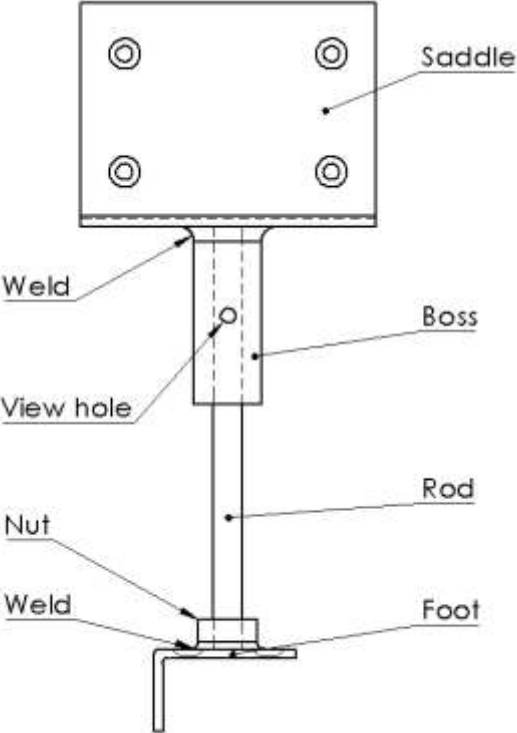


Figure 4: LOFT-E Leg Parts/Features.



Figure 5: Rendered 3D model

To prevent any error singularities in each of the simulations, the model was simplified. This simplification consisted of replacing the hexagonal boss geometry with a cylindrical tube-based model. Due to the model being simplified, the FEA meshing process was improved to give an accurate convergence plot. For the thermal and mechanical simulations, a different model was used to generate the most accurate results.

Figure 6 displays the model used for the steady-state thermal analysis. This CAD model comprises of the floor, timber, insulation, and LOFT-E leg components.

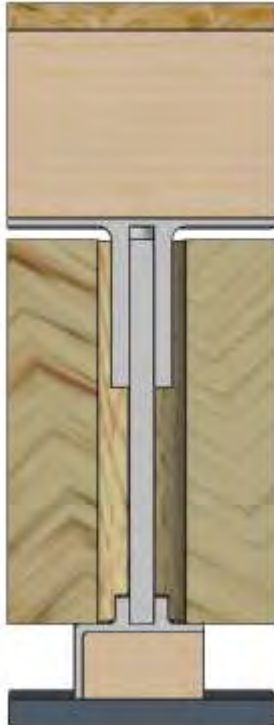


Figure 6: Steady-state thermal FEA model

The static structural mechanical model as shown in Figure 7 is a variation of the thermal model however there is no insulation, the saddle is hexagonal, and the floor timber has been extended to represent how the load would be induced at the top of the leg.



Figure 7: Static structural FEA model

4. Mechanical Aspects

4.1. Mesh

4.1.1. Mesh Generation

To carry out analysis on the loading of the support it was first necessary to generate a high-quality mesh of the component. A mesh with high element quality, low skewness and a low aspect ratio would be required to produce reliable results during loading simulations. ANSYS static structural was used to produce a mesh of the 3D computer generated model of the support. An initial mesh was generated using the default element size (13.523mm) and settings provided in static structural. The resultant mesh was coarse with large elements and unrefined around key features such as the weld between the saddle and boss (Figure 8).

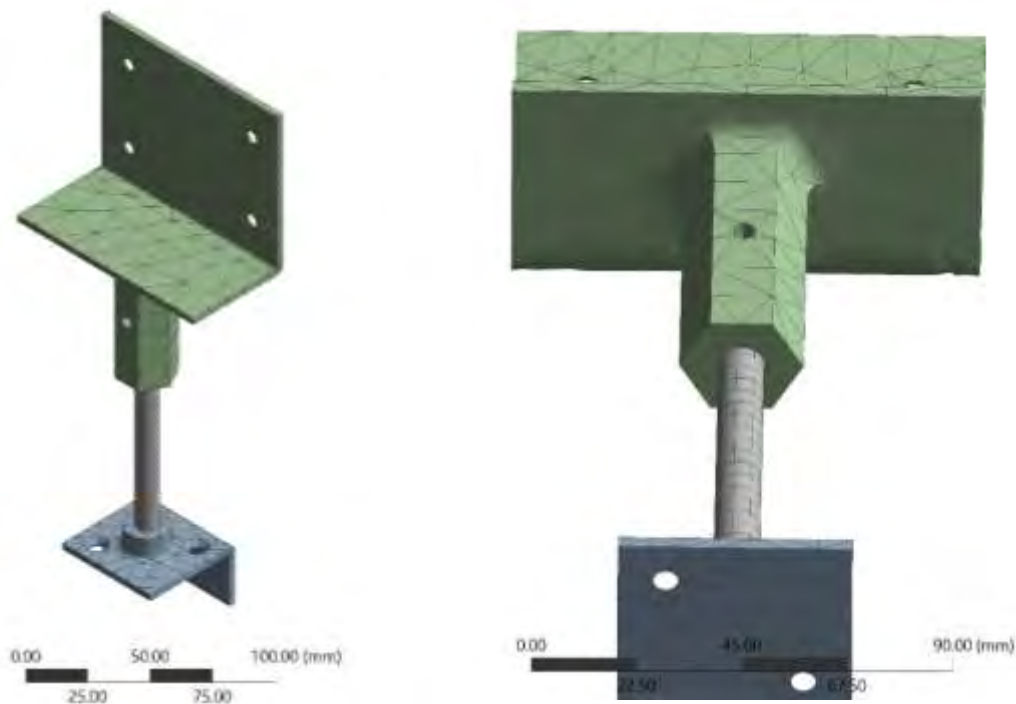


Figure 8: Initial mesh of support with hexagonal boss

The mesh was comprised of 8034 nodes and 3063 elements with an average element quality of 0.54. It was clear from these statistics that the mesh needed to be refined before any simulations could take place. Therefore, the overall element sizing of the model was decreased and various refinement methods such as decreased edge sizing around areas of interest were implemented. This produced a mesh with an improved element quality of 0.68.

The boundary conditions of the fixed supports and force applied to the saddle were assigned as can be seen in Figure 9.

B: Static Structural

Static Structural

Time: 1. s

08/03/2021 10:21

- A** Force: 4000. N
- B** Fixed Support



Figure 9: Boundary conditions applied to structure

4.1.2. Mesh Refinement

Loading simulations were carried out on the structure whilst simultaneously refining the mesh to produce a successively finer mesh with each simulation. The maximum stress and deformation of the structure were recorded along with the total number of elements for each simulation. As the mesh is refined and becomes finer the total number of elements increases and the result should become more accurate, ultimately converging to a final value. The results of these tests are plotted in Figure 10.

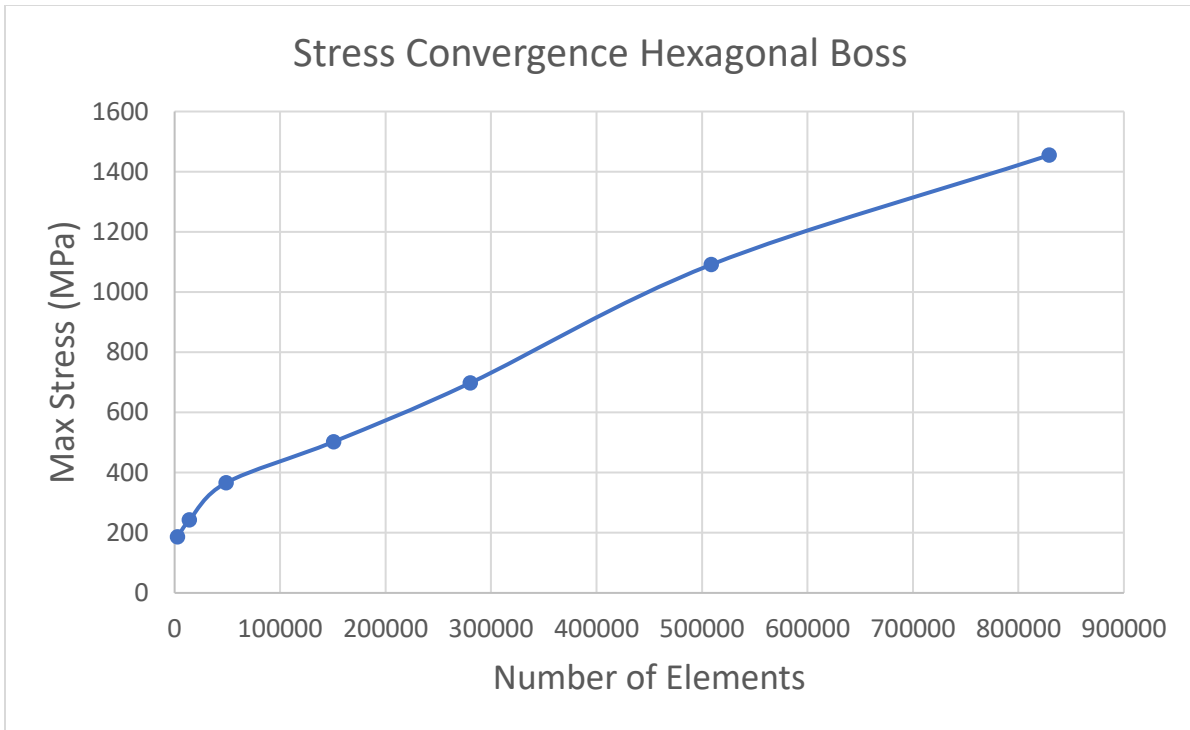


Figure 10: Convergence history of maximum stress through mesh refinement of hexagonal boss model

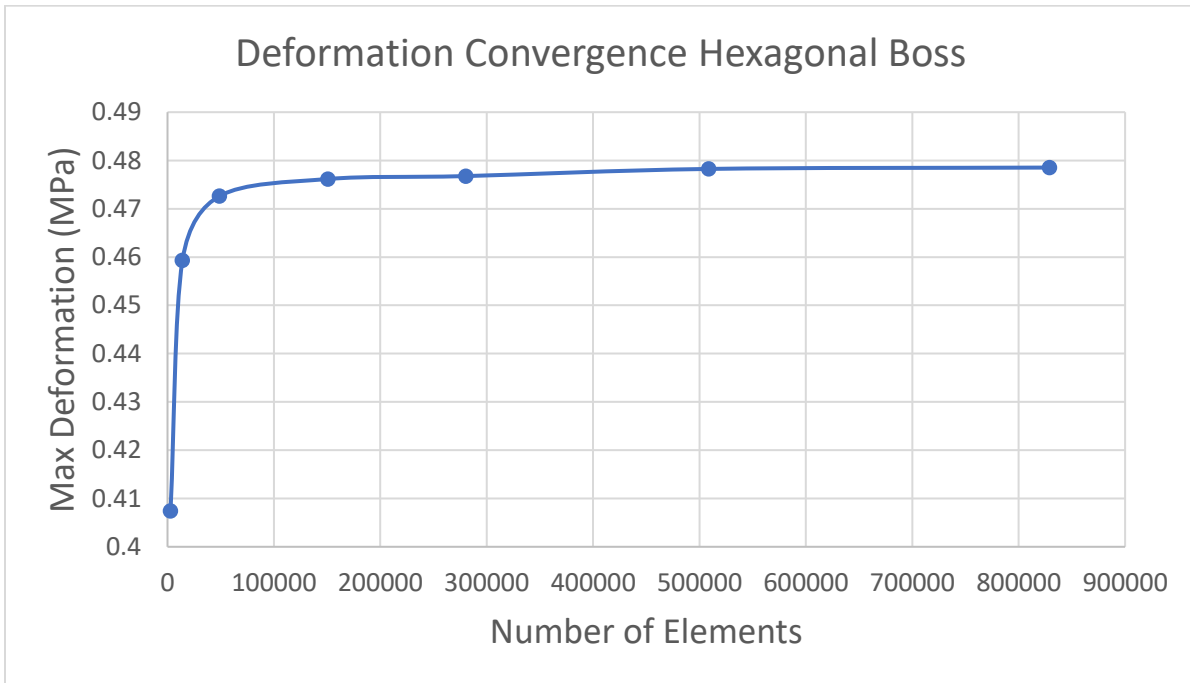


Figure 11: Convergence history of maximum deformation through mesh refinement of hexagonal boss model

The results clearly show that the maximum stress experienced by the support does not converge as the mesh is refined. However, the maximum deformation does converge suggesting that the reason for this was that various stress singularities were present on the body. These can occur for a variety of reasons,

one of which is due to sharp corners. In this model there are sharp corners in both the hexagonal boss and the way the boss was welded to the saddle.

Therefore, the model was edited to replace the hexagonal boss with a cylindrical version and similarly the weld was modelled to reflect this change. Furthermore, since initial consultation with the company we discovered that the threaded rod could pass through the saddle via a hole in its centre, this modification was also made. Finally, after meeting with our project supervisor and discussing the issue of stress singularities it was suggested to remove the back plate of the saddle as this had little significance in the structural stability of the support. This is represented in Figure 12. This modification also reduced the computational power needed to run the simulation and allowed us to focus our attention on the main areas of interest of the support.



Figure 12: Simplified support geometry

The same boundary conditions as described above were applied and the simulation was re-run to see if the maximum stress converged. The results of this simulation can be seen in Figure 13.

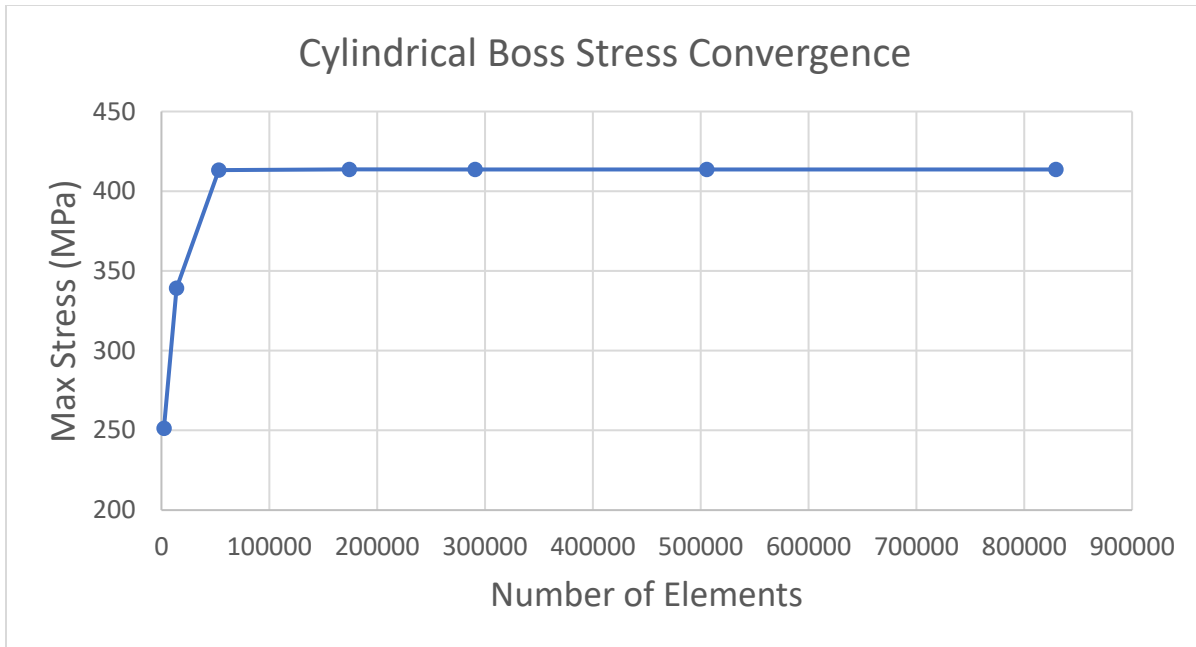


Figure 13: Convergence history of maximum stress through mesh refinement of cylindrical boss model

This new model can be seen to converge as the mesh is refined meaning no stress singularities were present and the model could be used to produce reliable results.

The final mesh used for further mechanical simulations had the following mesh metrics from Table 2:

Table 2: Mesh metric details

Nodes	187240
Elements	63741
Element Quality	0.88127
Aspect Ratio	1.5713
Skewness	0.19676

Having proved that a high-quality mesh had been generated that produced accurate and reliable results, static structural analysis of the support could be assessed.

4.2. Yield Stress Analysis

Using the mesh and model produced in the verification section of this report, loading conditions were applied to assess the failure criteria of the support. A force was applied to the top face of the saddle to replicate the force exerted by the timber it would support. This force was increased from 0N to 10000N in increments of 500N, the equivalent stress and total deformation were recorded for each of these tests along with the factor of safety.

4.2.1. Simulation Set Up

The 3D geometry was loaded into ANSYS Static Structural and the material of all bodies was assigned as structural steel, with the following properties in Table 3:

Table 3: Material properties of structural steel

Young's Modulus (MPa)	2e+05
Poisson's Ratio	0.3
Bulk Modulus (MPa)	1.6667e+05
Shear Modulus (MPa)	76923
Isotropic Secant Coefficient of Thermal Expansion (°C-1)	1.2e-05
Compressive Ultimate Strength (MPa)	0
Compressive Yield Strength (MPa)	250

4.2.2. Boundary Conditions

Following the method of the convergence tests conducted previously, the boundary conditions were applied to the same faces of the body as in Figure 14. However, the force applied to the top face of the saddle was replaced with a load that increased with time.



Figure 14: Boundary conditions applied to support

For these simulations, the threaded rod was modelled as a smooth rod to reduce computational time and improve the quality of the mesh. This decision was made as the presence of a thread would have little to no significance on the failure of the overall support. Furthermore, this rod was modelled to be flush with the top of the saddle where the load was applied.

4.3. Results

4.3.1. Maximum Equivalent Stress

To determine if the structure would fail the maximum stress experienced by the body was recorded. Knowing the material properties of structural steel, this value was then compared to the yield stress. If the stress experienced by the support exceeded this value, then these regions would plastically deform

meaning they would not return to their original dimensions when the load was removed. Hence, the structural stability of the support would be compromised, and it would be no longer fit for purpose. Both the maximum stress experienced by the whole body and the (threaded) rod were examined, the rod was isolated as it had the smallest cross-sectional area and was flagged as a potential weak spot.

4.3.2. Whole Body

Having applied a varying load from 0-10000N, the maximum stress experienced by the body was plotted for each loading case in Figure 15.

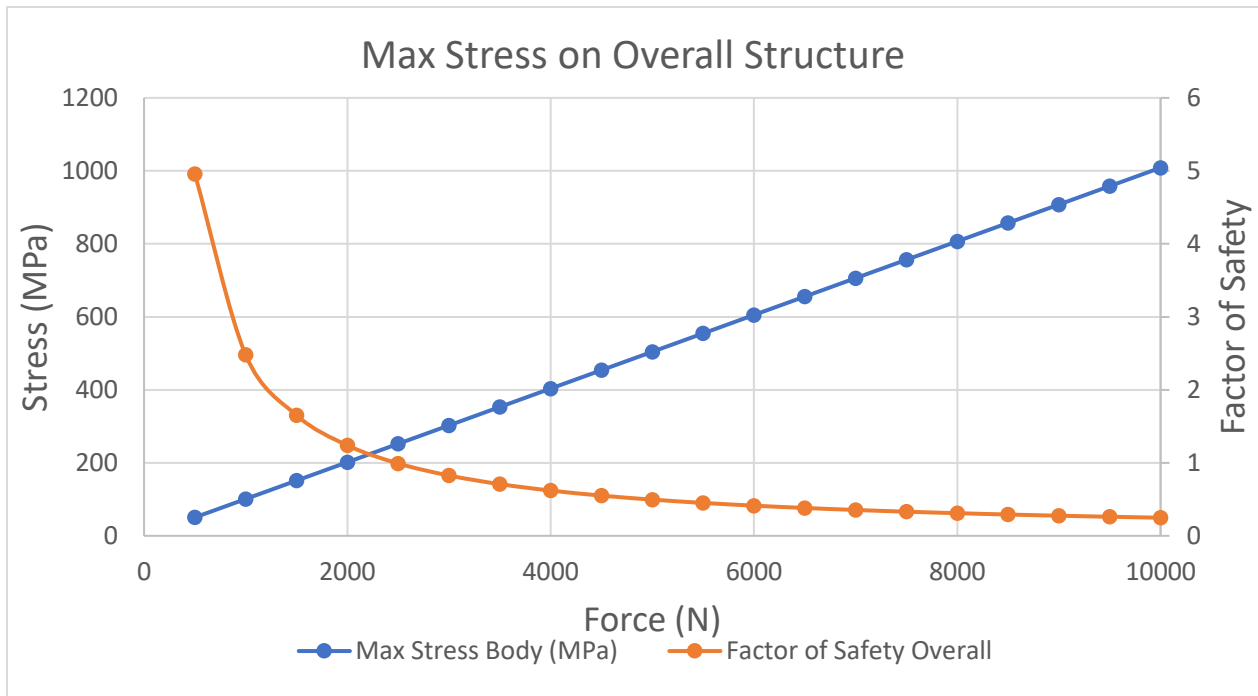


Figure 15: Maximum stress experienced by the whole structure when loaded from 0-10000N (structural steel)

Figure 15 above shows a linear increase in the stress experienced by the body which was to be expected as it is proportional to the applied load. Plotted on the same figure is the factor of safety for each loading case, for instance when 500N is applied, the factor of safety is approximately 5. As a result, the maximum stress experienced by the body is equal to 5 times the yield stress of the material. This value rapidly decreases and falls below 1 after 2500N is applied, showing that the structure has yielded and will then plastically (permanently) deform.

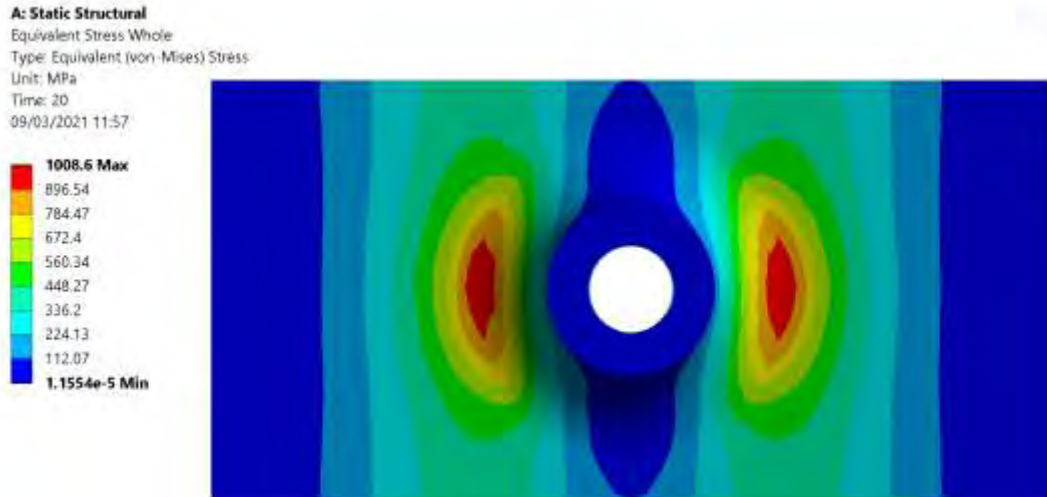


Figure 16: Stress contours on the base of the saddle

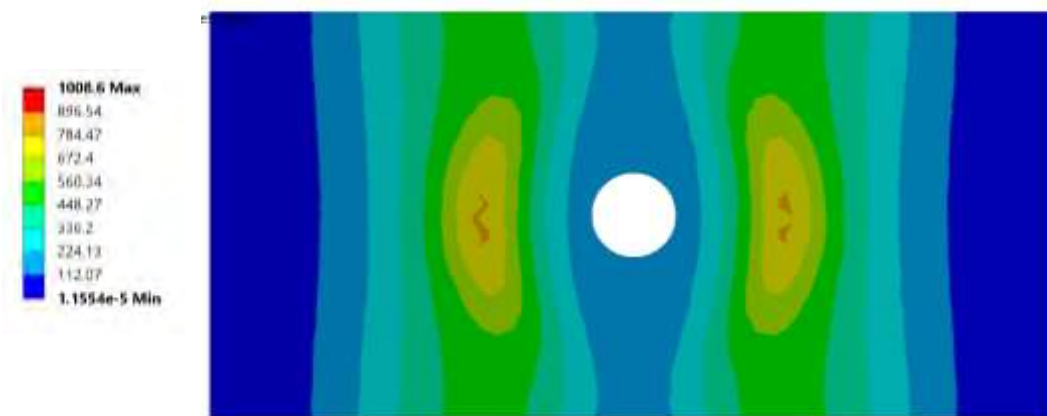


Figure 17: Stress contours on the top of the saddle

By examining the stress contours generated in ANSYS Static Structural, the location of these regions can be determined and therefore, weak areas can be identified. In this model the maximum stress experienced by the body occurs in the areas marked in red. Figure 16 and Figure 17 show that the locations of these high stress areas.

As can be seen from the above figures the stress around the weld connecting the boss to the saddle is the highest in the entire model. This is due to the transition of geometry between the base of the saddle which is a wide flat plate to the narrow cross section of the boss.

The overall stress contour plot is shown in Figure 18. The results of this simulation show that relative to the area surrounding the weld, the stress experienced by the body is relatively low and that the main area of concern is this connection.

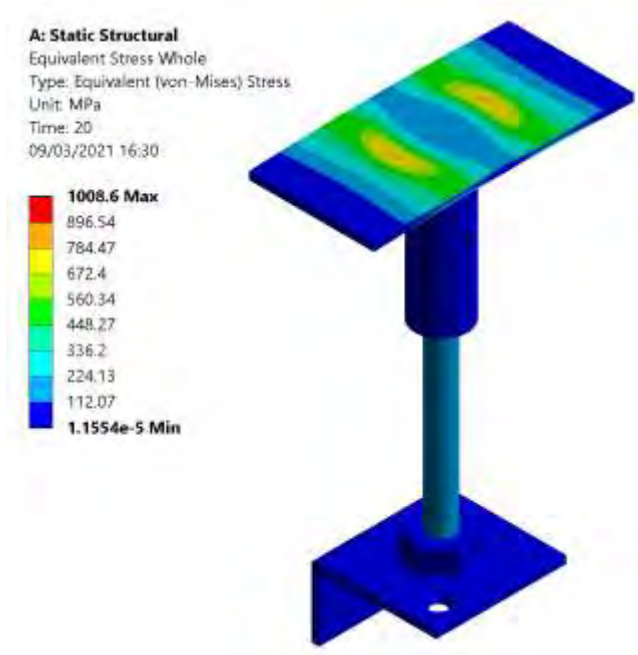


Figure 18: Stress contours of the whole body

4.3.3. Threaded Rod

The second area investigated was the threaded rod due to its narrow cross section and long length relative to other components. The rod was isolated from the simulation and the maximum stress for each loading case was recorded in Figure 19.

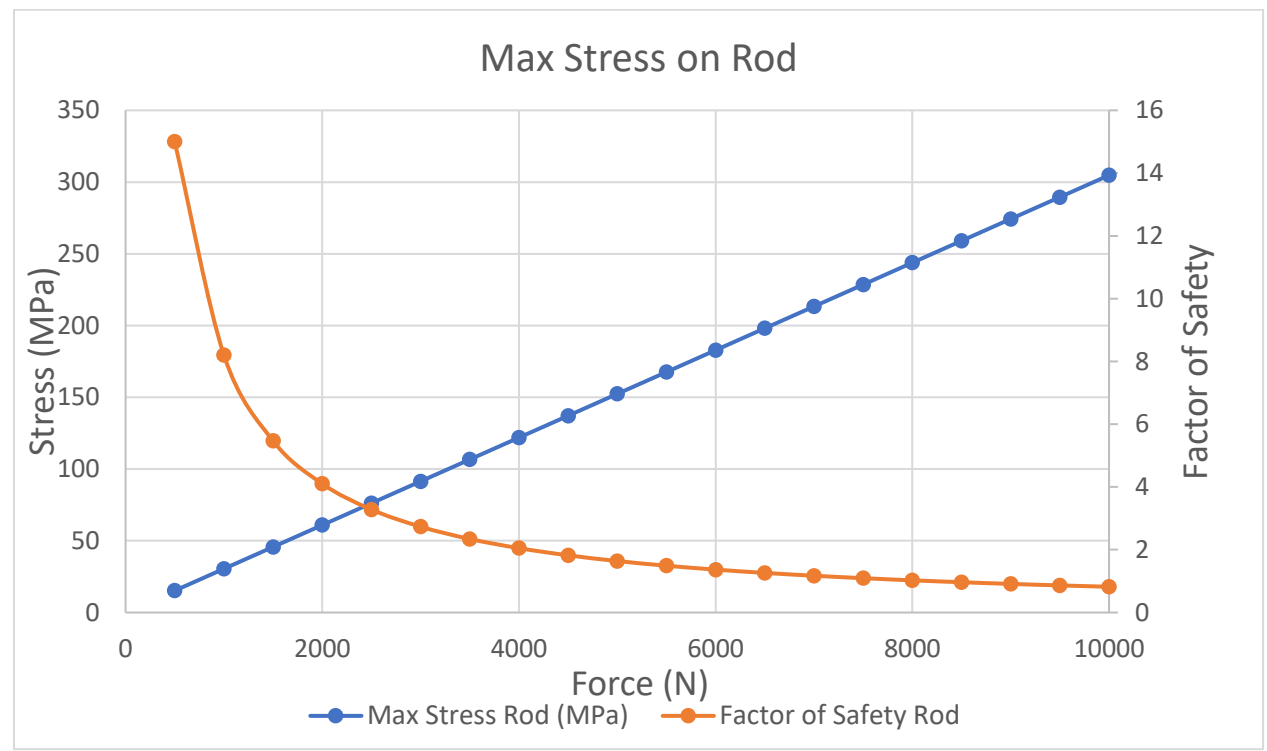


Figure 19: Maximum stress experienced by the rod when loaded from 0-10000N (structural steel)

The stress-force relationship follows the same pattern as the whole body, showing a linear increase in maximum stress as the force applied rises. The main difference between the two plots is the magnitude of the stress experienced by the rod is much lower than that experienced by the whole model. This is due to the area surrounding the weld not being considered. The figure above shows that the rod will not yield until a force of 8000N is surpassed, meaning that prior to this point the material will not permanently deform when a load is removed.

4.3.4. Maximum Deformation

An important physical characteristic to be considered was the deformation or change in position of components of the assembly. Therefore, the overall deformation of the body and rod were considered to see if a noticeable change in geometry could happen as a result of loading.

The same loading conditions as above were applied and the maximum deformation of the whole body and rod were plotted against the increasing load in Figure 20.

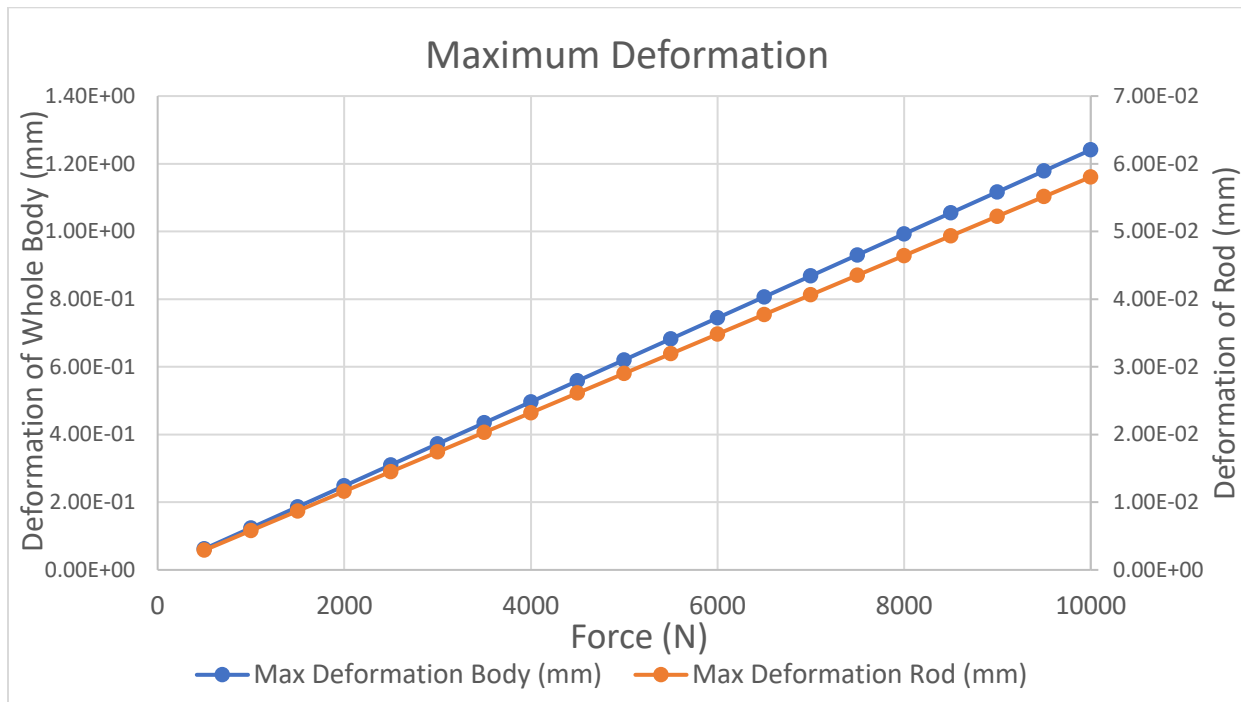


Figure 20: Maximum deformation experienced by the whole body and the rod for loading conditions of 0-10000N (structural steel)

Both deformations follow a linear trend as the force applied is increased. The rod deforms considerably less than the whole body with a maximum deformation of 0.058mm compared to the whole model which changes by 1.24mm for the highest loading condition. The location along with the distribution of these deformations are shown in the following contour plots.

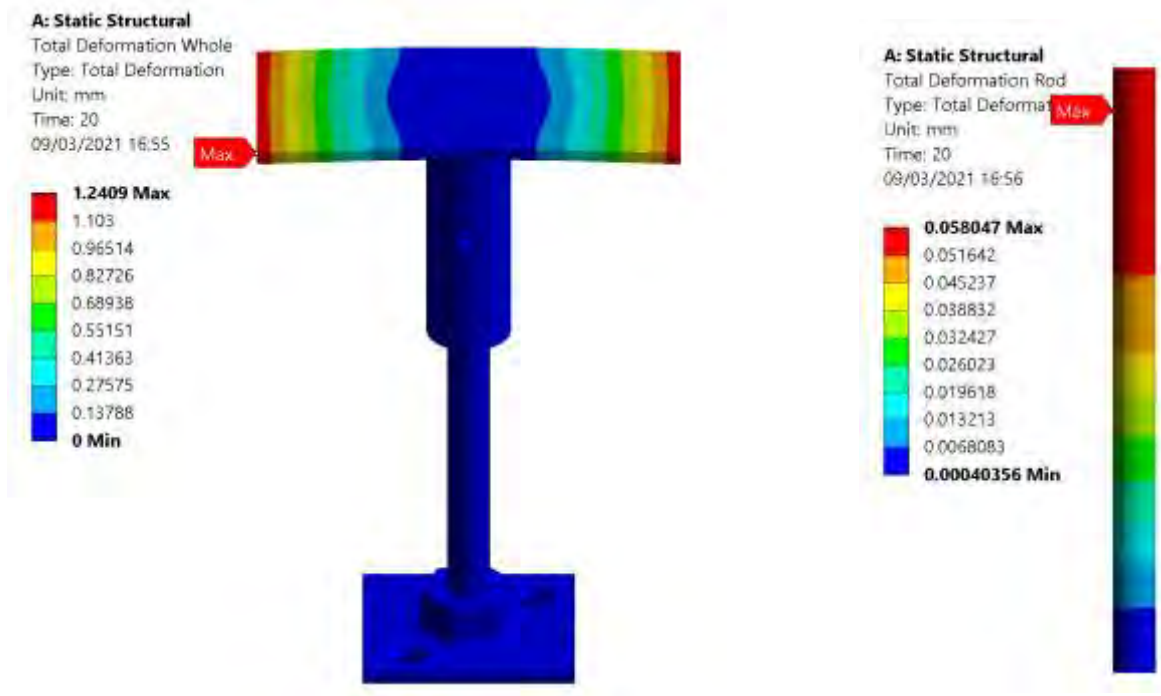


Figure 21: Deformation contour plots of whole body (left) and isolated rod (right)

The maximum deformation on the whole body occurs at the edges of the saddle and shows a gradual increase moving away from the centre. Examining the deformation of the rod, the maximum occurs near the top where the load is being applied and gradually decreased down its length.

4.3.5. Discussion

From carrying out stress analysis on the whole body it was identified that the areas experiencing the highest stress were located around the weld connecting the boss to the saddle. The reasoning for this stress concentration was likely due to the sharp change in geometry. Relative to this, the stress experienced by other components of the support was much lower. Considering the rod which was identified as a potential weak spot, it was found that its factor of safety was much greater than that of the whole body when the same loading conditions were applied.

The formation of the structure showed that the maximum occurred at the ends of the saddle and steadily increased travelling away from its centre. This was likely due to the way in which ANSYS applied the load, the force was uniformly distributed across the surface. However, in reality the force would not be distributed evenly with a greater proportion of it over the centre of the plate. Therefore, the deformation experienced by the saddle should not be as high during physical testing. The area of greater concern is the deformation experienced by the rod, this was much lower than the overall structure and provides a good comparison to the actual loading case.

4.4. Maximum Loading Conditions for an Array

After carrying out yield strength analysis on the support it was possible to determine the exact point at which the component will fail. From this, the maximum loading capabilities could be determined for both a singular leg and an array.

From the data displayed in Figure 15 the maximum allowable load was determined from the equation of the line as in equation 1 below. The linear trend was found to have an equation of:

$$y = 0.1009x - 0.0027 \quad \text{Equation 1}$$

Where y represents the stress experienced by the body and x represents the force applied. Knowing that the yield stress of the material was 250MPa, the equation was solved to find the load at which the support would fail.

$$250 = 0.1009x - 0.0027$$

$$x = 2477.7N$$

Therefore, the maximum load that a single leg can withstand before yielding is 2477.7N or 252.6kg. Using the data provided by UK Loft Boarding for the number of legs required for a given loft area (Boarding, 2020), the maximum loading was scaled from 6 to 192 legs.

The maximum loading value above does not incorporate a safety factor and therefore is the absolute maximum the material can withstand. Due to external factors that may weaken the support over time such as thermal expansion or corrosion, a safety factor of 2 was added to the model to ensure the supports remain safe over time. This factor of safety is adjustable at the discretion of the company to accommodate their needs, Figure 22 and Figure 23 show the maximum allowed load and equivalent mass, with and without a safety factor.

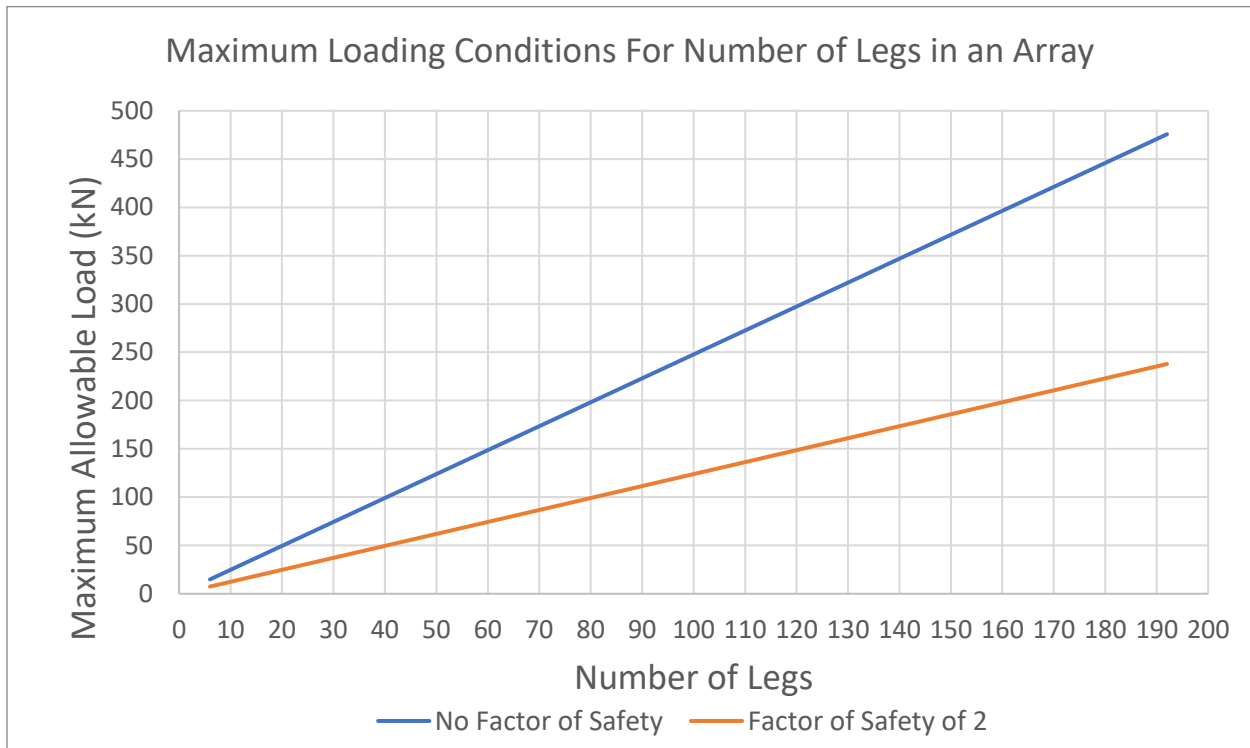


Figure 22: Maximum allowable load for an array of legs

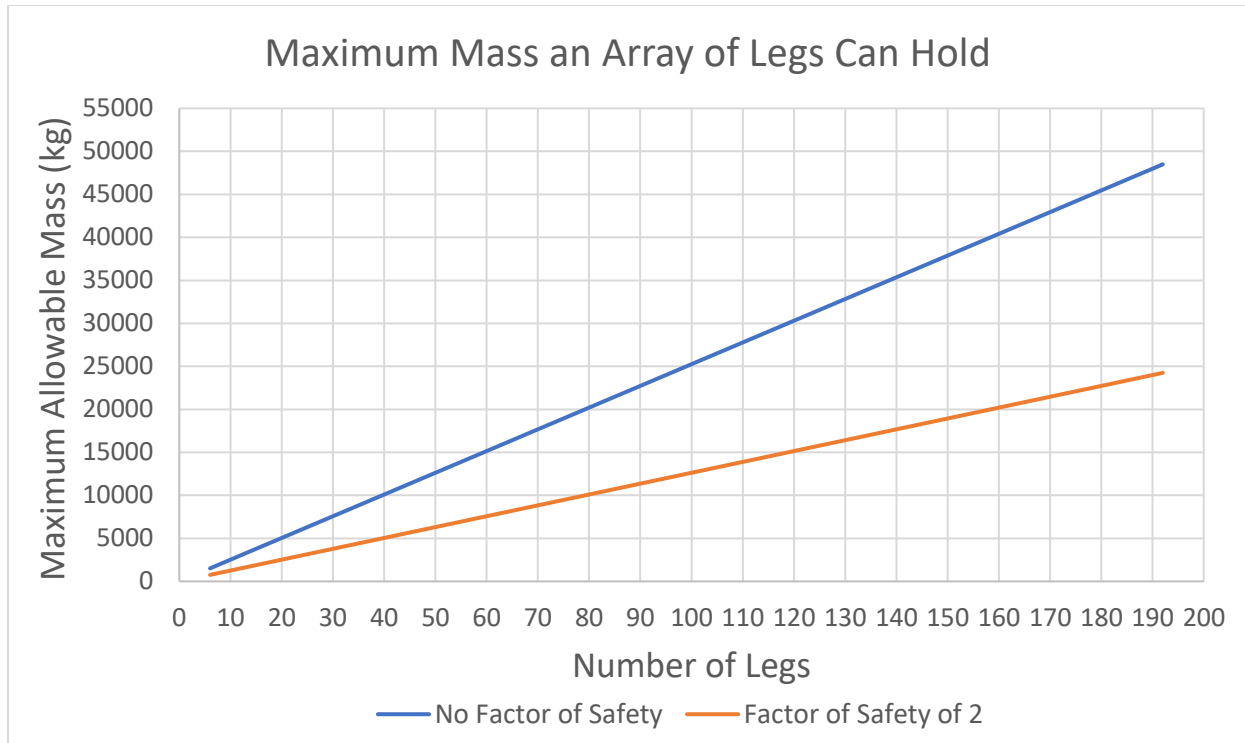


Figure 23: Maximum allowable mass for an array of legs

Even with a safety factor of 2, a single leg is still capable of carrying 126.3kg which is a significant load. Scaling this up to the smallest loft area of 4x4 feet requiring 6 'LOFT-E's it was found that the maximum mass the array can hold is 757.7kg. This value seems more than adequate for the needs of the company and shows the design of the product is fit for purpose.

4.5. Stability Analysis

In addition to assessing if the material will yield when subjected to an external load, the possibility of the threaded rod buckling was also investigated. The critical load at which buckling would occur is determined by equation 2 below:

$$P_{cr} = \frac{\pi^2 EI}{L^2} \quad \text{Equation 2}$$

Where:

E = Young's Modulus

I = 2nd Moment of Area

L = Length of the rod

P_{cr} = The load at which buckling occurs.

Youngs modulus was taken as 200MPa and the length of the rod was taken as 143mm.

$$I = \frac{\pi}{4} r^4 = 4.909 \times 10^{-10} m^4$$

$$P_{cr} = \frac{\pi^2 \times 200 \times 10^9 \times 4.909 \times 10^{-10}}{(143 \times 10^{-3})^2} = 47386.07N$$

The critical load required for buckling is much greater than the yielding load calculated previously. Proving that the rod will remain stable during working loading conditions and the factor of safety should be designed around the yielding load as this dominates the design.

4.6. Stress Due to Bending

4.6.1. Loading Scenario

In the scenario that the LOFT-E was supporting timber that had a non-uniformly distributed load, the stress experienced by the threaded rod would also have to take into consideration that caused by the bending moment. This would result in a stress that was greater than the uniaxial loading described previously. This section of the report explores an extreme example of stress due to bending to highlight the significant impact it could have on the design.

Uneven loading may happen if additional loads are applied to the timber at a distance away from the centre of the support. This would result in a bending moment that puts greater stress on the threaded rod as this has the narrowest cross section. Ultimately, this loading scenario would reduce the maximum load the support could carry.

Figure 24 depicts a possible loading scenario, the timber running along the saddle of the support has forces F_1 and F_3 applied in addition to its weight F_3 .

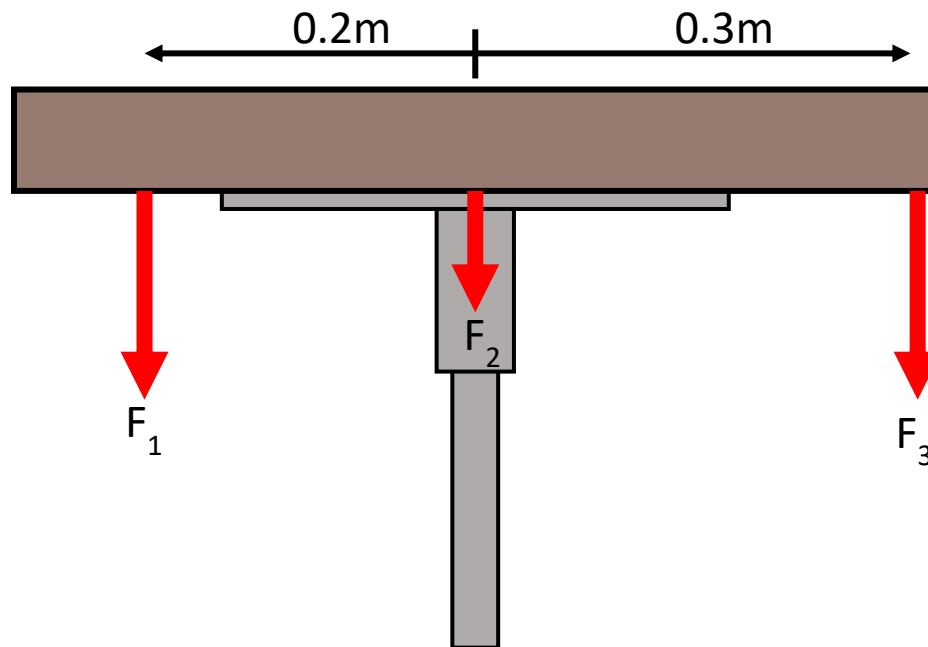


Figure 24: Bending loading scenario

The applied forces used in this simulation were the weight (F_2) passing through the LOFT-E leg, which was taken as 150N, and the load (F_1 and F_3) also applied on each side of the timber. The distance between the central axis of the support and F_1 and F_3 was kept constant at 0.2m and 0.3m respectively. Given the yield

stress analysis conducted previously, it was shown that the support was more than capable of carrying 150N prior to failure. Therefore, the effects of the additional loads could be highlighted in this simulation.

The loading case was replicated in ANSYS and the simulation was run for $F_1 = F_2$ ranging from 20N-400N and the maximum stress was recorded for each iteration. F_1 and F_2 were modelled as remote forces acting on the top face of the saddle (A and B in Figure 25). F_2 (C) represents the weight of the timber and acts as a surface effect, uniformly distributing the force over the face of the saddle.



Figure 25: Boundary conditions of bending loading

4.7. Results

4.7.1. Maximum Equivalent Stress

The simulation was run for 20 iterations with F_1 and F_2 increasing in magnitude from 20N – 400N. The maximum stress experienced by the whole support and the rod was recorded, from the results it could be seen that the maximum stress at every iteration was found in the rod. This agreed with our hypothesis due to its small cross sectional area and long length. Figure 26 shows the stress distribution of both the whole model and the rod in isolation.

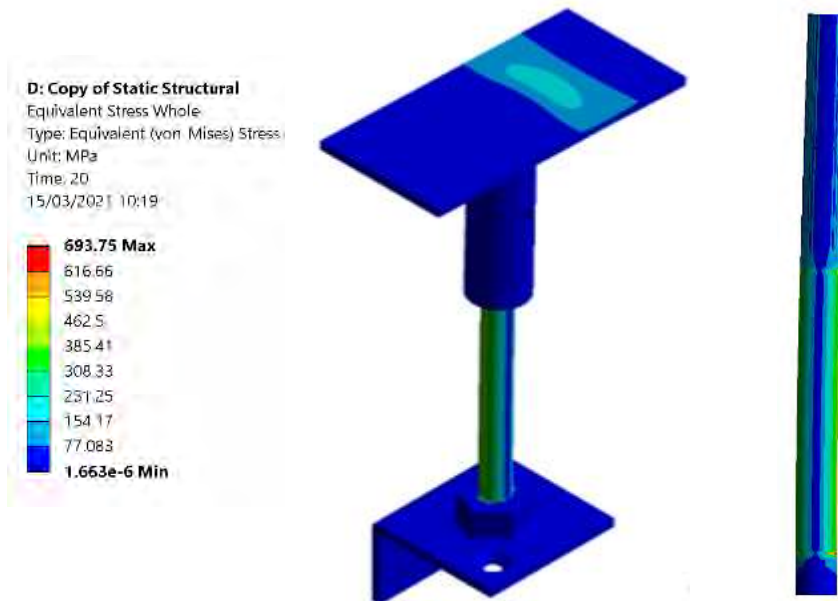


Figure 26: Stress distribution from bending loading on the whole body and isolated rod

The location of the maximum stress on the rod from Figure 27 was found to be at the point where it connects to the M10 nut on the foot of the support. This is because the rod is constrained here and the edge of the nut exerts a force on the rod as it pushes against its walls.

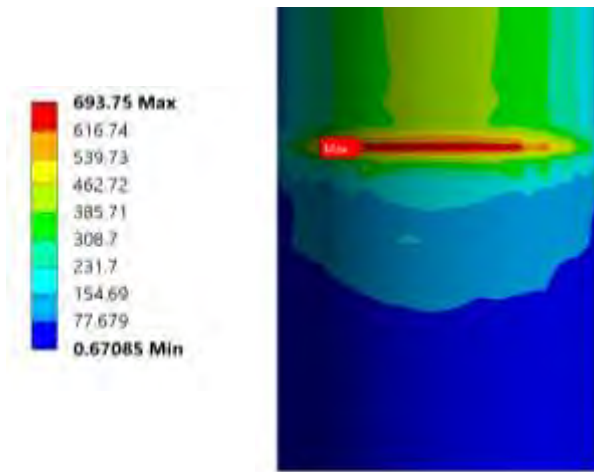


Figure 27: Location of maximum stress from bending loading

The maximum stress was plotted for each iteration along with the factor of safety. It can be seen that the failure load is significantly less than the uniaxial loading considered previously. In this scenario the factor of safety falls below 1 just after 430N is surpassed, this means that F_1 and F_2 were both at 140N. This is the equivalent of an additional 14kg being added at their points of application. As shown in the yield stress analysis, the structure is capable of withstanding in excess of 2500N when applied directly to the face of the saddle. Therefore, the effect of non uniform loading has a significant effect on the structural stability of the rod.

4.7.2. Discussion

The application of external loads away from the saddle showed a drastic decline in the failure stress of the support. The main area of concern for this loading scenario was the rod, specifically where the maximum stress occurred, its connection to the M10 nut on the foot. This test showed the importance of ensuring that the load applied to each LOFT-E is uniformly distributed across its surface. Furthermore, the application of additional loads to timber beams connecting supports should be minimised to prevent damage to the threaded rod. To reduce the stress experienced due to this loading scenario, the cross section of the threaded rod could be increased.

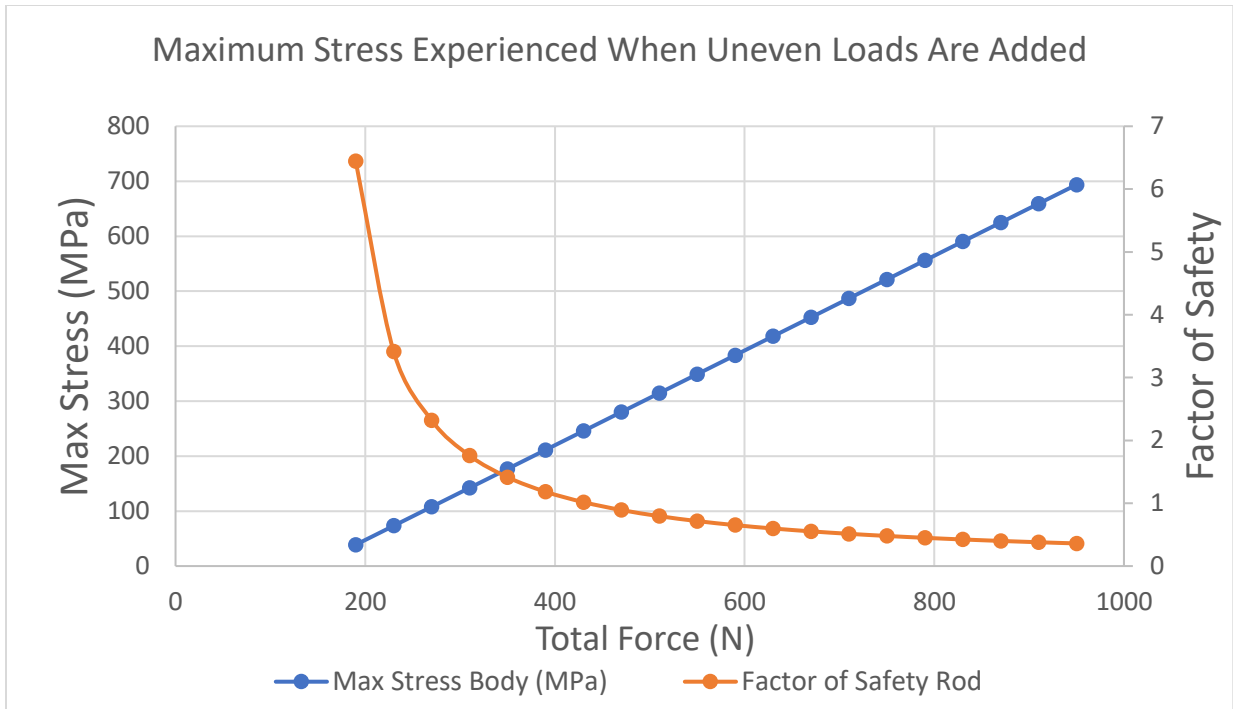


Figure 28: Maximum stress experienced when additional loading is applied away from the geometry

4.8. Recommendations/Design Optimisation

4.8.1. Different Material Simulations

The same simulations were carried out for the loft but for different materials which make up the loft support. These materials included: bronze, carbon steel, low alloy steel, stainless steel, and titanium alloy. The data provided for these materials to carry out the simulations were already set up in ANSYS under engineering data cell → engineering data sources → ANSYS GRANTA Materials Data for Simulation (Sample). These results can then be compared with the structural steel results and a conclusion could be drawn out.

For all materials, the relationships are following the same trend in that the stress increases linearly as force increases. Alongside the stress, the factor of safety rapidly decreases as force increases before its rate of decrease lowers as the loading increases. The maximum stress values for all materials simulated are almost identical to one another including the maximum stress on the rod. All materials gave the same linear relationship for deformation as loading increased however, some materials deformed more than others.

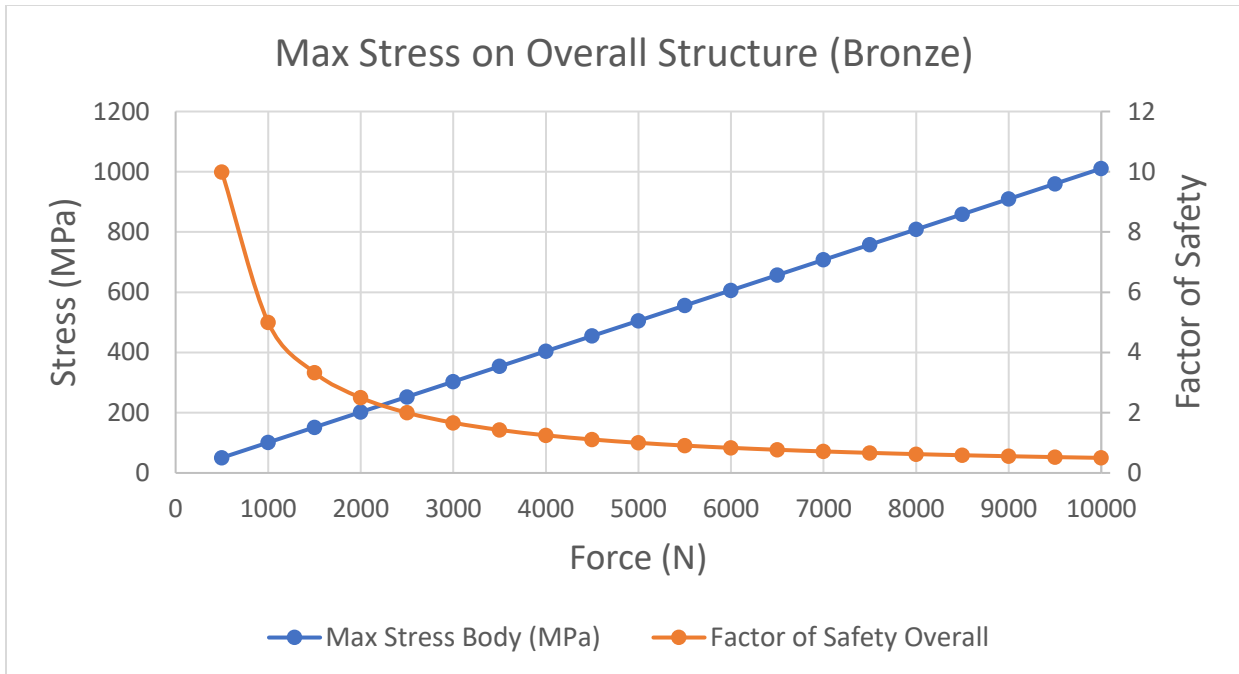


Figure 29: Maximum stress experienced by the whole structure when loaded from 0-10000N (bronze)

When setting up the loft to be made out of bronze, the stress and factor of safety relationship with force is as shown in Figure 29 the factor of safety starts at around 10 when analysing the whole body of the loft. The point when the factor of safety drops below 1 is around 5000N which in comparison with structural steel in Figure 15, is a higher level of loading that bronze can take indicating that bronze can withstand a larger amount of force without the material yielding.

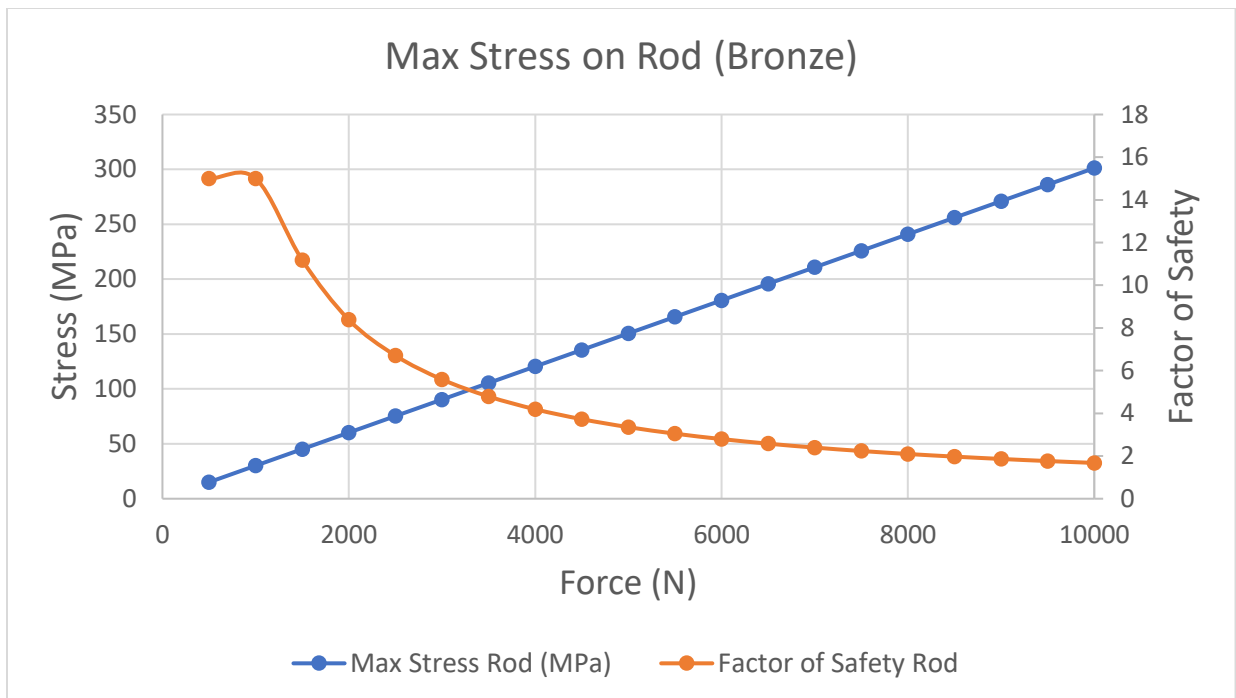


Figure 30: Maximum stress experienced by the rod when loaded from 0-10000N (bronze)

Focusing on the rod as shown in Figure 30, the factor of safety for bronze remains constant at 15 before decreasing as the loading increases beyond around 1000N. This already indicates that bronze is a much stronger material in withstanding these forces than structural steel. Even at 10000N, the factor of safety for the rod is still above 1 whereas for structural steel, the factor of safety drops below 1 just before 10000N is applied. Having the rod made from bronze would be structurally beneficial due to its high factor of safety at high levels of loading.

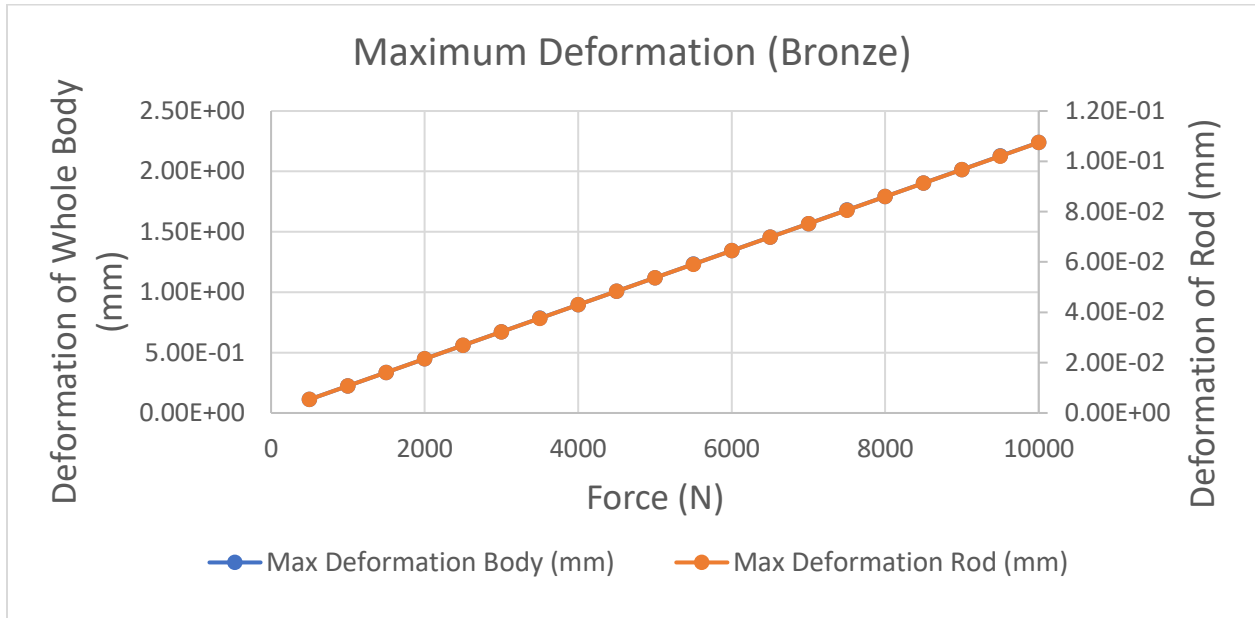


Figure 31: Maximum deformation experienced by the whole body and the rod for loading conditions of 0-10000N (bronze)

Comparing Figure 31 and Figure 20, it can be said that structural steel produces a smaller deformation than bronze

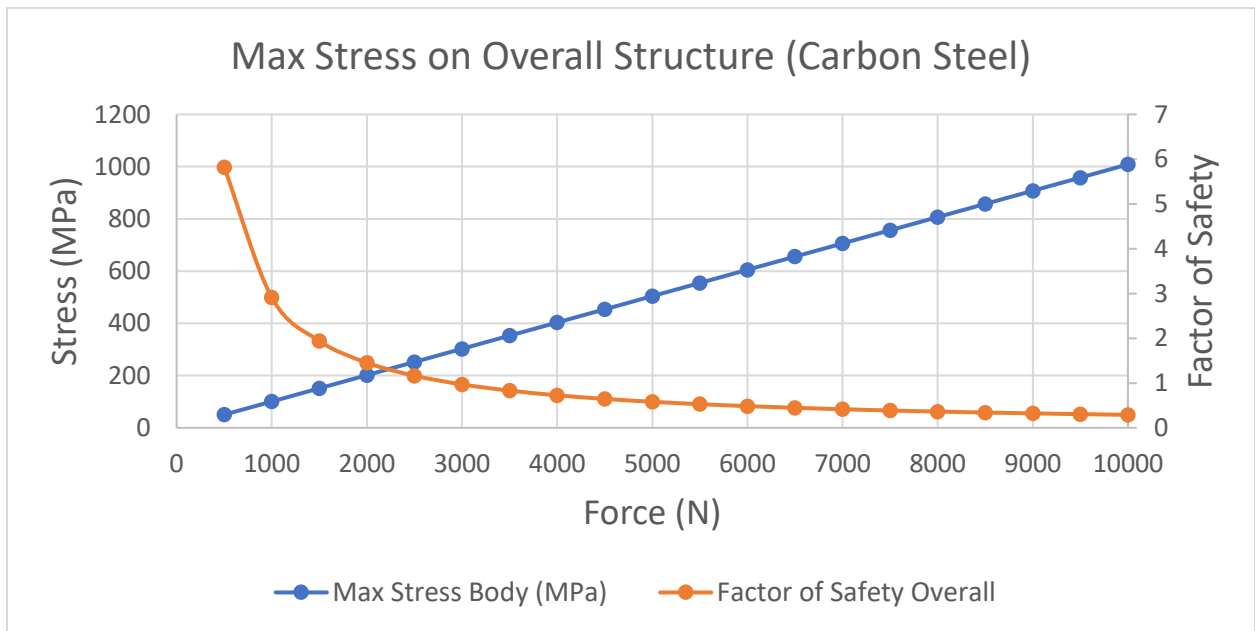


Figure 32: Maximum stress experienced by the whole structure when loaded from 0-10000N (carbon steel)

Allocating the whole body to be made from carbon steel, the stress and factor of safety relationship with force is shown in Figure 32. The starting factor of safety when a load is applied is around 4 factors smaller than bronze but around 1 factor higher than structural steel. The point where the factor of safety drops below 1 is around 3000 N stating that it is more durable than structural steel but not as durable as bronze. The maximum factor of safety starts at around 6 with it rapidly decreasing initially as loading increases before slowing its rate of decrease. This suggests that carbon steel isn't as effective in supporting a large load as bronze is.

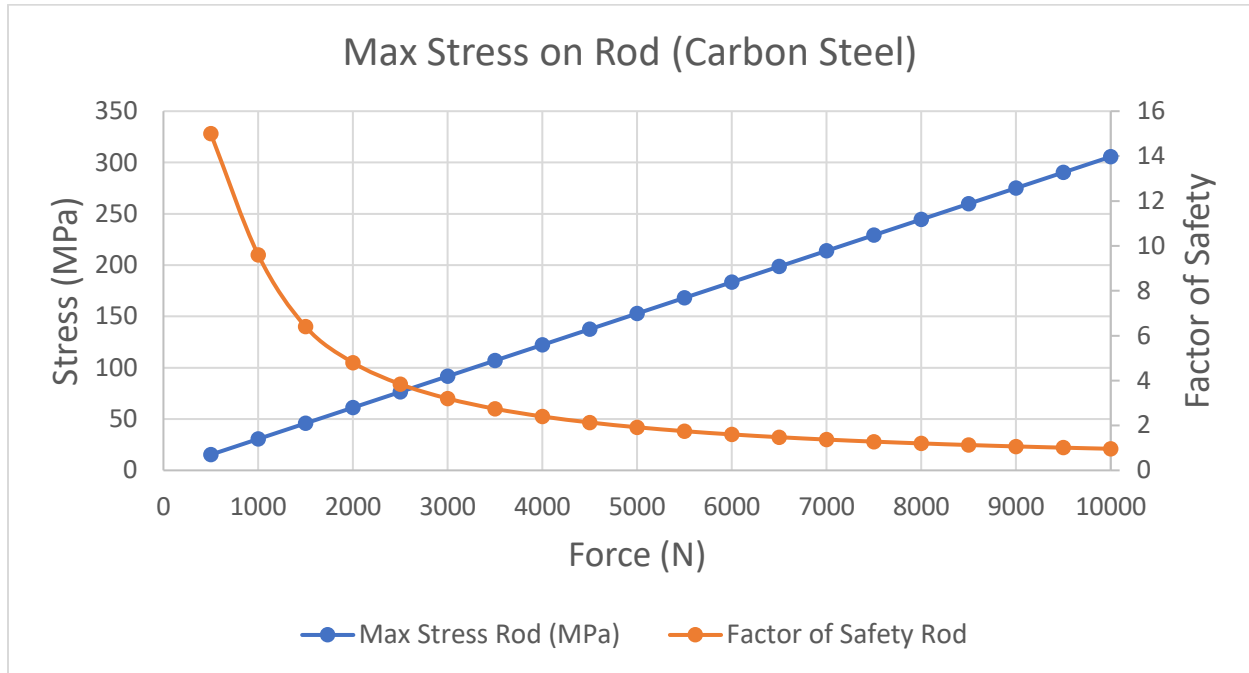


Figure 33: Maximum stress experienced by the rod when loaded from 0-10000N (carbon steel)

Shifting focus onto the rod in Figure 33, the initial factor of safety starts at around 13 and drops below 1 at around 9000 N. The final factor of safety at 10000 N is slightly higher than structural steel suggesting this material is suitable as a rod to hold the loft together however it is not as suitable to hold higher levels of loading than what bronze is capable of.

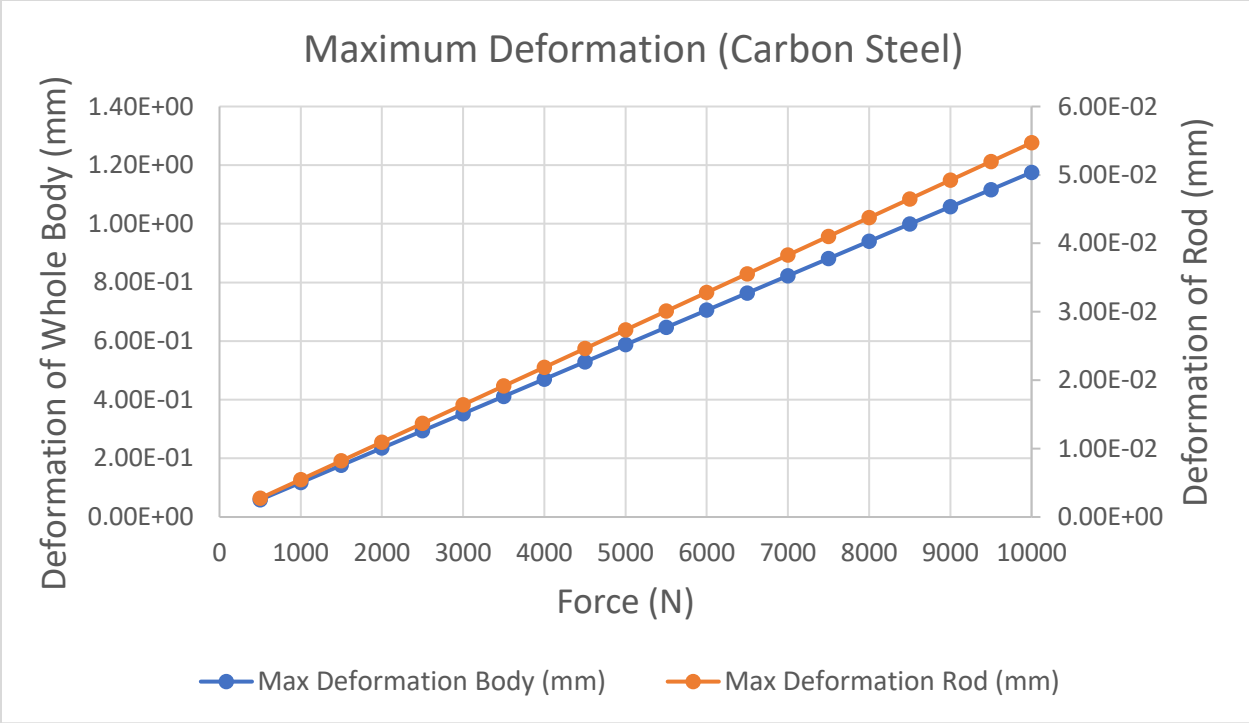


Figure 34: Maximum deformation experienced by the whole body and the rod for loading conditions of 0-10000N (carbon steel)

The relationship of force and deformation is again linear like with bronze and structural steel however, the magnitude of deformation shown in Figure 34 is slightly similar to structural steel albeit slightly lower but much lower than bronze. Again, the rod shows a significantly lower amount of deformation than the whole body.

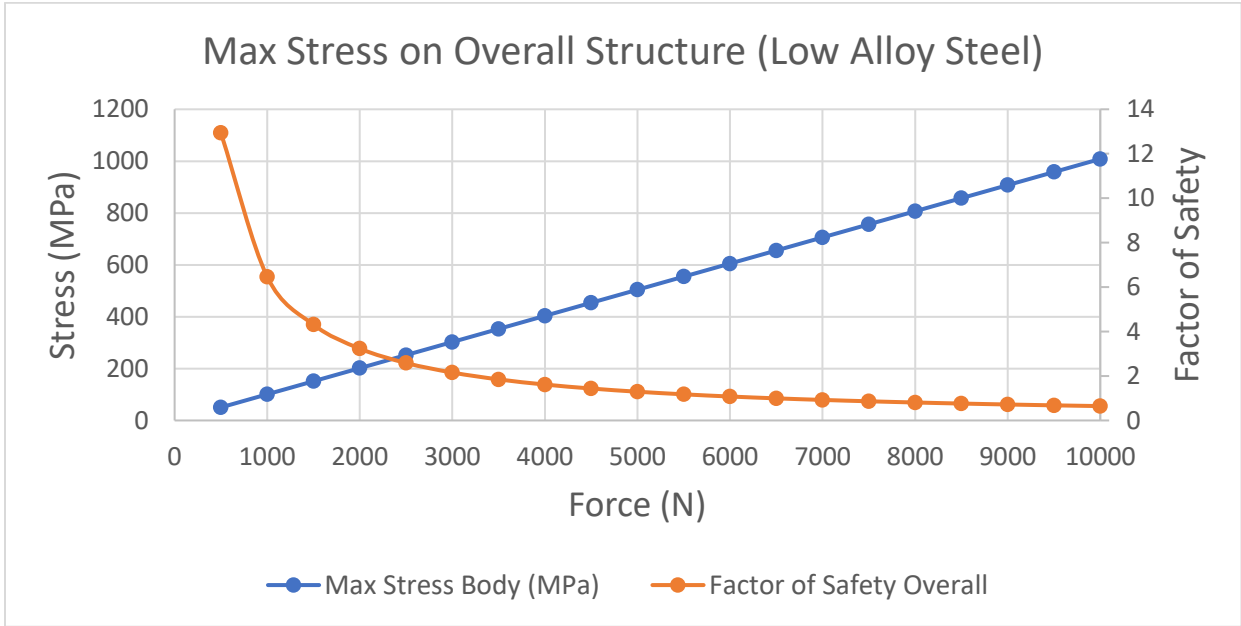


Figure 35: Maximum stress experienced by the whole structure when loaded from 0-10000N (low alloy steel)

Changing the loft support to be made out of low alloy steel, the stress and factor of safety relationship is shown as in Figure 35 where the initial factor of safety is around 13 which is around 8 factors of safety higher than Figure 15. The point where factor of safety drops below 1 is around 6000 N which in comparison to 2500 N from structural steel in Figure 15 is a much higher yielding force. It is also higher than what bronze can support before yielding thus suggesting that the low alloy steel is more capable of holding the loft support better.

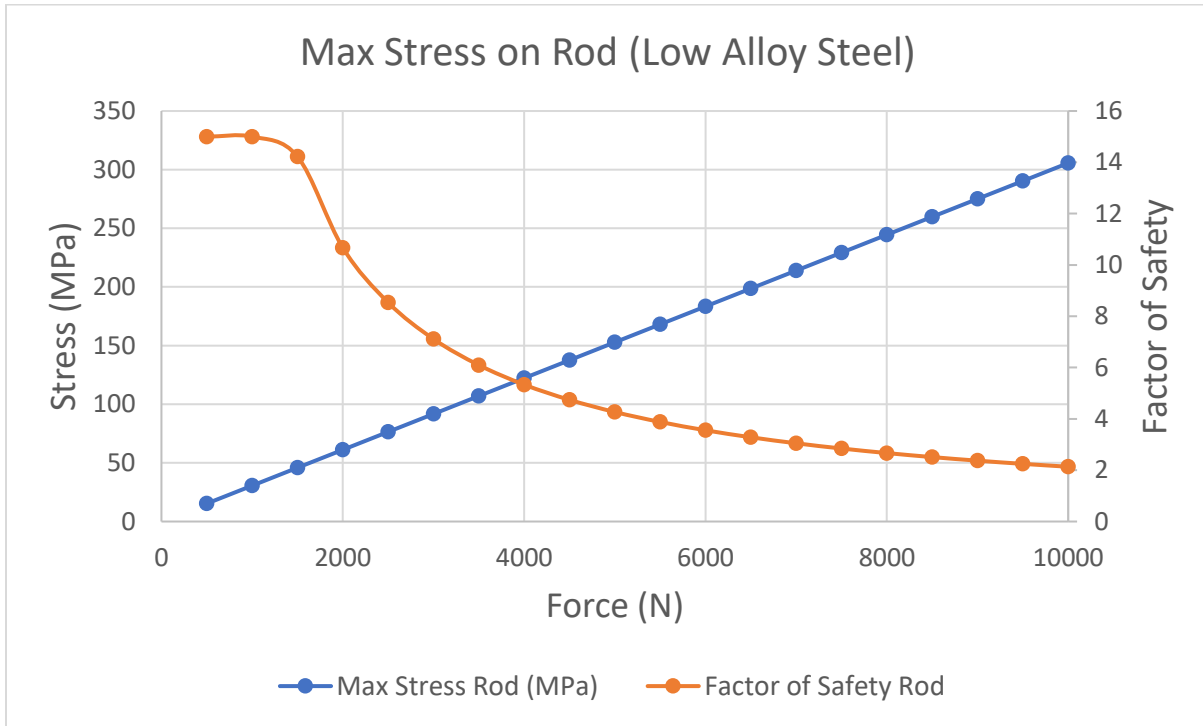


Figure 36: Maximum stress experienced by the rod when loaded from 0-10000N (low alloy steel)

Focusing on the rod of the loft support, the stress and safety factor relationship is as shown in Figure 36 where there is a constant factor of safety of 15 before 2000 N is reached and by observing the final force value of 10000 N, it shows a factor of safety of just under 3 suggesting that low alloy steel can take a much larger force beyond 10000 N and also surpass bronze maximum loading.

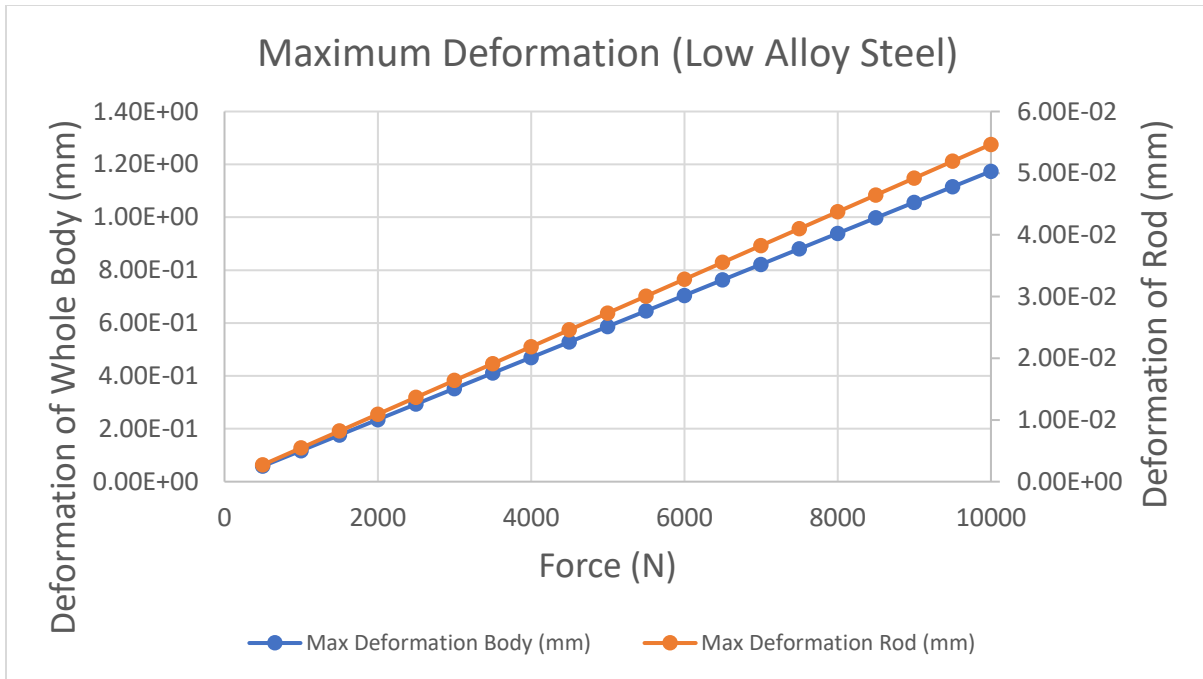


Figure 37: Maximum deformation experienced by the whole body and the rod for loading conditions of 0-10000N (low alloy steel)

The maximum value of deformation shown in Figure 37 is shown to be similar to carbon steel for both the whole body and the rod but much lower than bronze in Figure 31 and also lower than structural steel from Figure 20.

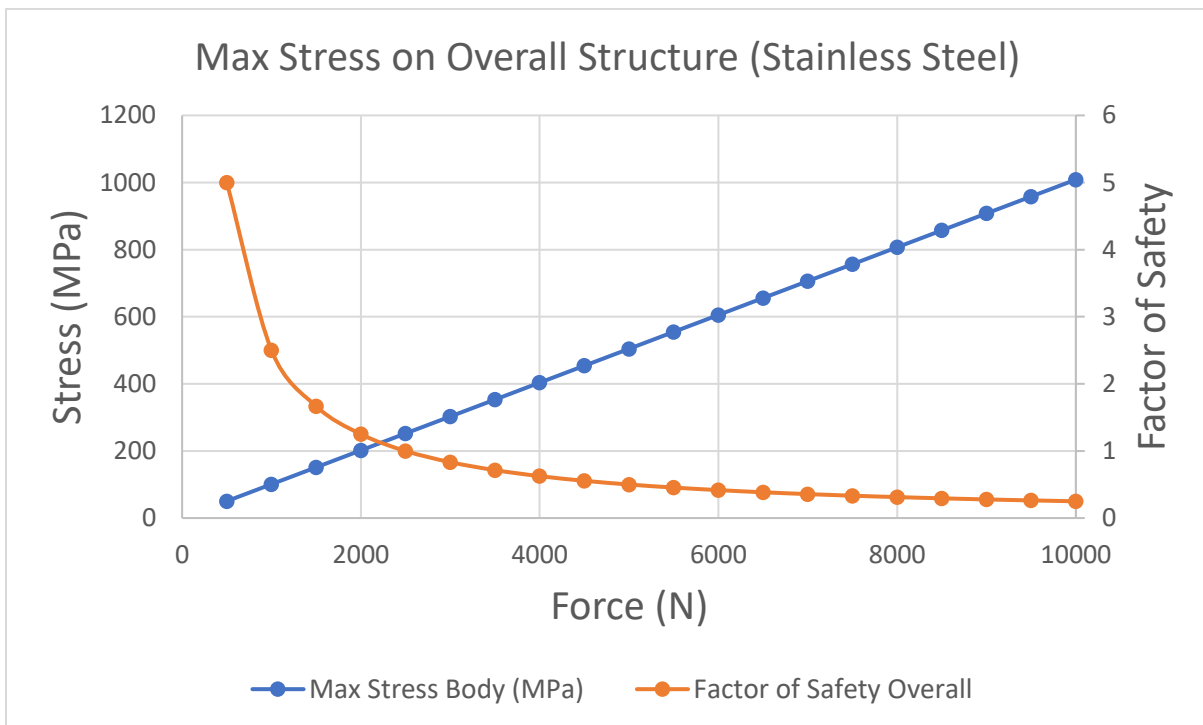


Figure 38: Maximum stress experienced by the whole structure when loaded from 0-10000N (stainless steel)

From Figure 38 with the loft support made from stainless steel, the initial factor of safety is around 5 which is roughly the same as the whole body made from structural steel from Figure 15. In fact, the overall result of stainless steel is somewhat the same as structural steel meaning that it isn't as structurally strong as the likes of bronze, carbon steel and low alloy steel.

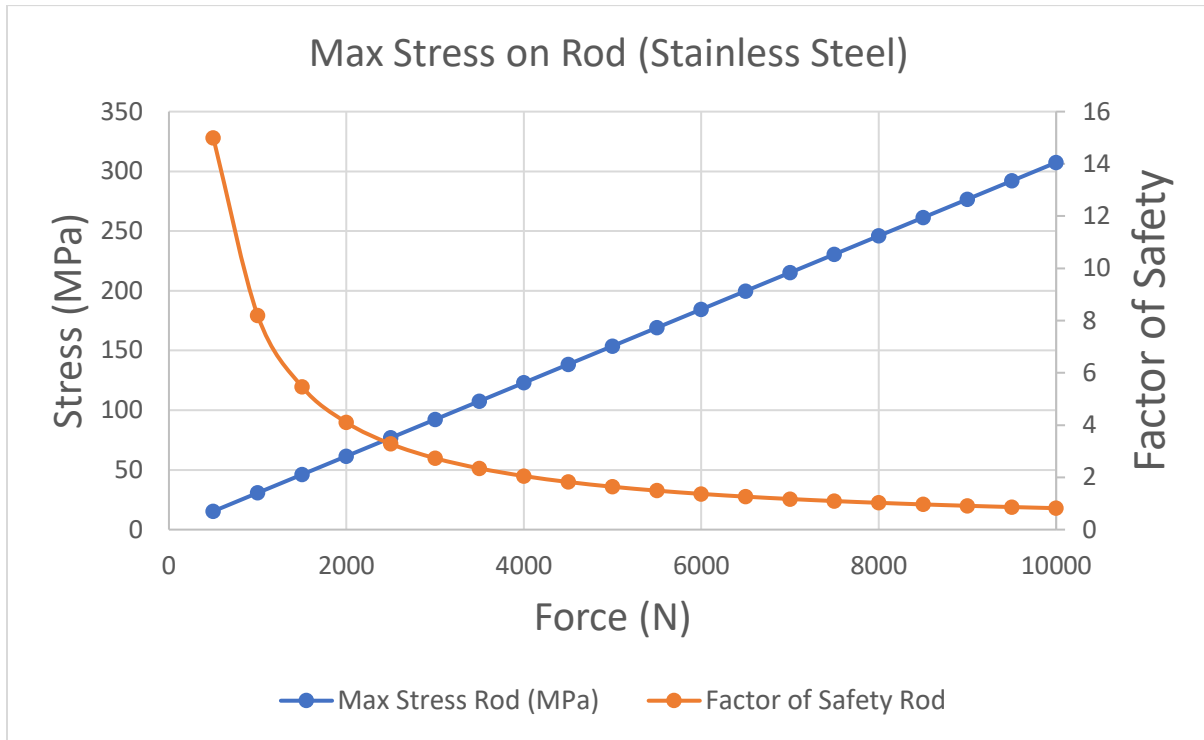


Figure 39: Maximum stress experienced by the rod when loaded from 0-10000N (stainless steel)

Since the results for stainless steel are almost identical to structural steel, it is expected that the focus on the rod would yield the near identical results to structural steel as in Figure 19 and although the factor of safety follows this trend, the stress at 10000 N appears to be 100 MPa lower than structural steel.

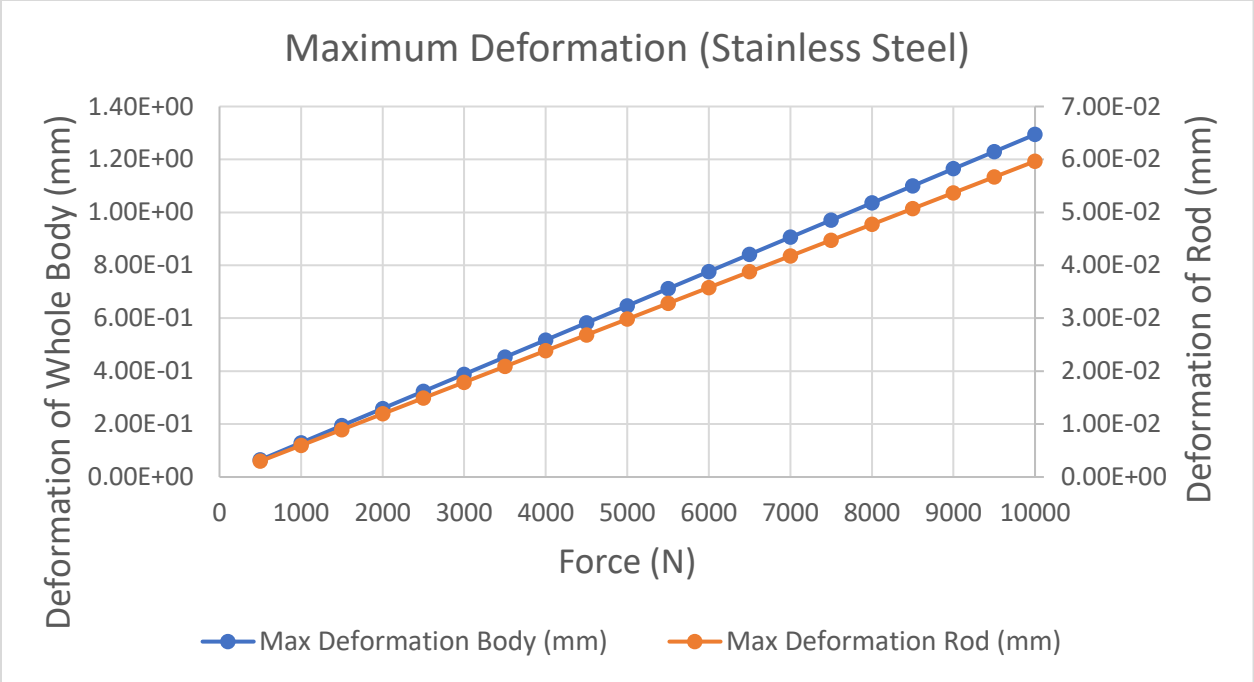


Figure 40: Maximum deformation experienced by the whole body and the rod for loading conditions of 0-10000N (stainless steel)

The deformation values in Figure 40 are similar to the deformation of structural steel given in Figure 20 albeit stainless steel yields slightly higher deformation values than structural steel. The deformation values are also smaller than bronze.

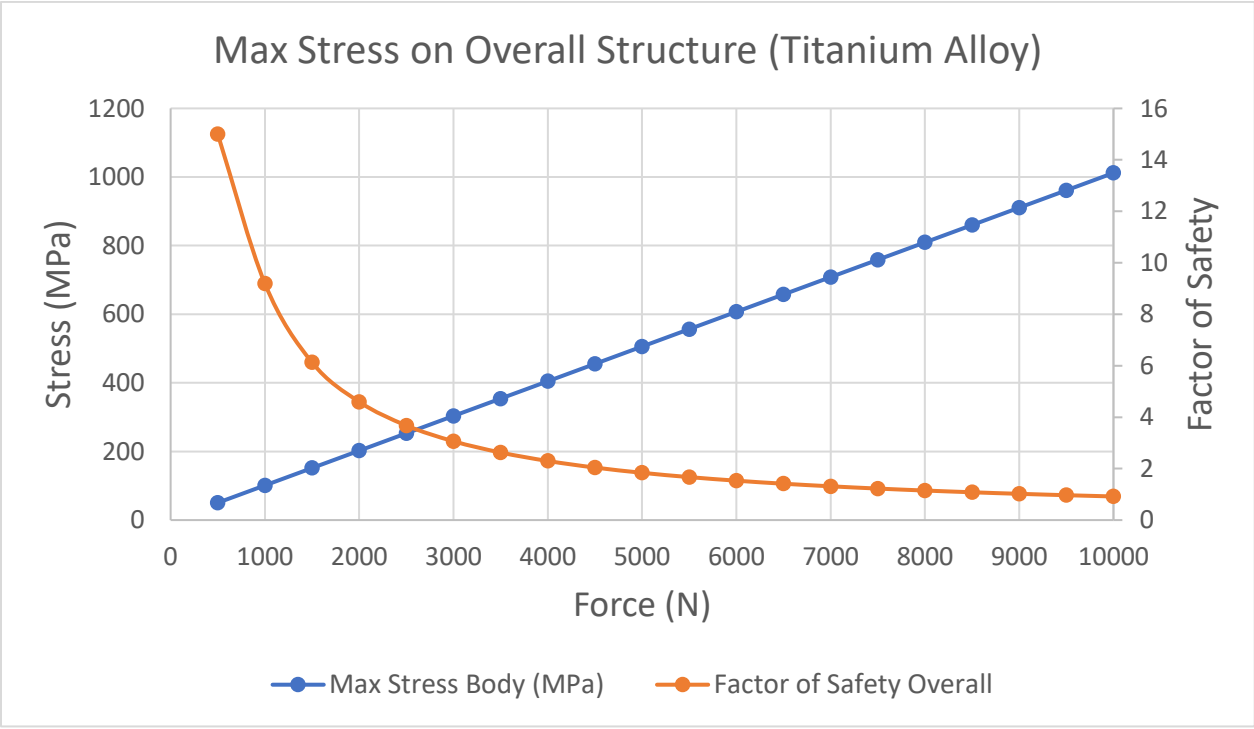


Figure 41: Maximum stress experienced by the whole structure when loaded from 0-10000N (titanium alloy)

Allocating the material to be titanium alloy for the loft support, the factor of safety of the overall structure as shown in Figure 41 starts at 15 and its maximum loading it can take is around 9000 N before yielding which is significantly higher than what structural steel, bronze, carbon steel, low alloy steel and stainless steel can achieve.

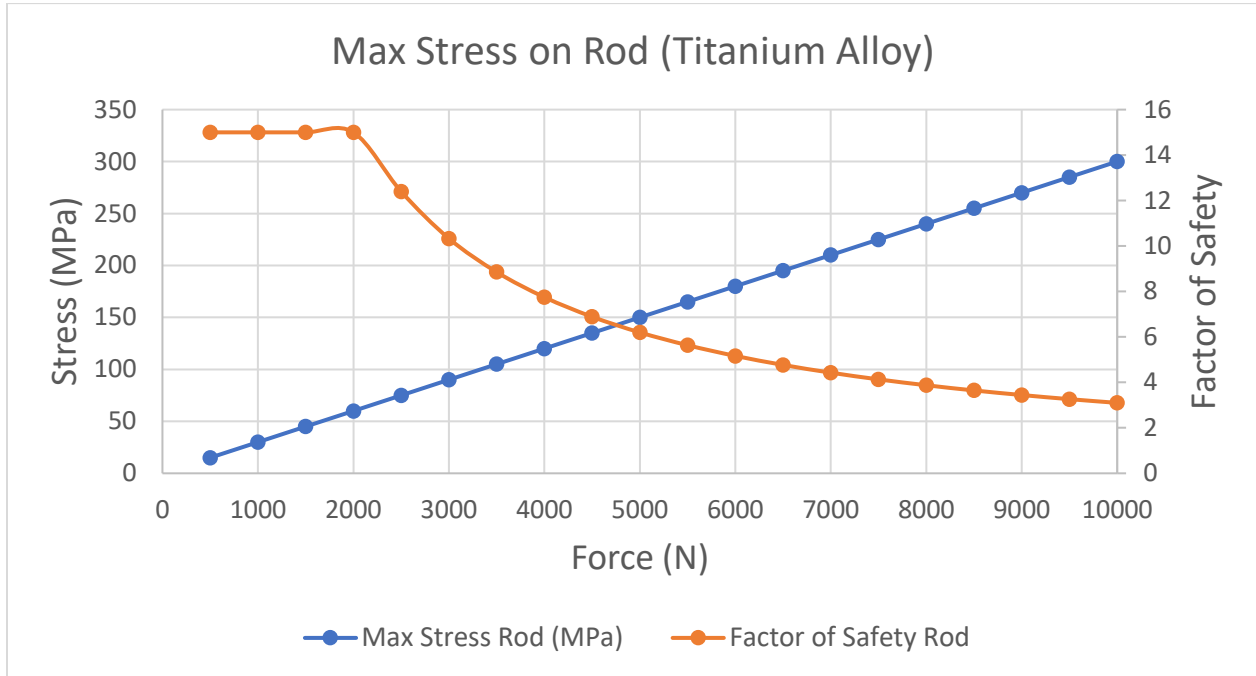


Figure 42: Maximum stress experienced by the rod when loaded from 0-10000N (titanium alloy)

The factor of safety of titanium alloy on specifically the rod as shown in Figure 42 is initially constant at 15 until a loading of around 2500 N is applied where it begins to drop and at the highest point of loading of 10000 N, its factor of safety is still above 1 and in comparison to bronze and low alloy steel, its value is higher than those two materials and significantly higher than what structural steel can take from Figure 19. This suggests that the yielding force will be beyond those for bronze and low alloy steel.

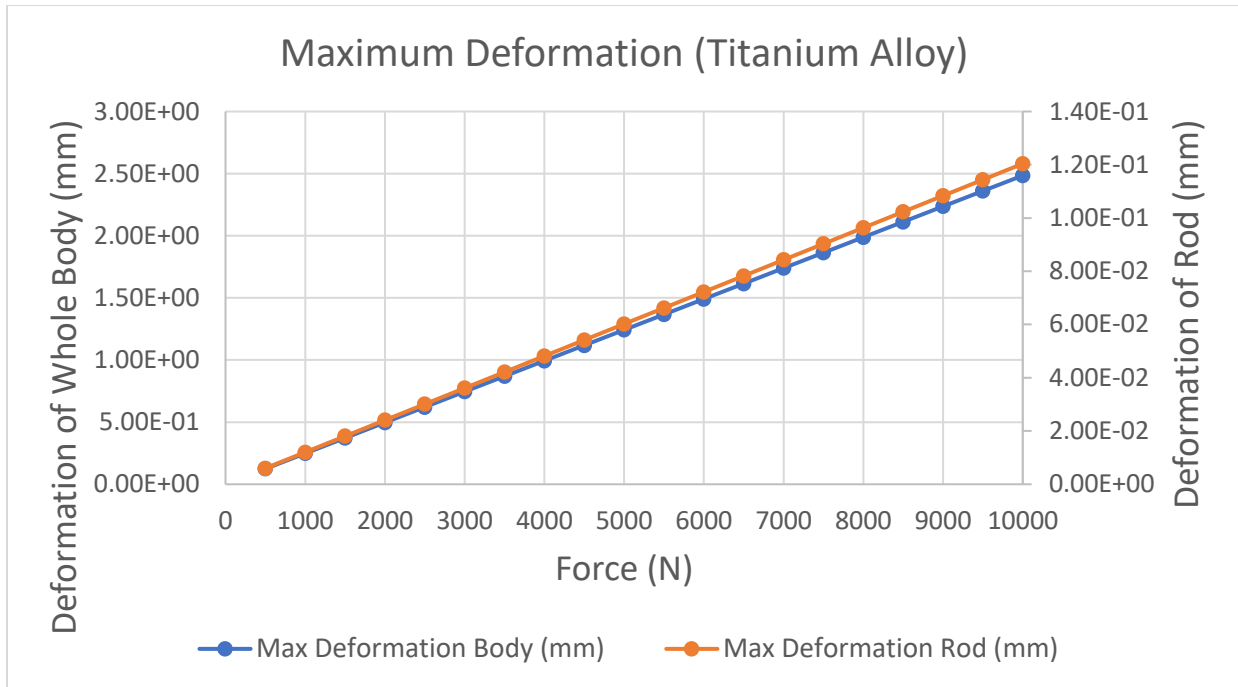


Figure 43: Maximum deformation experienced by the whole body and the rod for loading conditions of 0-10000N (titanium alloy)

The deformation of titanium alloy as shown in Figure 43 is higher than low alloy steel for both the whole body and the rod. With the maximum deformation at 10000 N showing around 2.5 mm for the whole body and 0.12 mm for the rod whereas for structural steel in Figure 20, the deformation is much lower with maximum values of around 1.24 mm for the whole body and 0.058 mm for the rod.

4.8.2. Material Selection for Bending Optimisation

Having highlighted stainless steel and low alloy steel as potential candidates for design optimisation. They were subject to the same loading scenario described in section 4.6.1 of this report, to assess their ability to withstand unevenly distributed loads. Two simulations were run for each of the materials, in the first, the load applied directly to the saddle was kept at a constant 150N and the forces applied at 0.2m and 0.3m from the centre were increased from 20-400N. The second simulation removed the external loads and mirrored the total force of the previous simulation purely through the load acting on the plate of the saddle. In doing so, a direct comparison could be made to assess the effect of bending against a uniformly distributed load.

The maximum stress and safety factor were recorded for each of the simulations and plotted in the figures below.

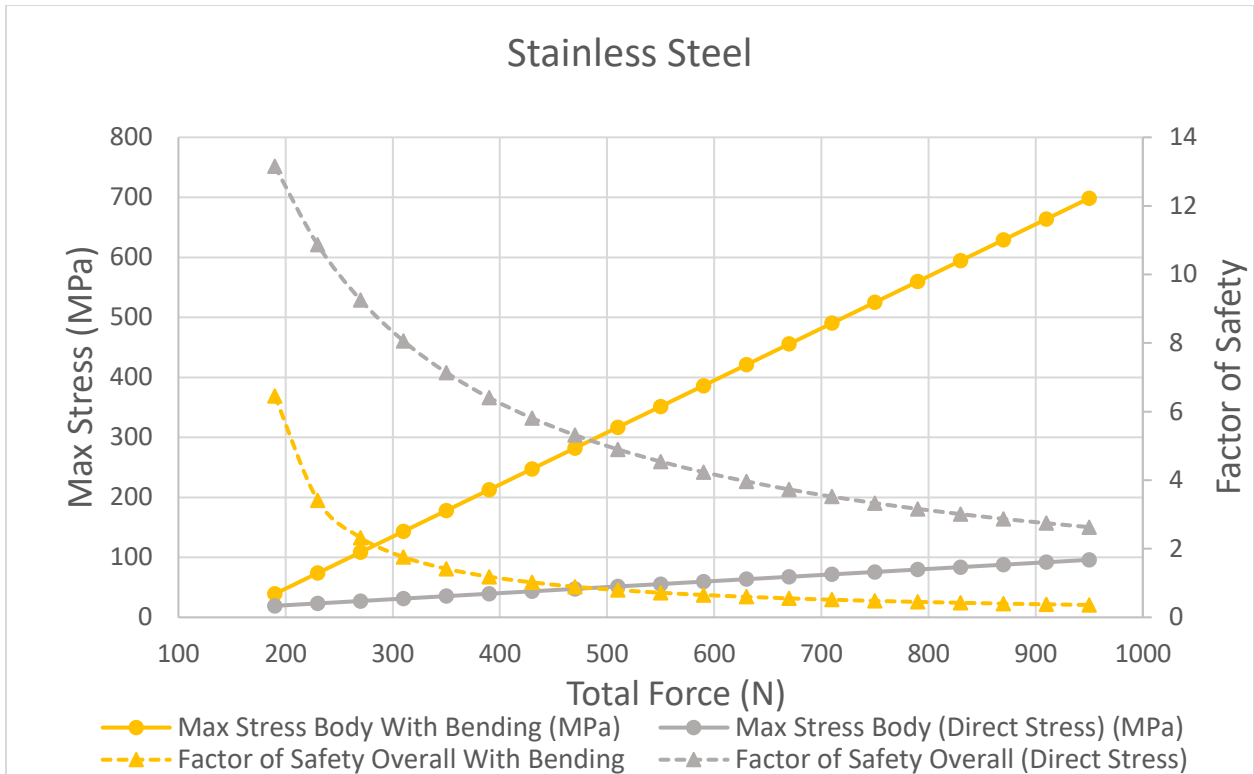


Figure 44: Comparison of uniform and non-uniform loading for stainless steel

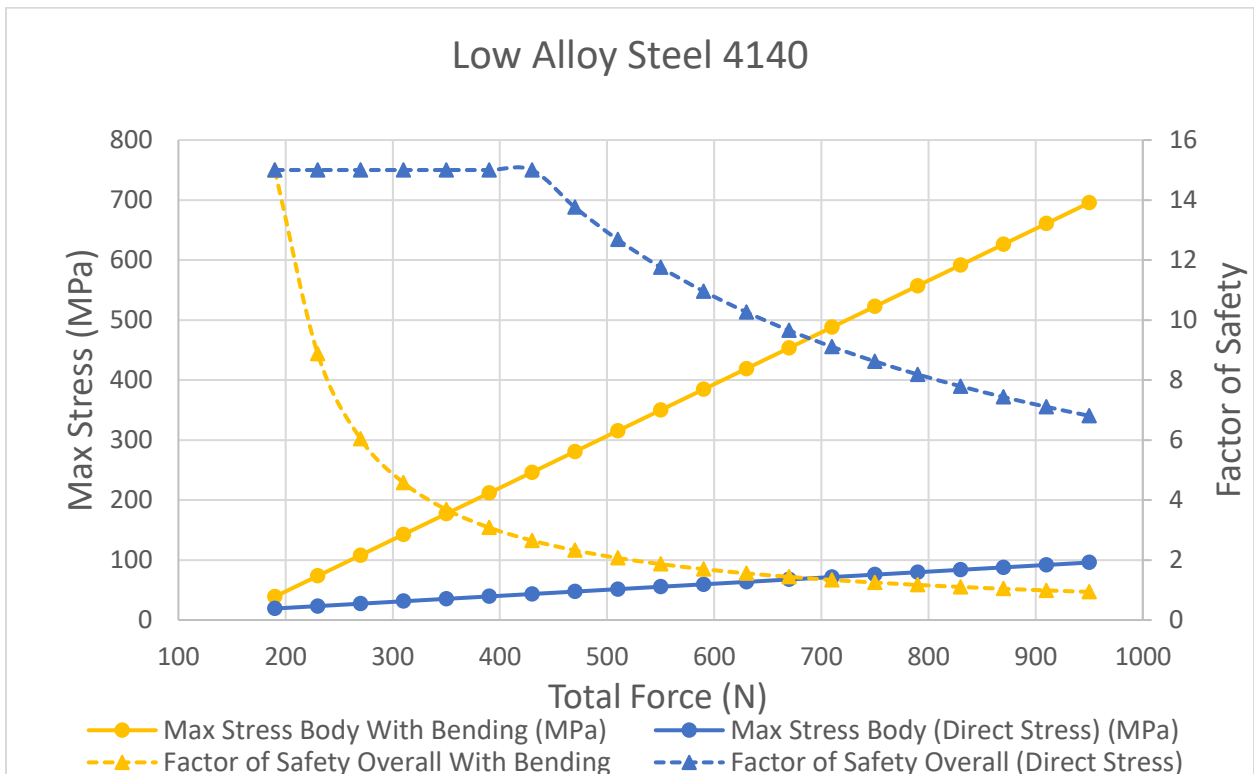


Figure 45: Comparison of uniform and non-uniform loading for low alloy steel

It is clear from the data shown that low alloy steel performs significantly better than both stainless steel and structural steel under these loading conditions. To further highlight this change, the safety factor when subjected to bending was plotted for the 3 materials.

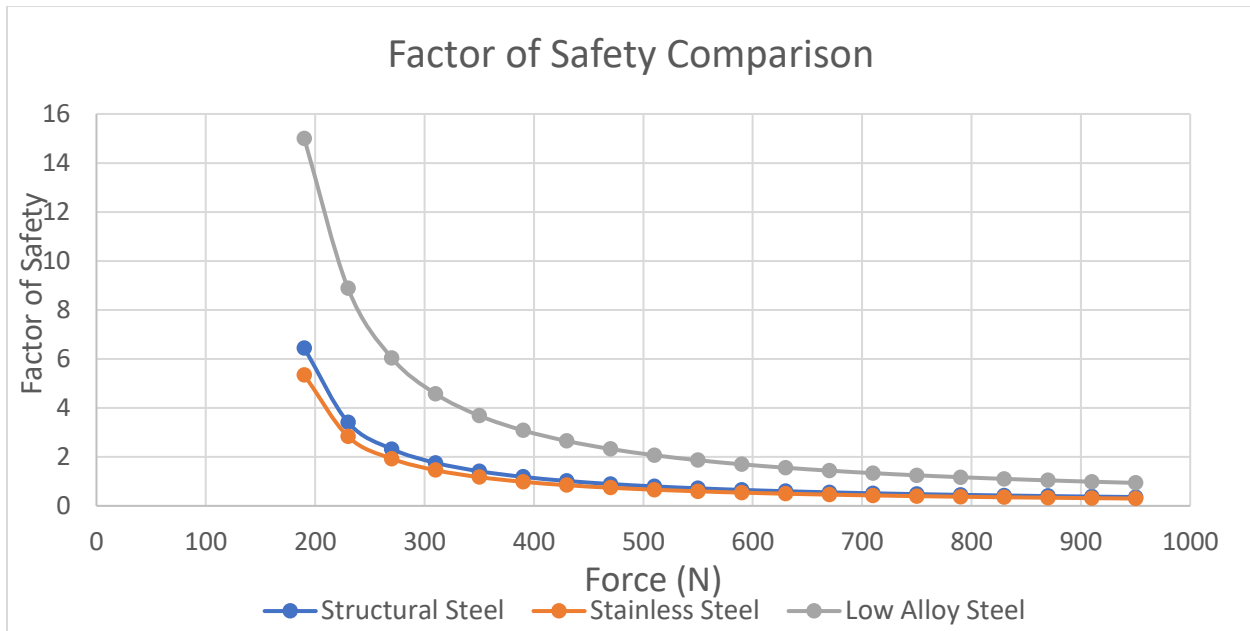


Figure 46: Factor of safety comparison for different materials subjected to non-uniform loading

Low alloy steel was able to withstand the greatest load prior to failure, with the factor of safety only dipping below 1 after 870N was surpassed. Comparatively the factor of safety of structural steel and stainless steel both fell below 1 after 430N. This shows that low alloy steel has the ability to support over double that of structural and stainless steel and should be considered if the support could be subject to uneven loading that would cause stress in the rod.

5. Thermal Aspects

5.1. Mesh

5.1.1. The Simulation Concept

The product being simulated will contribute to the overall thermal performance of the loft's insulation relative to the rooms below. Upon review of the documentation provided by Cumbria Loft Boarding, as well as initial discussions with the company, the implementation of the product and its operating environment were identified. The product would never be used in singularity, rather in an array of components to hold the load of the entire loft floor. The product would also be surrounded by insulative material, to ensure the heat transfer from the rooms below to the loft is kept to a minimum. Although the array of components will contribute to the overall thermal performance of the loft insulation, it was a logical decision to simulate a certain block of the loft insulation and support system. This block would contain the layers involved in the thermal transfer, these being the loft floor, insulative material, the room ceiling as well as one of the loft legs and supporting sections of the foundational timber truss members. As a result of this simplification the thermal transfer could be modelled in greater detail with the use of finer meshing strategies within ANSYS.

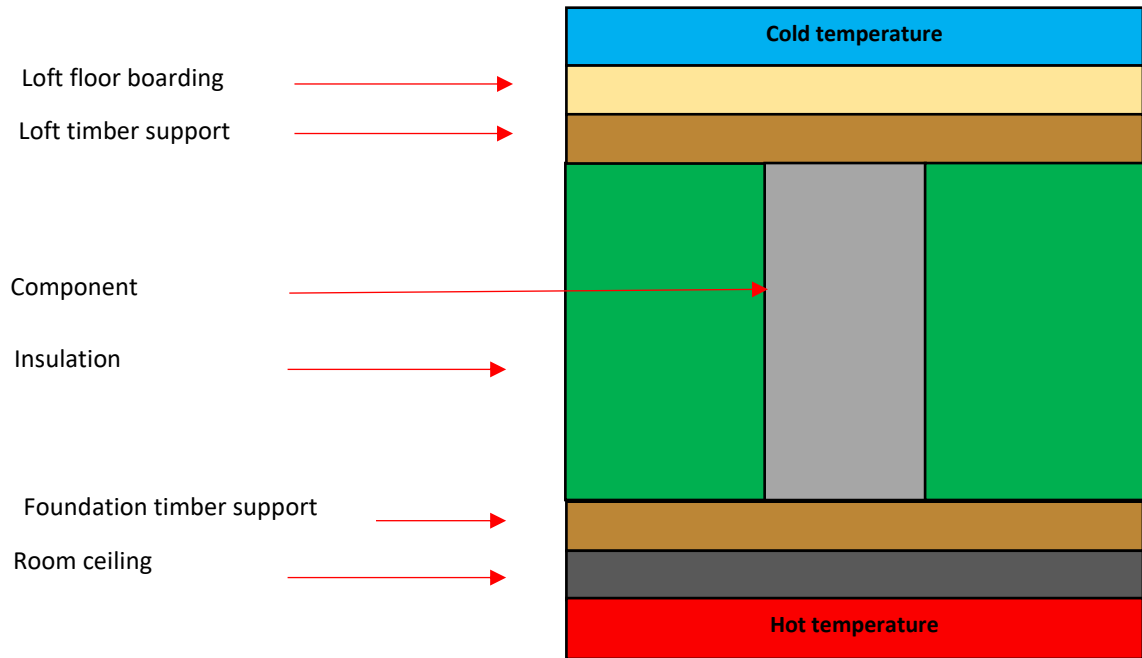


Figure 47: Block diagram for intended model simulation

5.1.2. Mesh Generation and Refinement

Upon importing the thermal CAD model set up it was determined to utilise the default mesh settings as a benchmark, such that the mesh refinement process could begin. The imported CAD model is depicted in Figure 48.

The factors which were assessed continually throughout this process were the element quality, aspect ratio and skewness among others. The values of these factors determined the overall quality of the meshing strategy, thus detailing how reliable the simulation results would be in representing the thermal effects of the scenario. However, the number of elements and nodes were also closely monitored to ensure the simulation was able to deliver useful results but in the most efficient manner possible, without using unnecessary computation. The initial default mesh values are shown in Table 4.

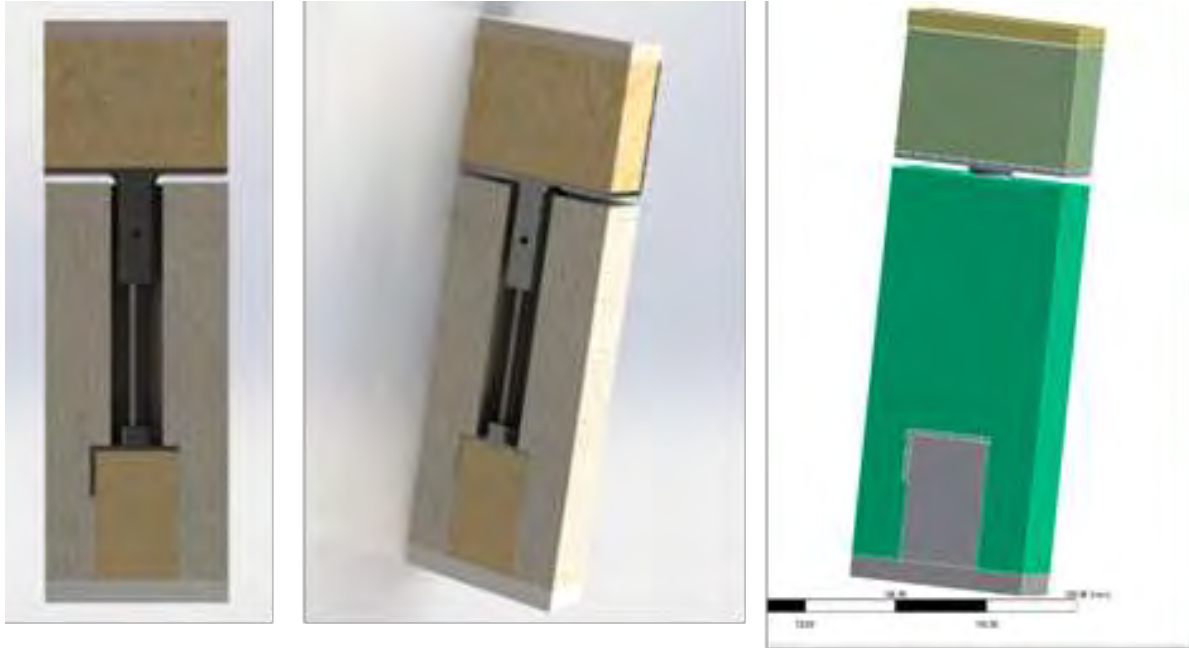


Figure 48: CAD model and default mesh application

Table 4: Initial mesh statistics

Element type	No. of elements	No. of nodes	Avg. element quality	Avg. skewness	Avg. aspect ratio
Tet10, Hex20	5854	17333	0.5864	0.513	3.9884

These meshing results were of an unacceptable quality. Thus, the refinement of the mesh was necessary. A process of trial and error was undertaken, in applying different meshing strategies to the model and assessing the resulting statistics. Upon application of these various strategies, the model could be analysed for points of poor quality in a localised scope, such that particular refinement methods could be applied. A description of the iterative processes is shown in Table 5.

Table 5: Details of iterations

Iteration	Description
1	Application of overall element size = 5mm
2	Above + body sizing (Loft floor timber) = 4mm
3	Above + face sizing (Weld face) = 2mm
4	Above + Edge sizing (edge connections of rod to bottom and top saddle) = 2mm
5	Above + Hex dominant loft floor timber support
6	Above + body sizing of upper saddle = 4mm

7	Above + body sizing of bottom saddle = 4mm
8	Above + cartesian method to rod
9	Above + body sizing of rod to 1mm
10	Above + body sizing of insulation block = 10mm
11	Hex dominant method to insulation block
12	Suppress both hex dominant methods
13	Un-suppress hex dominant application to loft floor timber
14	Apply body sizing to loft floor timber = 8mm, apply body sizing to upper saddle = 6mm, apply body sizing to room ceiling and loft floor = 10mm, apply body sizing to rod = 5mm, apply body sizing to foundation timber = 2.5mm

As a result of successive iterations, the overall meshing statistics changed accordingly. After careful assessment of the aforementioned factors a final acceptable mesh was arrived upon. Details of the mesh statistical changes are detailed in Table 6, with the final mesh result depicted in Figure 49.

Table 6: Statistical changes of mesh through iterations

Iteration	Element type	No. of elements	No. of nodes	Avg. element quality	Avg. skewness	Avg. aspect ratio
1	Tet10, Hex20, Wed15	21582	50107	0.70477	0.42051	2.4942
2	Tet10, Hex20, Wed15	22761	52092	0.7064	0.4202	2.4822
3	Tet10, Hex20, Wed15	24027	54311	0.70332	0.42498	2.4897
4	Tet10, Hex20, Wed15	24073	54431	0.70249	0.42632	2.4906
5	Tet10, Hex20, Wed15, Pyr13	26539	74608	0.71622	0.41347	2.8391
6	Tet10, Hex20, Wed15, Pyr13	29980	80542	0.74924	0.36277	2.6483
7	Tet10, Hex20, Wed15, Pyr13	31115	82647	0.7553	0.35396	2.607
8	Tet10, Hex20, Wed15, Pyr13	31018	82046	0.75473	0.35309	2.6146
9	Tet10, Hex20, Wed15, Pyr13	36162	107590	0.77817	0.33371	2.4232
10	Tet10, Hex20, Wed15, Pyr13	35451	105029	0.79691	0.30488	2.3643
11	Tet10, Hex20, Wed15, Pyr13	29896	99736	0.78921	0.32176	2.5651
12	Tet10, Hex20, Wed15	32985	84852	0.79293	0.30614	0.79293

13	Tet10, Hex20, Wed15, Pyr13	22037	62538	0.8266	0.2529	1.9837
14	Tet10, Hex20, Wed15, Pyr13	26519	81823	0.85646	0.21066	1.8246

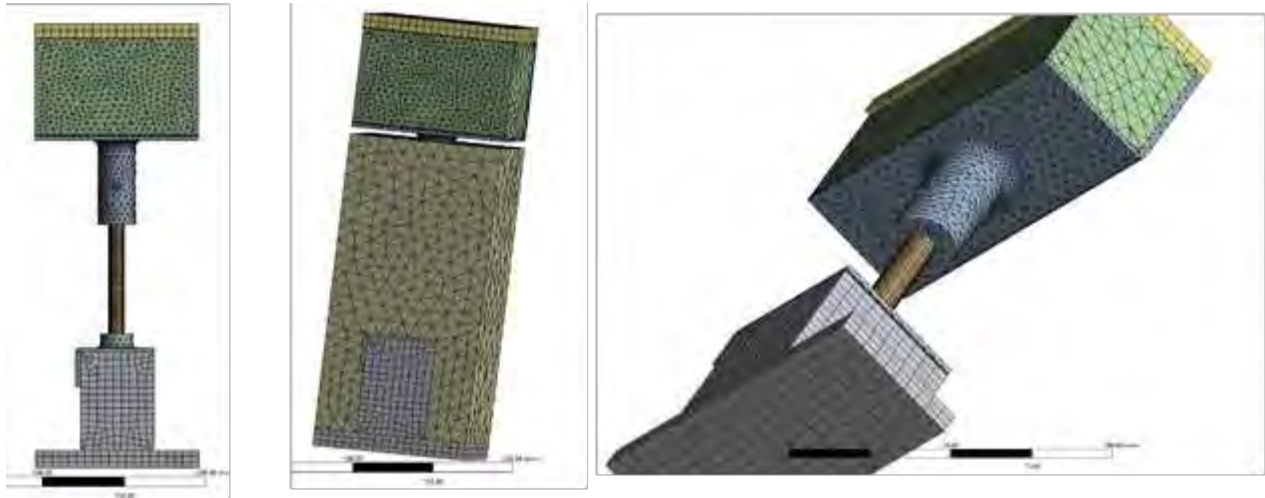


Figure 49: Final meshing of component

5.2. Steady State Thermal

5.2.1. Boundary Conditions and Configuration

The simulation was organised such that it was representative of the physical conditions that the loft leg would operate in. As depicted prior in the block diagram, Figure 47, there will be a temperature differential between the room below and the loft space, with heat being transferred through the ceiling to the loft via the layers and the component layers. Thus, the ANSYS steady state thermal simulation was set such that these conditions were represented.

Thermal conditions were set such that the bottom face of the model, the room ceiling, and the top face of the model, the loft floor, had different temperatures. The room below was assumed to be standard room temperature of 22°C and the loft to be a value of 2°C, this temperature differential was to set an initial benchmark for the first results of the simulation. Later goals of this model were to provide the temperature variation across the component for a range of temperature differentials, such to be representative of regular seasonal temperature fluctuations but also irregular extremities. The model thermal configuration is depicted in Figure 50.

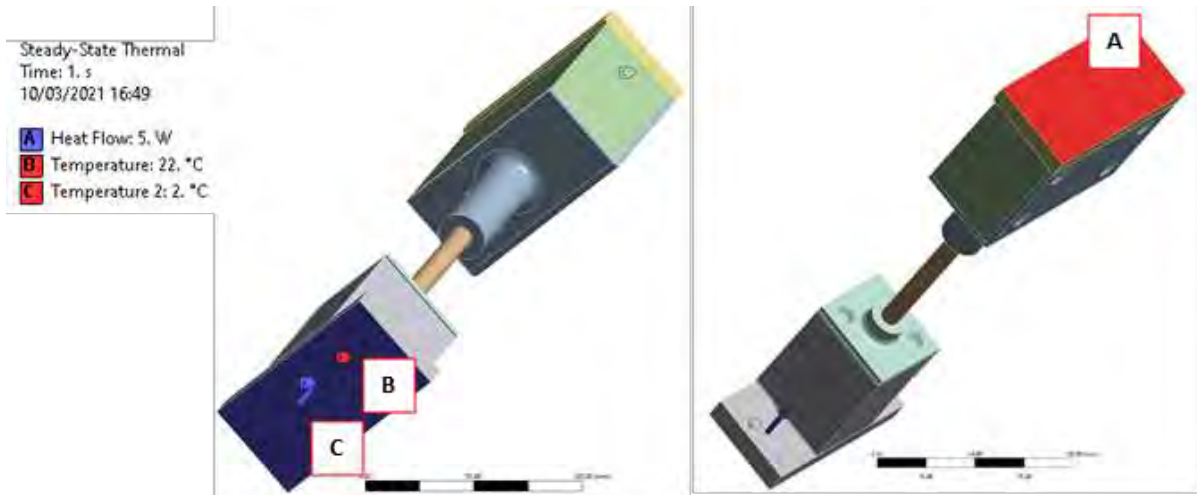


Figure 50: Thermal model conditions configuration

The labelled sections A through C in Figure 50 detail the application of temperatures in the model. The applications are as follows:

- Position A, representing the ceiling of the room below, utilises a temperature application of 22°C.
- Position B, representing the loft floor, utilises a temperature application of 2°C
- Position C, is a face application to the ceiling layer with a benchmark heat flow of 5W

Next, the appropriate material properties must be applied to each respective component layer of the model, such that the actual thermal conductivity of the component is representative of the actual product. Thus, utilising the data provided by ANSYS as well as manual input of thermal conductivity values provided by the company, the inputted material properties and respective assignments are detailed in Table 7.

Table 7: Material assignment and properties

Model component	Material assigned	Thermal conductivity value	Unit
Upper saddle	Structural Steel	60.5	W m ⁻¹ C ⁻¹
Rod	Structural Steel	60.5	W m ⁻¹ C ⁻¹
Lower saddle	Structural Steel	60.5	W m ⁻¹ C ⁻¹
Loft floor timber	Oak Wood	0.4528	W m ⁻¹ C ⁻¹
Foundation timber	Oak Wood	0.4528	W m ⁻¹ C ⁻¹
Loft floor	Oak Wood	0.4528	W m ⁻¹ C ⁻¹
Ceiling	Plasterboard	0.19	W m ⁻¹ K ⁻¹
Insulation material	Custom Insulation Material	0.044	W m ⁻¹ K ⁻¹

5.2.2. Simulation Results

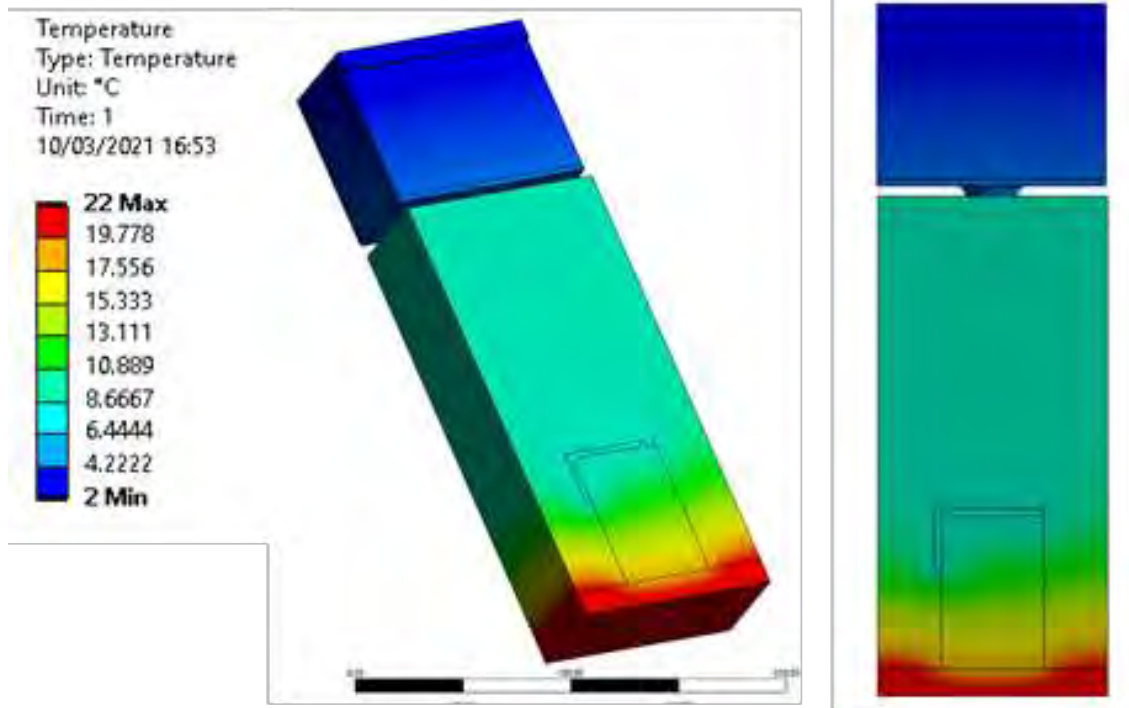


Figure 51: Thermal model temperature results (with insulation layer)

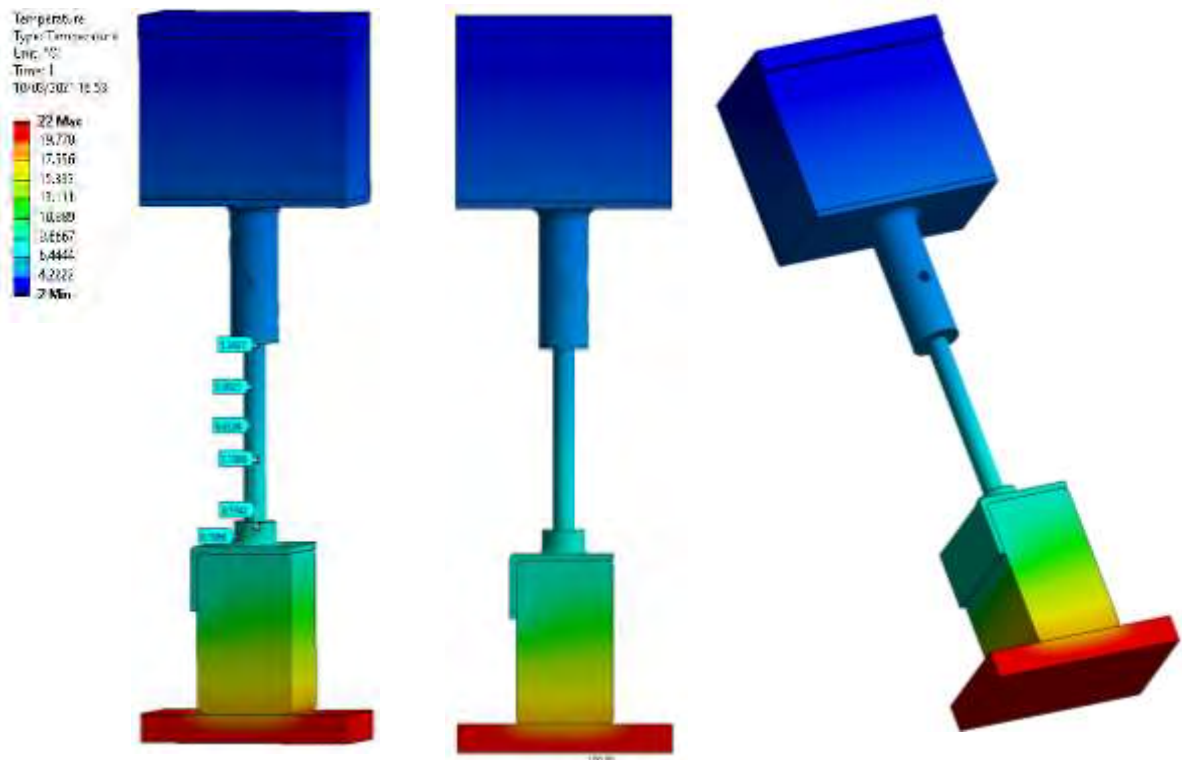


Figure 52: Thermal model temperature results (hidden insulation layer)

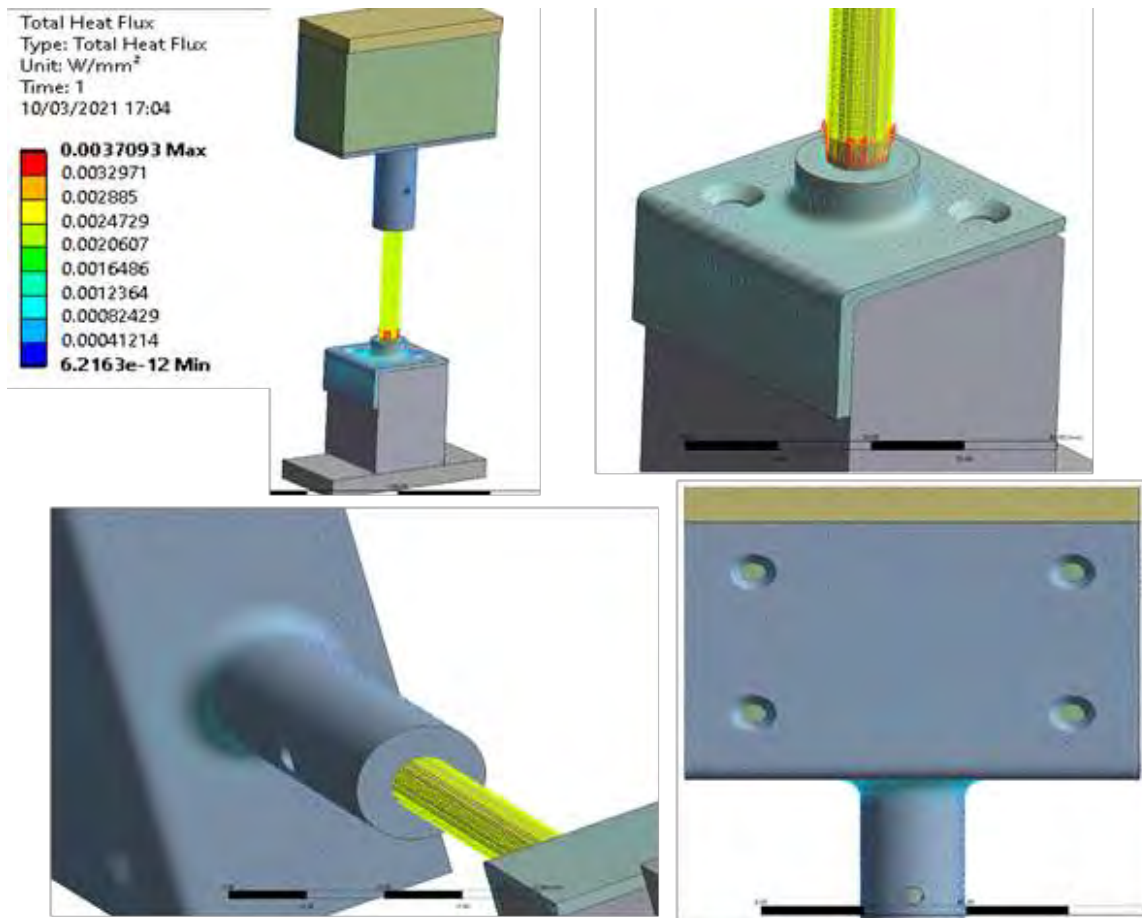


Figure 53: Direction of total heat flux through component

The initial results obtained from the fully meshed model are detailed in Figure 51 through Figure 53. The temperature varied as expected, with a sharper increase in temperature drop across the foundational timber truss member and bottom saddle of the component. The component demonstrated a steady decline in temperature with distance from the bottom surface, reaching equilibrium with the loft space temperature at the top surface of the model. In contrast, the insulative material fulfilled its purpose and demonstrated a lesser magnitude in temperature gradient from the bottom surface to the top. The heat flux vectors depicted in Figure 53 demonstrate that the component geometry creates concentrations of heat flow from the bottom saddle, which reach a significant magnitude at the boundary between the bottom saddle and the rod. The rod then acts as the most significant conduit for heat flow from the bottom surface to the top. Further, it can be demonstrated by the resulting thermal error in the model, depicted in Figure 54, that the results can be considered accurate. The maximum error region of the model occurs in a region of little priority, therefore, can be ignored.

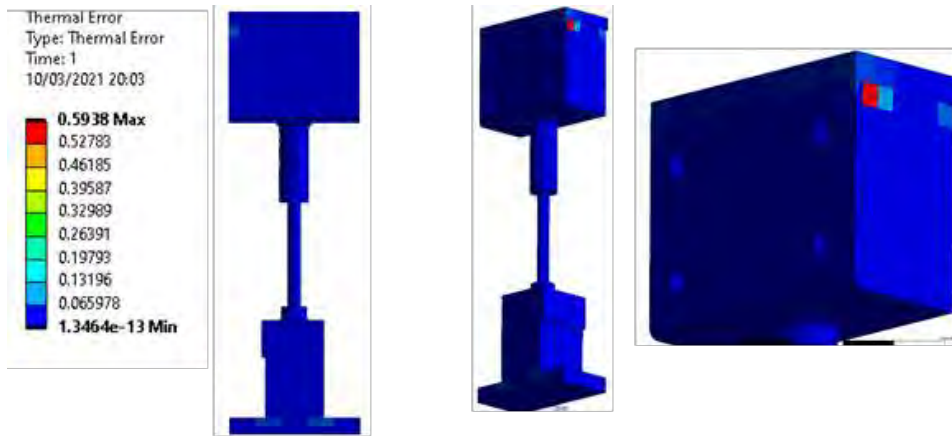


Figure 54: Thermal error in the model

With analysis of the initial data it can be noted that the sections, starting from the bottom layer through to the top of the bottom saddle demonstrate the largest temperature gradient. The results show a temperature difference between the plasterboard ceiling and the bottom saddle to be in the region of 14°C. Thus, it is noted that this section is an area of interest for implementing consideration regarding the optimisation for thermal retention. However, it is also useful to obtain a range of data such to ensure this temperature behaviour is echoed for a range of temperature differential settings, in the same simulation configuration. Figure 55 demonstrates the same simulation but for different temperature differentials.

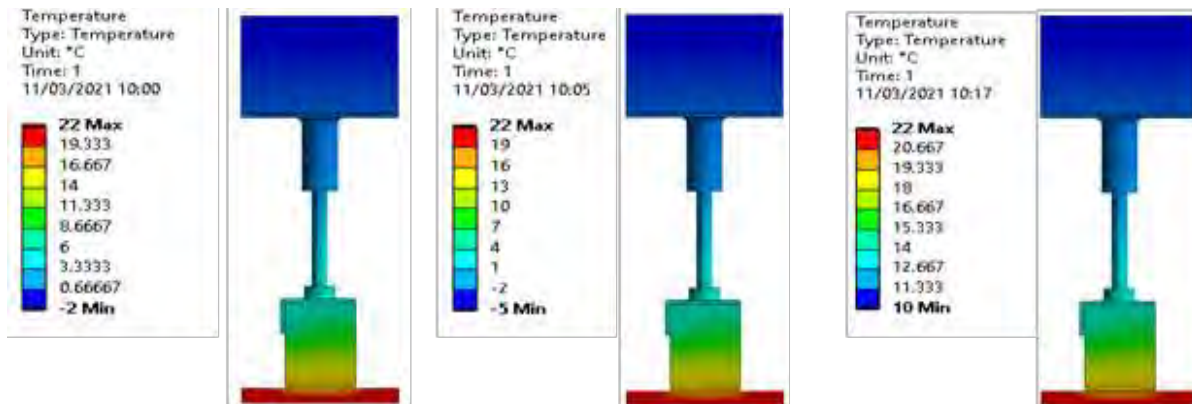


Figure 55: Thermal distributions for a range of temperature differentials

It is demonstrated in Figure 55, that the identical magnitudes of temperature distribution occur for a range of thermal data. With these results in mind, now provides confirmation that no matter the temperature differential, the distribution will be the same for the geometry. Thus, it is now necessary to begin thinking of how the design should be optimised. The simulation configuration outlined in Figure 50 is representative of the realistic conditions, with the component experiencing significant heat flow via the connecting timber support and surrounding insulative material. The insulation acted as intended, retaining more heat demonstrated with the smaller temperature difference from the room ceiling to the top of the insulation. The peak flow of heat flux is concentrated across the rod of the component, therefore showing an area to address for investigation of lower thermal conductivity. Further, with the greatest temperature drop occurring across the timber support, the lower saddle demonstrates the first point of contact that could demonstrate a better performance regarding reducing further heat loss further

up the component. Therefore, the main conduit of heat loss was identified as the route through the component from top to bottom of the model.

As a result, it was necessary to perform an isolated simulation of the component, disregarding the timber connections and other boundaries, such that the thermal performance of the component alone could be assessed. A similar meshing strategy was utilised on the component, simply by suppressing all other externally connecting bodies and editing the mesh accordingly. Further, a similar simulation configuration was set, with the same temperature differential applied. The details of this mesh are outlined in Table 8. The differing temperatures were placed across the component rather than across the faces of the ceiling and loft floor. Thus, the thermal results for the isolated component were obtained, the result of which are shown in Figure 56.

Table 8: Isolated component meshing statistics

Element type	No. of elements	No. of nodes	Avg. element quality	Avg. skewness	Avg. aspect ratio
Tet10, Hex20	35337	72684	0.80386	1.9572	0.29187

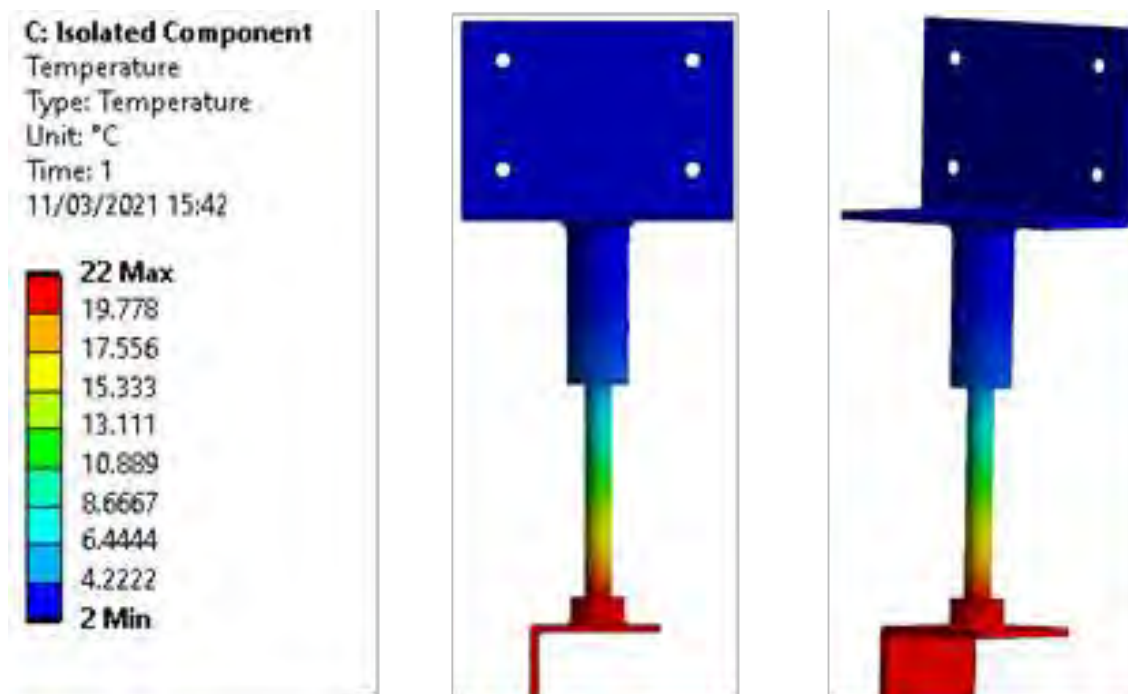


Figure 56: Thermal distributions for isolated component

As the results in Figure 56 demonstrate, the maximum temperature gradient occurs via the rod of the component. These results, coincide well with the flux results demonstrated in the prior full model simulation, showing maximum heat flux concentration through the rod of the component. Thus, confirming this region as an area for potential optimisation.

5.2.3. Design Optimisation

The main solution to improving the thermal retention of the component is to recommend the usage of different materials, with a lower thermal conductivity value. Thus, the prior models can be utilised in the same configuration but with different material applications to the component. A consideration of a variation of different materials were considered for the following simulations, the details of these materials are outlined in Table 9. The outlined materials were then applied to the previous full model, with the same temperature difference application of 22°C-2°C. The resulting thermal performances are depicted in Figure 57 and Figure 58.

Table 9: Material properties of chosen material range

Material	Isotropic thermal conductivity ($W\ m^{-1}\ ^\circ C^{-1}$)
Structural Steel	60.5
Stainless Steel 316	14.58
Carbon Steel 1020, annealed	54.1
Concrete	2.933
Copper, C10100, hard	396.7
Titanium Alloy, Ti-6Al-4V	7.187
Low alloy Steel, 4140, normalised	43.33

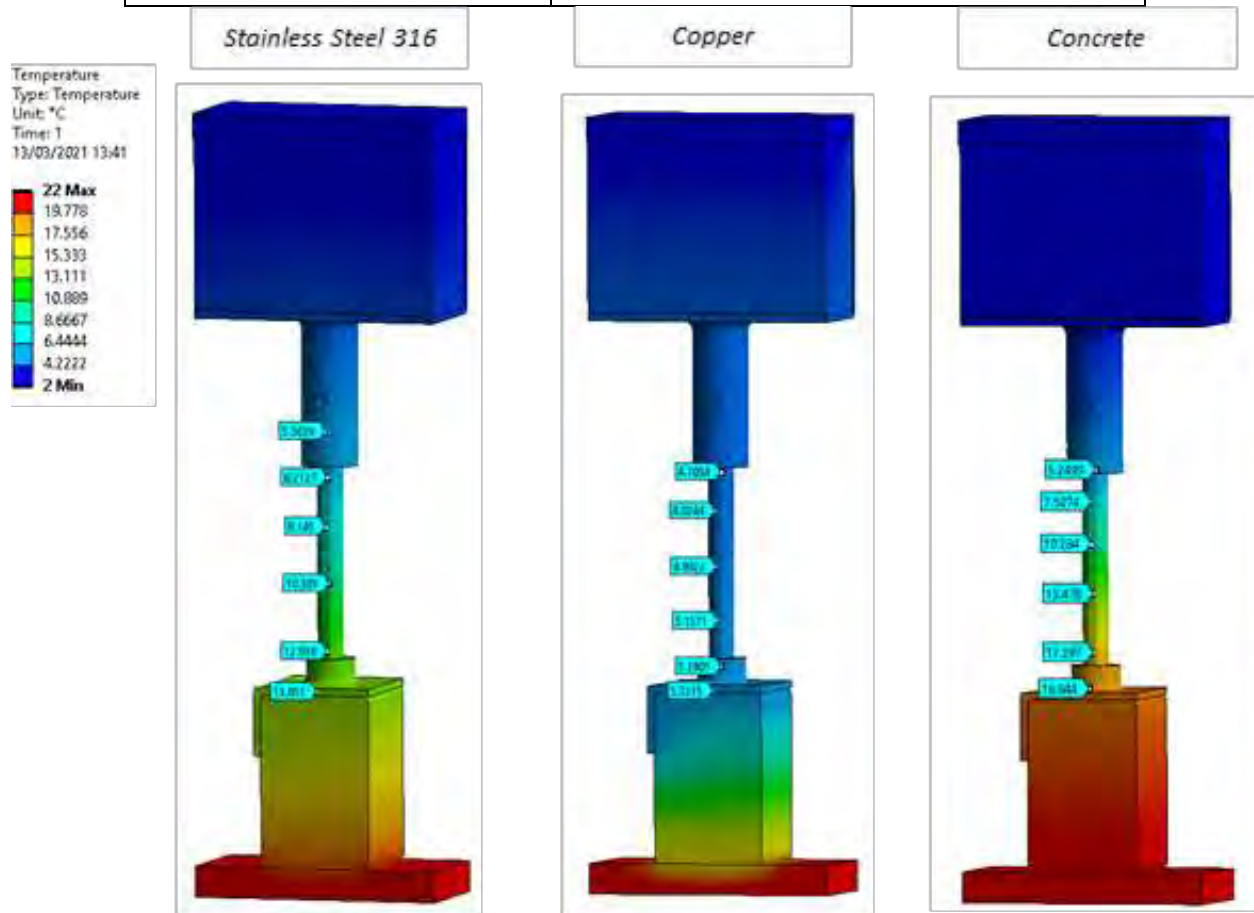


Figure 57: Temperature distribution results for the range of selected material applications

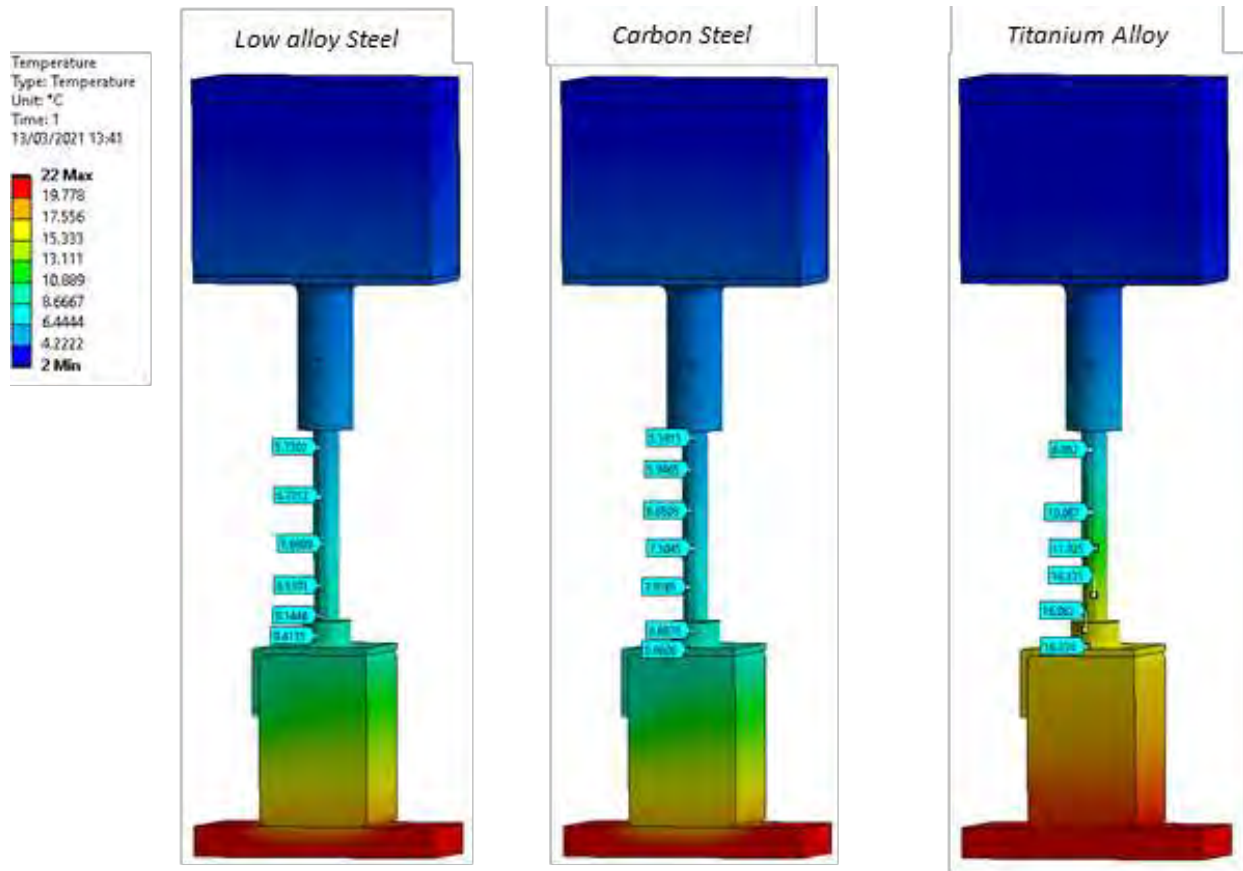


Figure 58: Temperature distribution results for the range of selected material applications

From the observations of the results of these thermal simulations, it can be noted that some materials did perform better relative to others. As a benchmark, the standard structural steel utilised in the initial simulations, results of which are demonstrated in Figure 51, demonstrated a temperature difference from the bottom saddle to the tip of the rod of around 3.15°C. A comparison of the different material performances was conducted utilising sampling probe points at different sections along the component. Figure 59 details the approximate areas these probe points were taken from, such that the resulting data points could be compared in Table 10 and result in the comparative results graph in Figure 60.

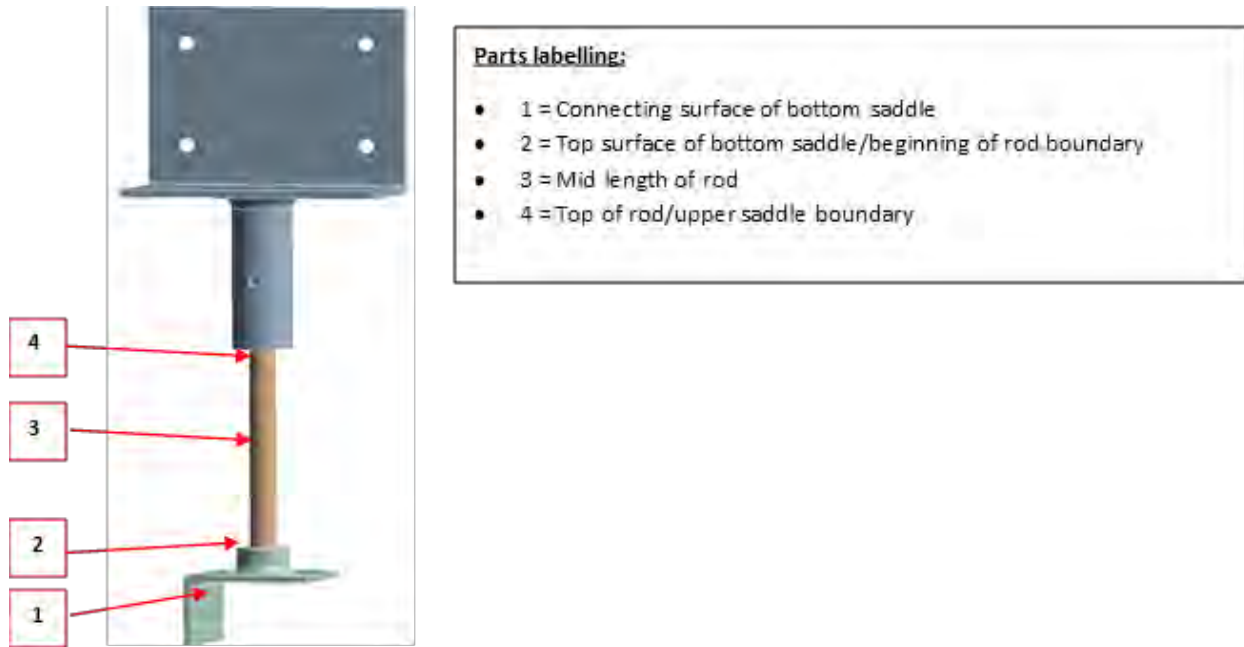


Figure 59: Labelled sampling probe points for data comparison

Table 10: Material thermal performance data

		Data Point			
Material	Temperature / °C	1	2	3	4
Structural Steel		8.5373	8.2669	6.7235	5.1329
Stainless Steel 316		13.853	13.427	9.6983	5.7629
Carbon Steel, 1010, annealed		8.8634	8.5879	6.8822	5.1707
Concrete		19.155	18.509	11.986	5.2558
Copper, C10100, hard		5.3215	5.2887	4.9716	4.6734
Titanium Alloy, Ti-6Al-4V		16.566	16.02	11.013	5.538
Low Alloy Steel, 4140, normalised		9.5899	9.367	7.4016	5.2519

Temperature differential results from sample points

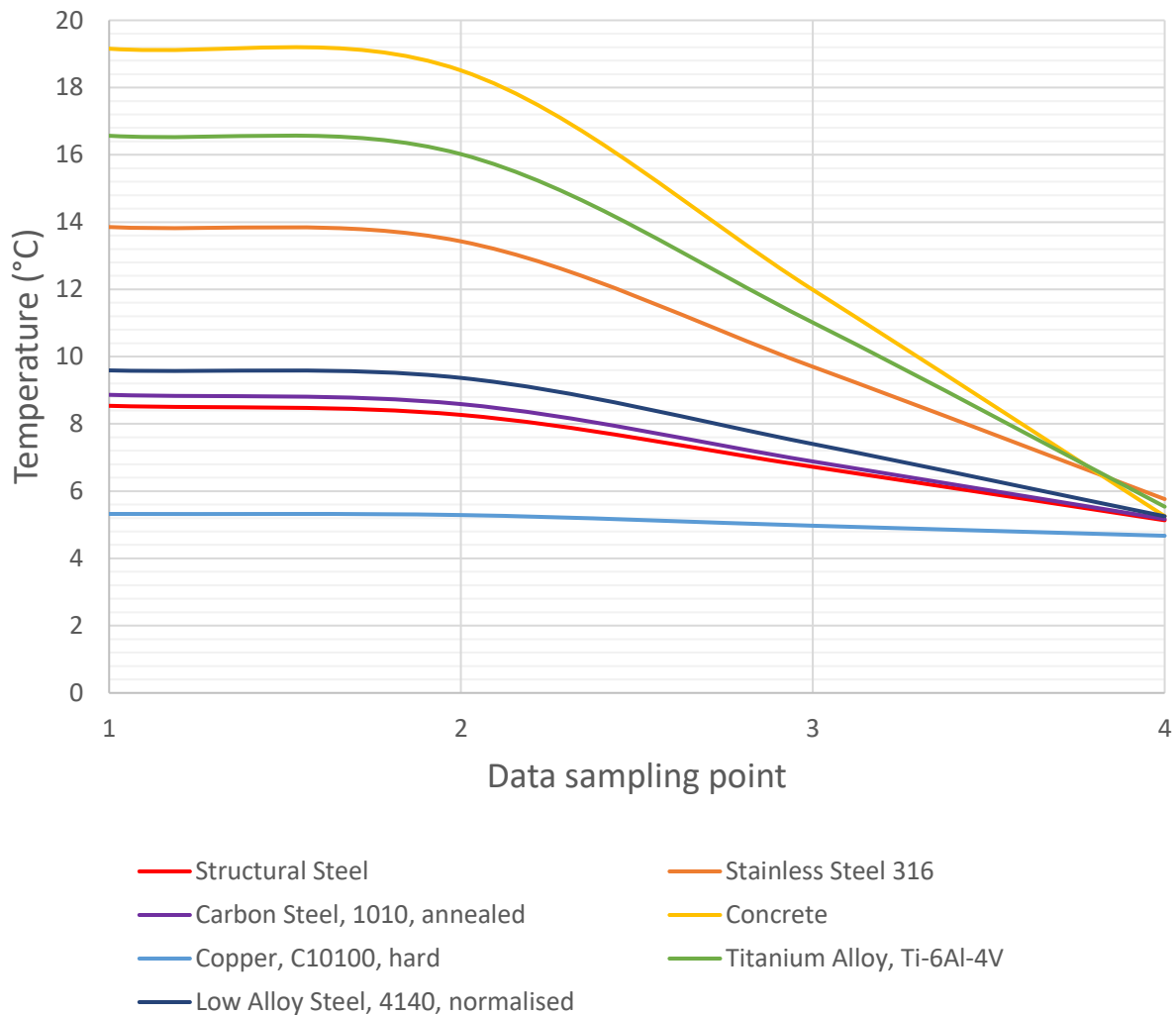


Figure 60: Temperature differential results from sample points

It can be seen from the results that the materials demonstrated a large spread of initial temperatures as the base of the bottom saddle, with all trends showing convergence towards 5°C. The initial spread at the first data point is a useful indication of the material's ability to withhold heat from the bottom ceiling and foundational timber, with a higher temperature in figure 13 demonstrating a better ability for heat retention. The higher value means that the resulting temperature from the timber-ceiling transfer has been retained through the bottom saddle, due to the material's conductive properties. All materials show the similar trend and converge towards the 5°C region, this is expected as thermal equilibrium will always be met closer to the top of the component where there is less insulative material. Recommendations to the design optimisation will be summarised in the concluding section of this report.

It should be noted that some materials utilised can be deemed unrealistic due to either it's impracticalness for use in the component or that the material is known to have a worse thermal conductivity value than the default structural steel. However, these materials were still included such to obtain a good spread of

data for comparison. Such materials that may be deemed impractical include the use of Concrete and Copper.

5.3. Thermal Expansion

As there is a temperature difference between the floors of the house and the loft, it is expected that the material would undergo a change in size in response to a change of temperature. The relationship of thermal expansion depends on the change of length, change in temperature and its initial length as in equation 1 assuming linear expansion. (The Physics Hypertextbook, n.d.)

$$\alpha = \frac{1}{L_0} \frac{\Delta L}{\Delta T} \quad \text{Equation 1}$$

Where:

α – Thermal Expansion ($^{\circ}\text{C}^{-1}$)

L_0 - Initial Length (m)

ΔL – Change in Length (m)

ΔT – Change in Temperature ($^{\circ}\text{C}$)

Simulations were set up to replicate what could occur with a temperature of 22°C located at the bottom of the plasterboard and a temperature of 2°C at the top of the timber to replicate the cold loft conditions to understand the effects of thermal expansion of the Loft-E device. The results of the deformation of the loft with and without the attachments are displayed below in Figure 61 and Figure 62 these can be compared to understand how the loft support functions individually and as a group.

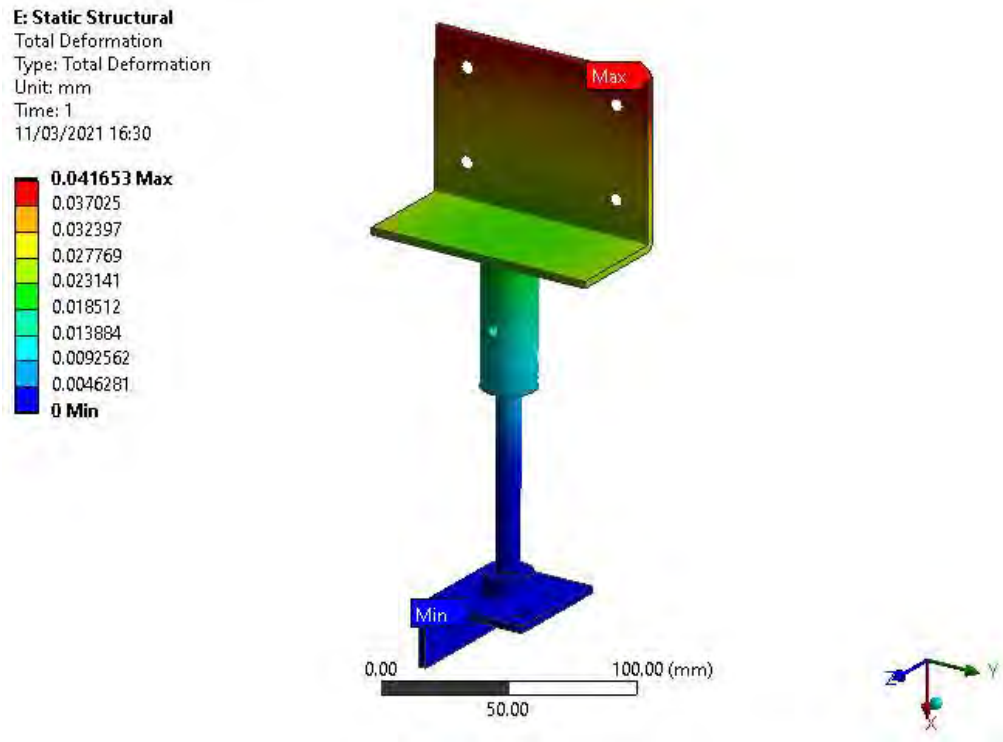


Figure 61: Total Deformation of Loft Support without attachments

C: Static Structural
 Total Deformation
 Type: Total Deformation
 Unit: mm
 Time: 1
 11/03/2021 16:34

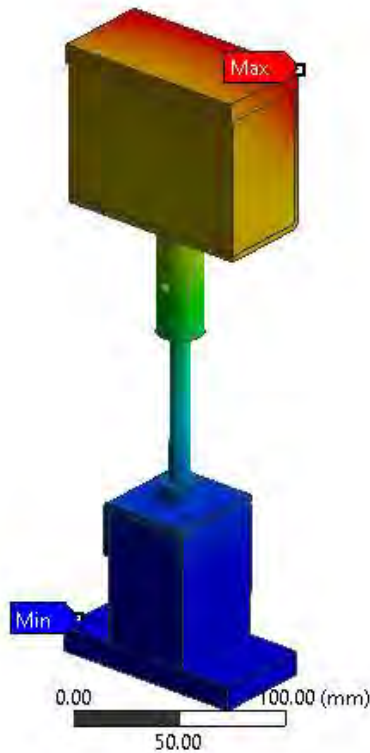
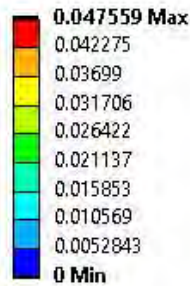


Figure 62: Total Deformation of Loft Support with attachments

As seen in the results of deformation, the maximum deformation occurs at the top due to the material constricting through colder temperatures at the top half of the loft. However, the deformation produced is very small thus would not be noticeable in the loft.

5.4. Thermal Stress

Thermal expansion also has an effect as to how much stress is applied to the loft via thermal effects as derived from equation 1:

$$\alpha = \frac{1}{L_0} \frac{\Delta L}{\Delta T}$$

Equation 2 defines the strain:

$$\varepsilon = \frac{\Delta L}{L_0} \quad \text{Equation 2}$$

Equation 3 defines the elastic modulus or Young's modulus:

$$E = \frac{\sigma}{\varepsilon} \quad \text{Equation 3}$$

Therefore, Thermal Stress:

$$\sigma_{dt} = E\varepsilon$$

$$= E * \frac{\Delta L}{L_0}$$

$$= E * \alpha * L_0 * \Delta T * \frac{1}{L_0}$$

$$\sigma_{dt} = E\alpha\Delta T$$

Equation 4

Where:

σ_{dt} – Stress due to change in temperature (Pa)

E – Elastic Modulus (Pa)

α – Thermal Expansion ($^{\circ}\text{C}^{-1}$)

ΔT – Change in Temperature ($^{\circ}\text{C}$)

(The Engineering ToolBox, n.d.)

Like in the thermal expansion section, comparisons between the loft support individually and as a group can be carried out. As seen in Figure 63 the largest stress is located at the rod in the area within the boss where the view hole is. Adding on the plasterboard and the timber, most of the stress applied are located on the saddle and foot of loft support with the rod and boss not really experiencing a larger amount of stress. As the maximum stress is embedded within the saddle, the component was set to hidden and the stress is more clearly displayed in Figure 64. Overall, the stress produced on the loft said to not be significant to affect the performance of the loft support when isolated.

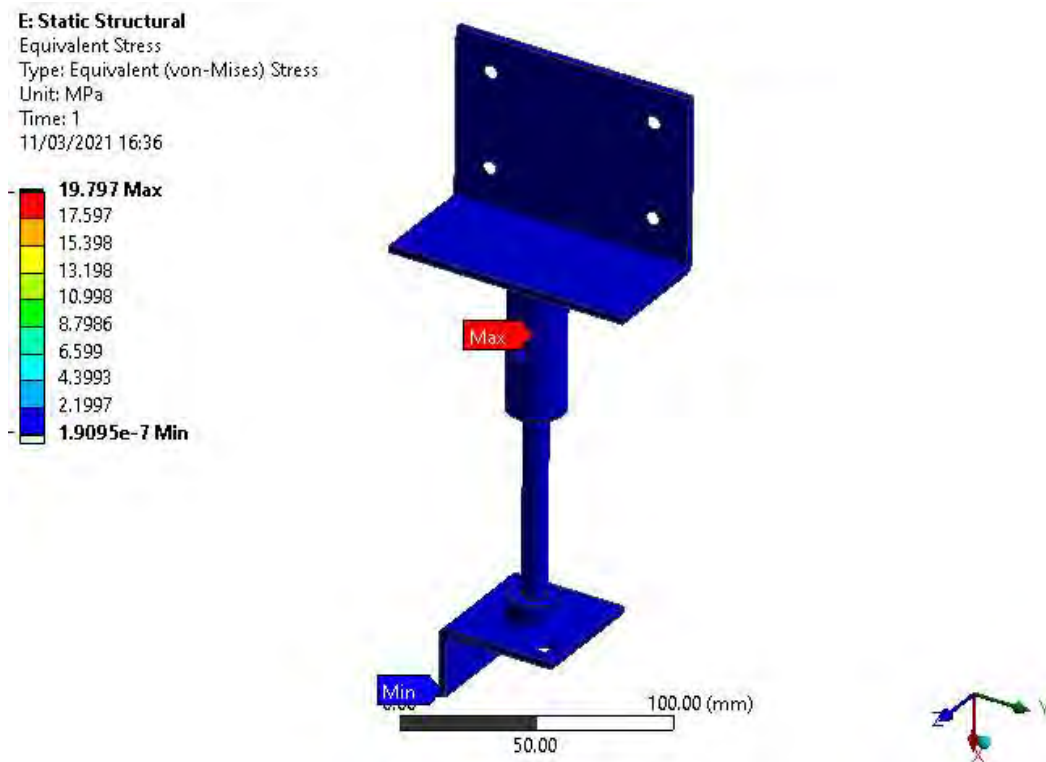


Figure 63: Equivalent Stress of Loft Support Without Attachments

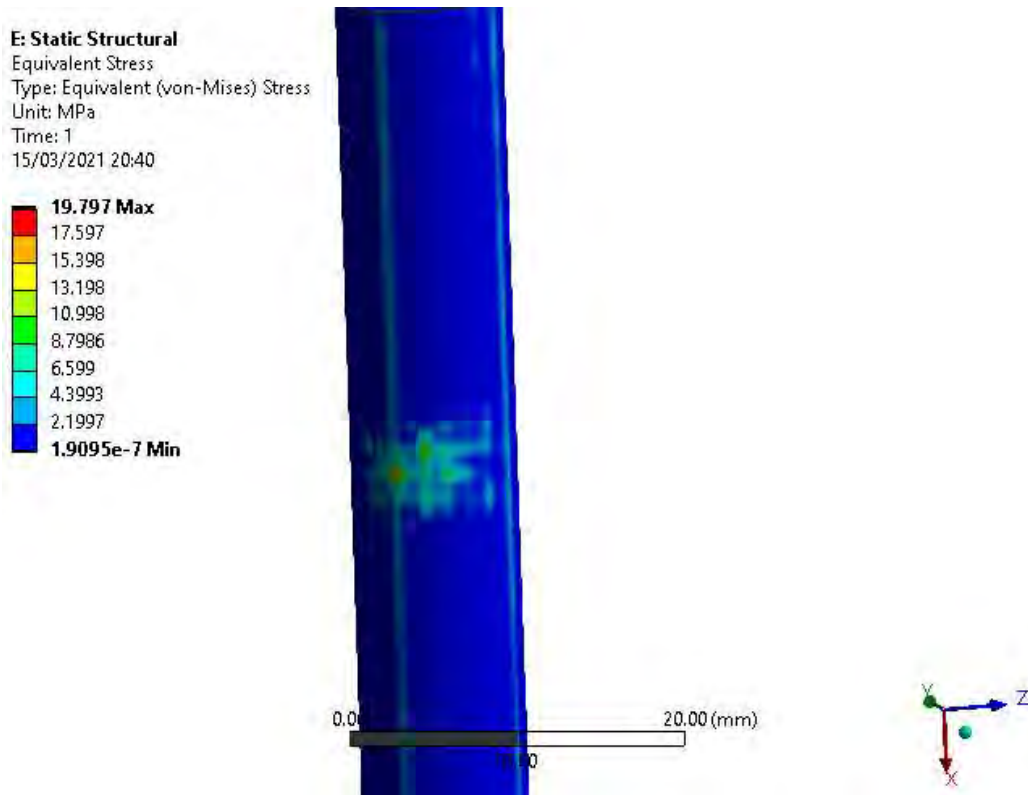


Figure 64: Close up of rod with saddle hidden.

By inserting the attachments onto the loft support, Figure 65 shows the stress the loft support undergoes with the thermal conditions. The saddle and foot of the loft are the areas of highest stress due to the temperature going through the change in material of lower thermal conductivity to a higher thermal conductivity of the sections between the timber and the foot of the loft support. The same applies between the boss and the saddle thus displaying the higher levels of stress.

Note that material data for plasterboard and loft had to be inputted to ensure that the static structural simulations ran. The isotropic elasticity of the loft had to be derived using Young's modulus and Poisson's ratio which were said to be 72000MPa and 0.21 (Azo Materials, n.d.). For the plasterboard, the Young's modulus and Poisson's ratio were said to be 250MPa and 0.3 respectively (S. M. Cramer, 2003). For the likes of wood and structural steel, the data was provided by ANSYS workbench.

C: Static Structural

Equivalent Stress

Type: Equivalent (von-Mises) Stress

Unit: MPa

Time: 1

11/03/2021 16:37

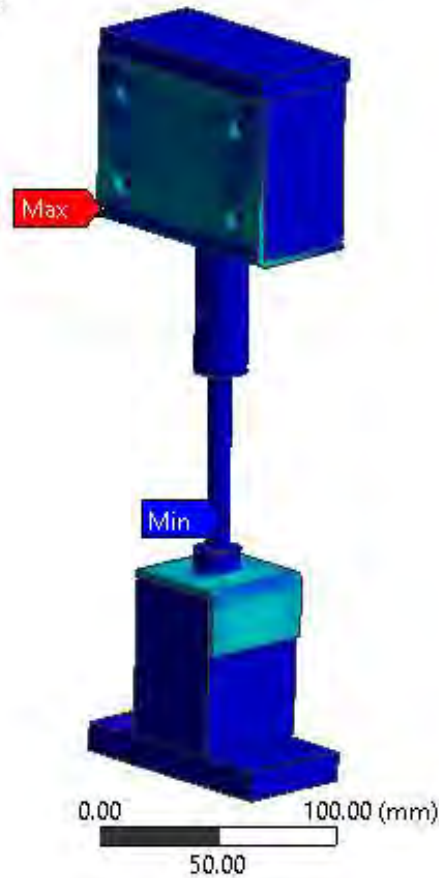
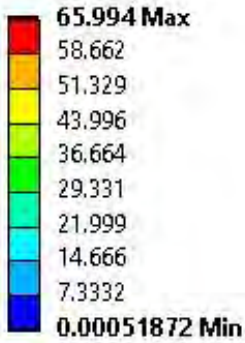


Figure 65: Equivalent Stress of Loft Support With Attachments

Figure 66 shows a closer view of where most of the stresses are located. It appears that the rod and boss are not significantly affected however the saddle and foot are the most affected. This could be due to how the structural steel has a much higher thermal coefficient than wood in addition to the loft experiencing a change of temperatures at those points as well as having a much higher Young's Modulus than wood thus a larger thermal stress.

C: Static Structural

Equivalent Stress

Type: Equivalent (von-Mises) Stress

Unit: MPa

Time: 1

11/03/2021 16:32

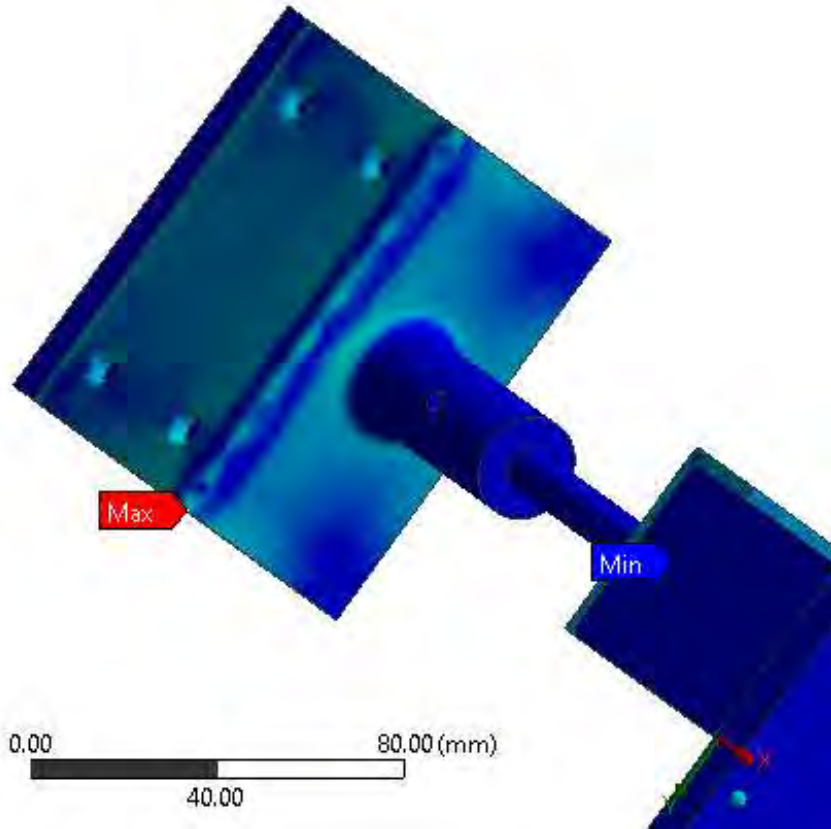
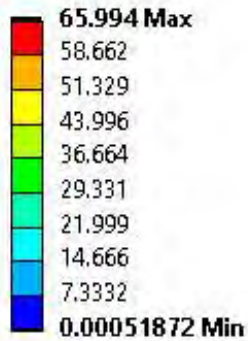


Figure 66: Equivalent Stress Close-Up of Saddle.

5.5. Numerical Calculations

5.5.1. Steady-State Thermal Calculations

One-dimensional steady-state heat transfer is the most basic model of conduction. Using Fourier's basic law of conduction assumes that the temperature is uniform at sections normal to the direction of heat flow and is constant at any location. The direction of heat flow in this case is from the bottom of the leg to the top. Heat transfer (Q) is calculated by dividing the change in temperature (T) of the system by the sum of the thermal resistance (R) for each geometry section.

$$\dot{Q} = \frac{\Delta T}{\sum R} \text{ where } R = \frac{x}{kA}$$

Equation 1

The thermal resistance in between each point shown in Figure 67 was calculated using the heat coefficient of structural steel (k) valued at 0.0605W/mm.K .

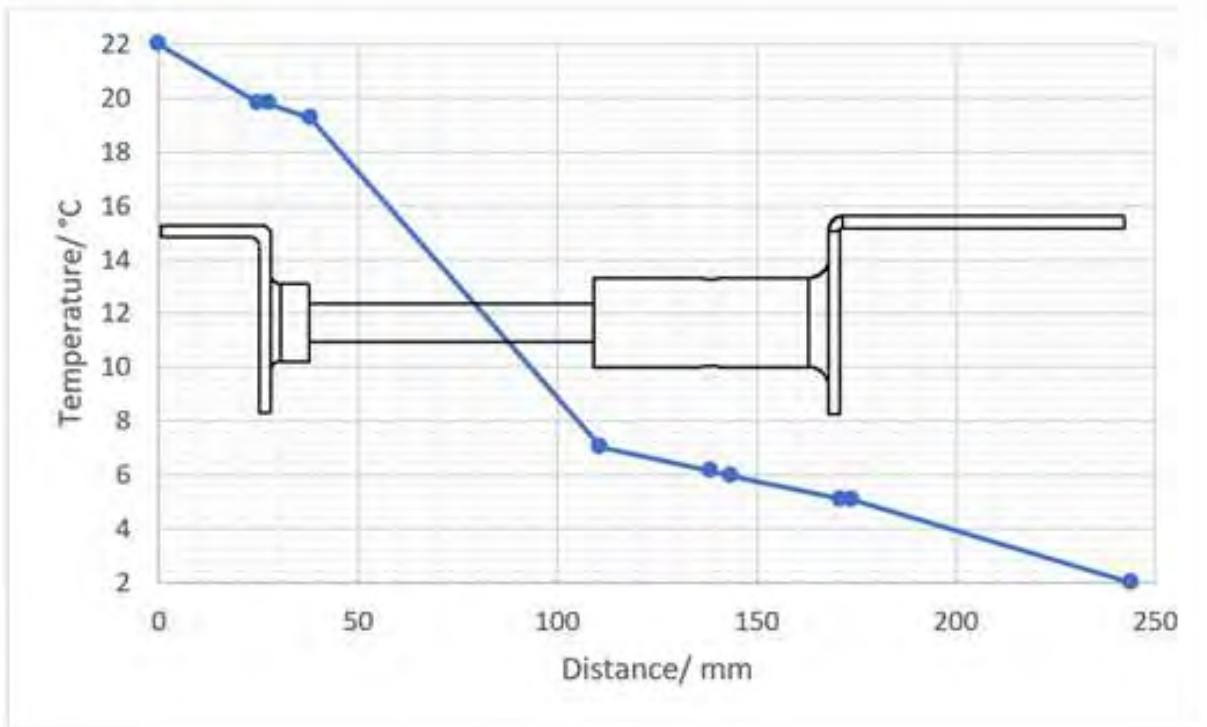


Figure 67: Temperature at Each Point in the Geometry Compared to Distance.

As the law of steady-state thermal heat transfer states that is constant throughout the model. Using this, the temperature at a certain point can be calculated from the individual resistance of the geometry using equation 2 below.

$$T_2 = T_1 - \dot{Q}R \text{ where } T_2 < T_1$$

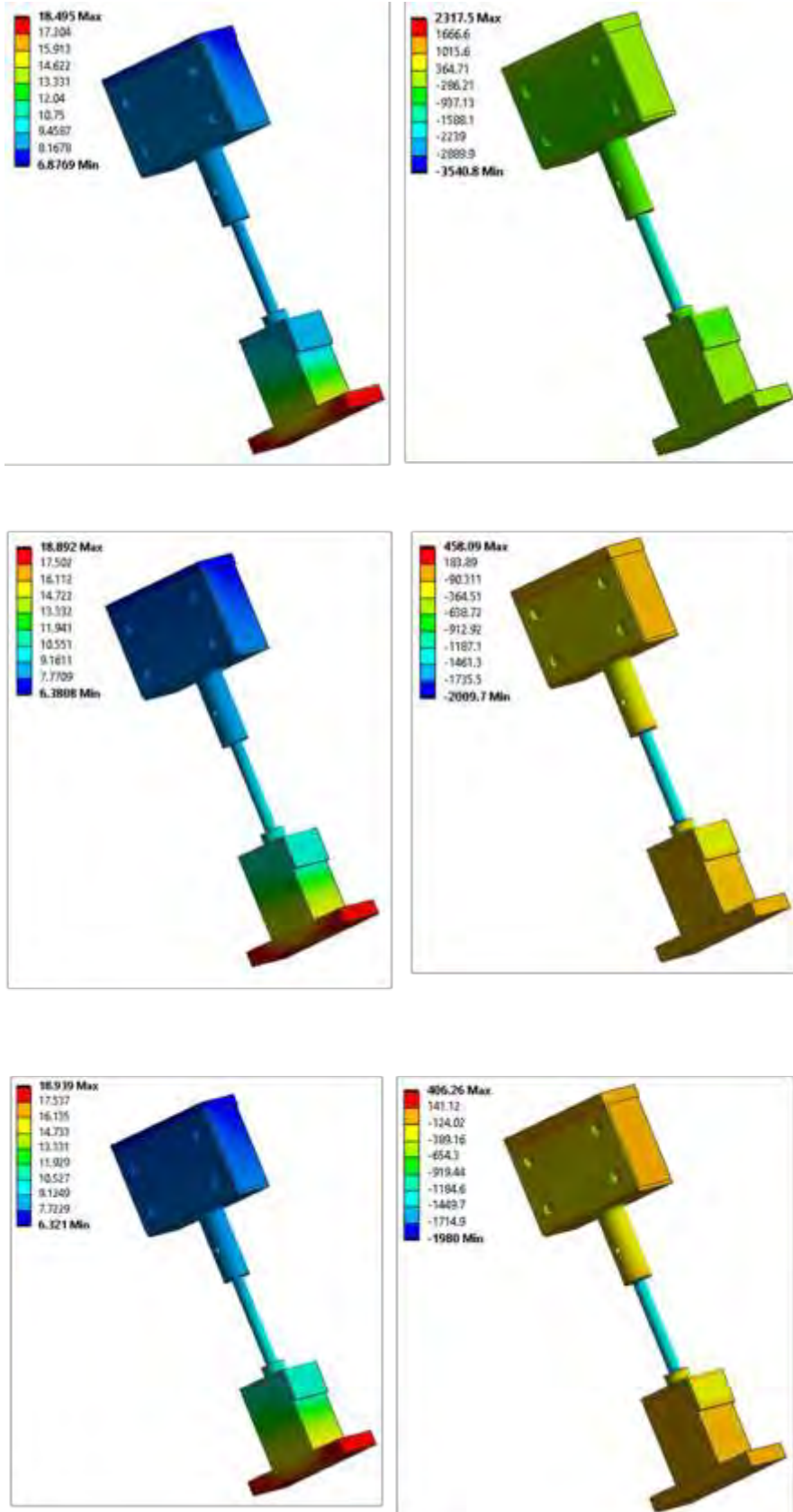
Equation 2

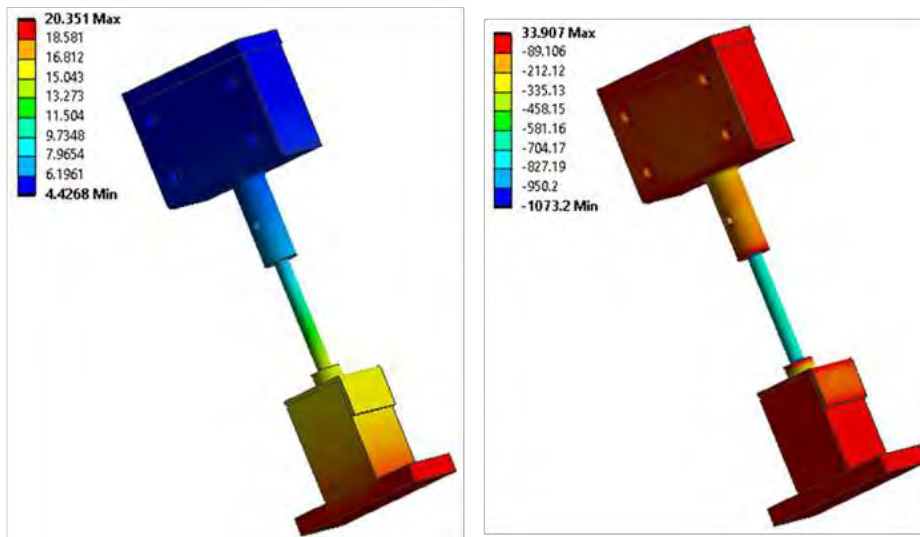
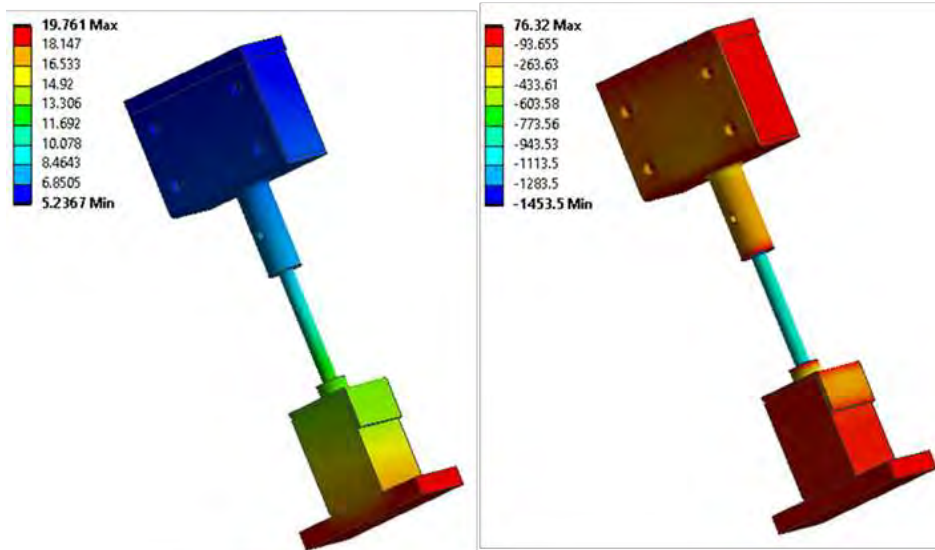
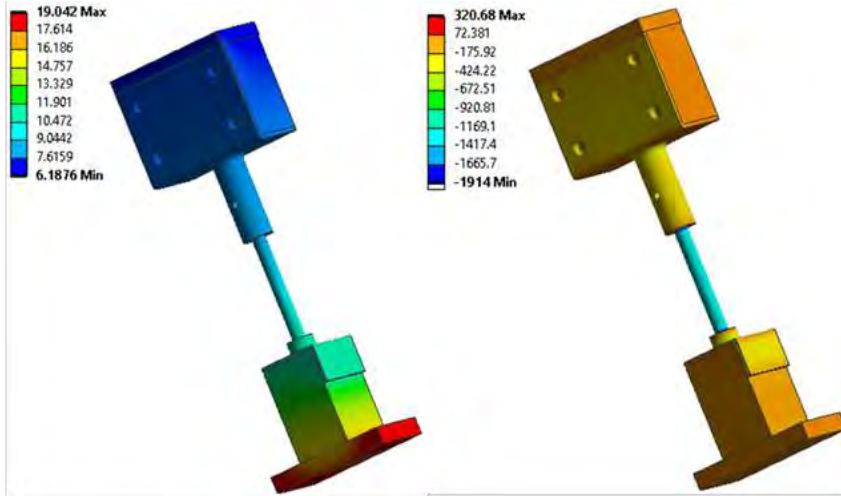
5.6. Further Thermal Simulation- Ambient Temperatures and Directional Heat Flux

5.6.1. Motivation and Methodology

Further simulation work was done on the loft support model, simulating the effect of ambient temperatures at either end of the support to find directional heat flux values. The ambient temperatures were 22°C at the bottom of the support and 2°C at the top. This was done to emulate the real-world conditions more accurately than a model with fixed temperature values. A key difference of this model is the radiative thermal loads reacting to the emissivity of the surfaces. An emissivity value of 0.9 was used for both the plaster/paint on the bottom edge and the wood on the top layer, meaning that some thermal radiation is reflected, which resulted in a smaller temperature range within the support. Average directional heat flux for each material was found through the simulation, which was used to find the thermal performance of a typical section of loft cavity.

5.6.2. Results





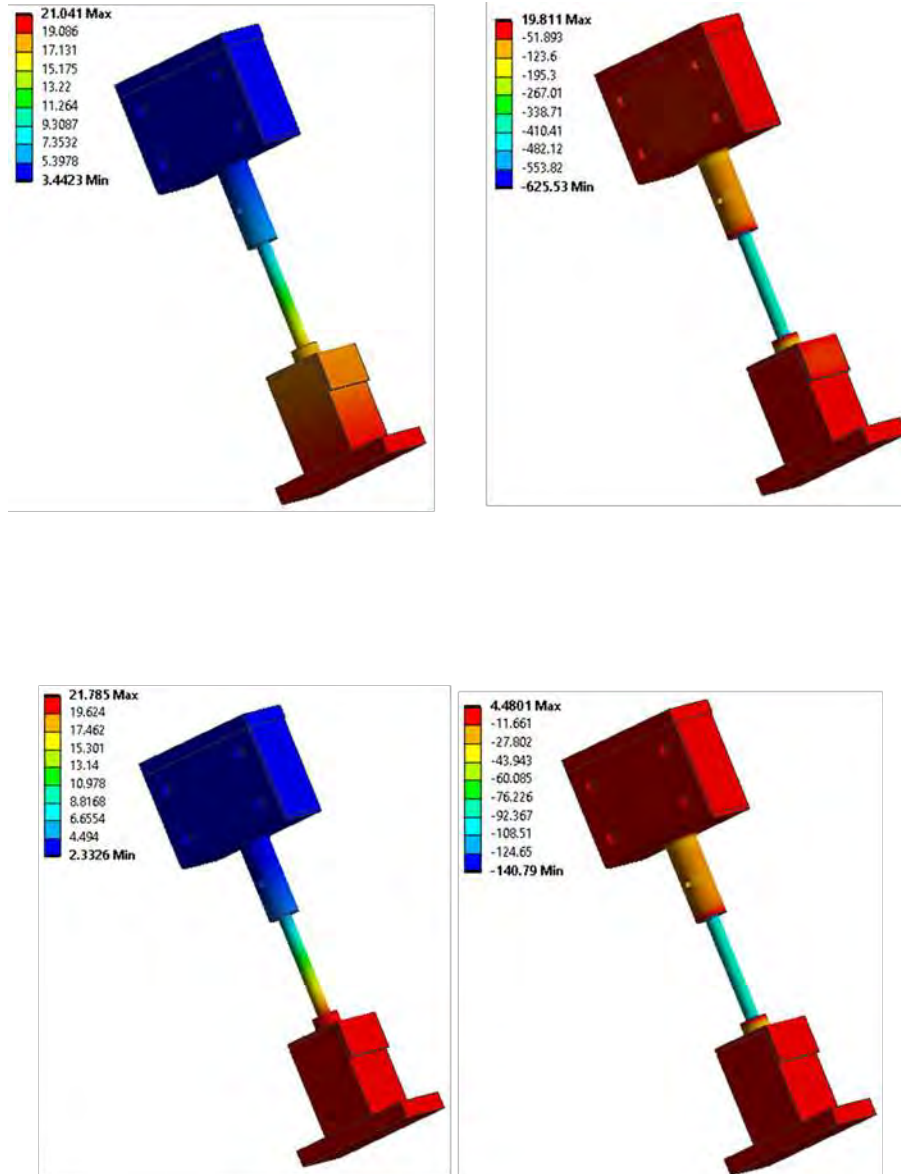


Figure 68: Temperature and directional heat flux simulations on eight materials of decreasing thermal conductivity: copper, structural steel, carbon steel, low alloy steel, stainless steel, titanium alloy, concrete and HDPE. Temperature left, heat flux right

Figure 68 shows the temperatures and directional heat fluxes throughout the support geometry. Directional heat flux was oriented in the x-axis, which points from top to bottom in the model, so a more negative directional heat flux indicates a higher heat flux going up through the support. The results show that as the conductivity of the support decreases, the end-to-end temperature difference increases, showing that less heat travels up the rod at steady state for a less conducting material. The directional heat flux simulations show that as conductivity decreases, the minimum directional heat flux becomes less negative, again showing that less heat travels up through the rod with a less conductive material.

Average directional heat flux values were simulated, with results shown in Table 11.

Table 11: Thermal conductivity and average directional heat flux data for different materials

Material	Thermal conductivity (W/m.K)	Average directional heat flux (W/m ²)
Copper, C10100, hard	396.7	351.21
Structural steel	60.5	309.61
Carbon steel 1020, annealed	54.1	304.78
Low alloy steel, 4140	43.33	294.08
Stainless steel 316	14.58	220.37
Titanium alloy, Ti-6Al-4V	7.187	160.8
Concrete	2.933	92.302
HDPE	0.4811	20.388

5.6.3. Calculations and U values

U values are a measure of thermal transmittance which show how well insulated a structure is. For an existing build, a U value of 0.16W/m².K or less is required for ceiling level insulation.

For these calculations, the case of a single beam in a 0.6m by 1.2m area of loft cavity is used.

Data

A_{total}: Area of loft cavity for one support = **0.72m²**

A₁: Area of support section = **0.005m²**

A₂: Area of insulated section = **0.715m²**

L₁: Thickness of plasterboard and wood = **2 x 0.0125m**

L₂: Thickness of loft insulation material = **0.2915m**

λ₁: Thermal conductivity of plasterboard and wood = **0.19 W/m.K**

λ₂: Thermal conductivity of loft insulation material = **0.044W/m.K**

$\overline{\varphi}_q$: Average directional heat flux: as shown in **Table 11**

T: Temperature difference = **20°C**

U value of fully insulated portion of loft cavity

$$R = L/\lambda$$

Equation 1

$$R_1 \text{ (plasterboard and wood)} = 0.025/0.19 = \mathbf{0.1315789}$$

$$R_2 \text{ (loft insulation)} = 0.2915/0.044 = 6.625$$

$$U_1 = \frac{1}{(R_1 + R_2 + \dots)} \quad \text{Equation 2}$$

$$U_1 = 1/(0.1315789 + 6.625) = 0.148 \text{ W/m}^2\text{K}$$

U value of simulated portion

$$U_2 = \overline{\varphi}_q / T \quad \text{Equation 3}$$

Table 12: U values for different materials

Material	U ₂ value (W/m ² .K)
Copper, C10100, hard	17.56
Structural steel	15.48
Carbon steel 1020, annealed	15.24
Low alloy steel, 4140	14.70
Stainless steel 316	11.02
Titanium alloy, Ti-6Al-4V	8.04
Concrete	4.62
HDPE	1.02

Overall U value

$$U_{\text{overall}} = \frac{U_1 A_1 + U_2 A_2}{A_{\text{total}}} \quad \text{Equation 4}$$

Table 13: Thermal conductivity, average directional heat flux and final U value data for each material

Material	Thermal conductivity (W/m.K)	Average directional heat flux (W/m ²)	U value (W/m ² .K)
Copper, C10100, hard	396.7	351.21	0.2689
Structural steel	60.5	309.61	0.2545
Carbon steel 1020, annealed	54.1	304.78	0.2528
Low alloy steel, 4140	43.33	294.08	0.2491
Stainless steel 316	14.58	220.37	0.2235
Titanium alloy, Ti-6Al-4V	7.187	160.8	0.2028
Concrete	2.933	92.302	0.1790
HDPE	0.4811	20.388	0.1541

5.7. Maximum Thermal Conductivity Calculation

Table 13 shows that none of the metal supports satisfy the U value requirement of 0.16 W/m²K. Further calculations were done to find the maximum thermal conductivity of a material which could be used for the support. To do this, simulations of supports of a range of thermal conductivities were carried out in order to improve the data set, which is shown in Table 14.

Table 14: U values for simulated supports with a range of thermal conductivities

Material	Thermal conductivity (W/m.K)	Average directional heat flux (W/m ²)	U value (W/m ² .K)
Arbitrary value	10000	362.78	0.2729
Arbitrary value	7500	362.41	0.2728
Arbitrary value	5000	361.80	0.2726
Arbitrary value	2500	360.42	0.2721
Arbitrary value	1000	357.35	0.2711
Arbitrary value	750	355.89	0.2705
Arbitrary value	500	353.19	0.2696
Copper, C10100, hard	396.7	351.21	0.2689
Arbitrary value	300	348.26	0.2679
Arbitrary value	200	342.57	0.2659
Arbitrary value	100	327.19	0.2606
Structural steel	60.5	309.61	0.2545
Carbon steel 1020, annealed	54.1	304.78	0.2528
Low alloy steel, 4140	43.33	294.08	0.2491
Arbitrary value	30	273.00	0.2418
Arbitrary value	20	245.04	0.2321
Stainless steel 316	14.58	220.37	0.2235
Arbitrary value	10	188.87	0.2126
Arbitrary value	9	179.89	0.2094
Arbitrary value	8	169.87	0.2060
Titanium alloy, Ti-6Al-4V	7.187	160.80	0.2028
Concrete	2.933	92.30	0.1790
Arbitrary value	1	39.31	0.1606
Arbitrary value	0.95	37.60	0.1600
Arbitrary value	0.9	35.86	0.1594
HDPE	0.4811	20.39	0.1541
Arbitrary value	0.01	4.52	0.1485

MyCurveFit Beta (2020) by MyAssays Ltd. was used to generate a curve for the data. The equation describing the relationship between thermal conductivity, λ and U value, U is:

$$U = 0.2725669 + \frac{-0.1250619}{(1 + (\lambda/9.278186)^{0.9529071})}$$

This fit has an R² value of 0.9999

Solving for λ , where $U \leq 0.16 \text{ W/m}^2\cdot\text{K}$ gives $\lambda \leq 0.924 \text{ W/m}\cdot\text{K}$

This means that the chosen material for the support must have a thermal conductivity of $0.924 \text{ W/m}\cdot\text{K}$ or less. One such material is HDPE, although other plastics such as ABS, PA6, PET and PVC also have satisfactory thermal conductivities, typically between 0.15 and $0.5 \text{ W/m}\cdot\text{K}$.

5.8. Recommendations/Design Optimisation

With analysis of the collection of thermal results obtained, some design optimisations can be recommended regarding the thermal response. Firstly, it can be demonstrated in the results of the thermal stress tests that the thermal stresses and deformations induced from the standard temperatures do not demonstrate a significant risk to the component's ability to operate, with resulting magnitudes of stress not approaching the yield stress by any close margin. Thus, the thermal expansion of the standard Steel applied to the component can be disregarded.

However, the results demonstrated from the application of different materials showed interesting results regarding the overall thermal performance of the component. The main objective of the component, in a thermal regard, is to minimise thermal conduction as much as possible, such that as much heat is retained in the rooms below the loft. Thus, from analysing the temperature differential trends, in Figure 60, it can be noted that some material options performed better than the current Steel. The material performances of Stainless Steel 316, Low Alloy Steel and Carbon Steel showed a better demonstration of heat retention from the bottom saddle to the top of the rod. The order in which these materials were ranked was Stainless Steel 316 showing the best heat retention, followed by Low Alloy Steel and finally Carbon Steel. Thus, these options could be suitable for application in the manufacture of the component, with the use of Stainless Steel 316 being the optimal choice. However, with better thermal performances comes a trade-off regarding mechanical performance. Therefore, this is at the discretion of the company as to what properties they want to be prioritised.

It is important to note that the simulations indicate that the current design is not suitable for use in ceiling loft insulation, due to high thermal conductance resulting in U values significantly above those allowed by building regulations. The thermal conductance of metals is too high to allow for a thermal transmittance below $0.16 \text{ W/m}^2\cdot\text{K}$ (for reference, structural steel is around 300 times more conductive than wood). Simulating plastics such as HDPE shows their suitability from a heat transfer perspective, although mechanical analysis would be required to judge their overall suitability.

6. Concluding Statement and Suggestions of Further Work

The mechanical simulations show that the current design can withstand significant loading per component leg that would more than meet the loading criteria applied in a loft space. Furthermore, with analysis performed regarding the assessment of the loading results of the component implemented in an array, as in industry, it could withstand even further total loading with the overall weight distributed throughout the components in the array. However, results demonstrated from the bending moment simulations showed a significant dip in performance relative to centralised orthogonal loading conditions. The bending moment results showed factor of safety falling below required levels at a fraction of the ideal loading conditions. Thus, this is an area that must be subject to further research and physical testing. The bending moment simulation performed in this report demonstrates an extreme case of loading condition, in which concentrated point loads are applied offset from the central axis of the rod. In the realistic case the weight will be more evenly distributed due to the loft floor above the component and timber, as well as the

timber being supported by an array of components. However, this simulation was still useful in seeing the relation between the mechanical capabilities of the component when subject to compression and bending, highlighting the need for further bending investigation.

With regards to the thermal aspects of the work carried out, the simulations showed that the steel utilised in the component currently does not perform sufficiently. Physical thermal testing should be carried out to verify the suitability of the design as it is possible that the simulated model has limitations stemming from either lack of detail or issues such as meshing anomalies. If physical thermal tests yield similar data to what has been simulated, then the mechanical properties of plastics should be investigated to judge their viability for use in the support. Simulation results demonstrated the better performance regarding temperature difference throughout the component to be lesser in magnitude with the utilisation of other steel types. A highlighted material for the usage in this component, showing the best heat retention and good practicality for application in this scenario, being Stainless Steel 316. This material application would improve heat retention of the rooms below, as well as performing marginally better from a mechanical standpoint comparative to the currently steel utilised. However, further work could be completed with the simulations already created with a greater range of materials such to potentially discover even more suitable applications to the component.

In conclusion, the desired data requested by the company have been provided in this report and provided a good basis for physical testing to proceed. The component is mechanically sufficient as the design stands, and would operate safely in loft space conditions, whilst offering the uniqueness in design of addressing unevenness in loft flooring. However, further improvements could be made, and these have been highlighted as a result in the report recommendations and further work.

7. Reflection

Team management was required to progress through the project. This involved continuous organisation of tasks within the group. A meeting with the company was established on 02/03/2021 to discuss the background of the company and the deliverables of the project and thus an agenda could be created. In addition to the company meeting, a supervisor meeting was conducted to relay the information over from the company to ensure a full understanding of the problem statement.

Social media platforms were used between team members for communication. This allowed discussion of the project outside working hours if necessary. Microsoft Teams was used to share the work between group members throughout the project so that the work could be reviewed and any issues that arose could be addressed.

Upon further meetings, a Gantt chart was developed as in Appendix C – Gantt Chart. This was to structure and organise the project. As the project was focused on thermal and mechanical aspects of the product, the team was split into smaller groups to address each aspect. Two people would be researching and analysing the mechanical aspects and the other three would perform the thermal research and analysis of the product.

The team had worked effectively and efficiently allowing all the deliverables set by the company to be completed and even establish some further targets such as identifying the effect of bending stresses to the product. It was agreed between the group and the company that the material data would be obtained for research however, due to no reply from the company, the material data was never retrieved thus a

general material (structural steel) was used in the simulations to understand the extent of performance of the loft support.

8. References

Azo Materials, n.d. *E-Glass Fibre*. [Online]

Available at: <https://www.azom.com/properties.aspx?ArticleID=764>

[Accessed 9 March 2021].

Boarding, U. L., 2020. *LOFT-E Leg Calculator 2020*, Cumbria: s.n.

Evergreen Energy, n.d. *Loft Insulation, The Complete Guide to Types & Costs*. [Online]

Available at: <https://www.evergreenenergy.co.uk/insulation/loft-insulation-guide/>

[Accessed 9 March 2021].

OVO Energy, 2020. *The Ultimate Guide to Roof and Loft Insulation*. [Online]

Available at: <https://www.ovoenergy.com/guides/energy-guides/the-ultimate-guide-to-roof-and-loft-insulation.html>

[Accessed 9 March 2021].

Roofing Superstore, n.d. *How to Board a Loft*. [Online]

Available at: <https://www.roofingsuperstore.co.uk/help-and-advice/project-guides/pitched-roofing/how-to-board-a-loft/#:~:text=4.,in%20damp%2C%20mould%20and%20rot>

[Accessed 9 March 2021].

S. M. Cramer, O. M. F. R. H. W. G. S., 2003. *Mechanical Properties of Gypsum Board at Elevated Temperatures*. [Online]

Available at: <https://www.fpl.fs.fed.us/documnts/pdf2003/crame03a.pdf>

[Accessed 9 March 2021].

The Engineering ToolBox, n.d. *Thermal Expansion - Stress and Force*. [Online]

Available at: https://www.engineeringtoolbox.com/stress-restricting-thermal-expansion-d_1756.html

[Accessed 10 March 2021].

The Greenage, 2013. *Getting To Grips with U-Values*. [Online]

Available at: <https://www.thegreenage.co.uk/getting-to-grips-with-u-values/>

[Accessed 9 March 2021].

The Physics Hypertextbook, n.d. *Thermal Expansion*. [Online]

Available at: <https://physics.info/expansion/summary.shtml>

[Accessed 10 March 2021].

Tidewater Insulators, 2014. *How does Fibreglass Insulation Work?*. [Online]

Available at: <https://www.tidewaterinsulators.com/blog/how-does-fiberglass-work>

[Accessed 9 March 2021].

Total Materia, n.d. *Steel Properties*. [Online]

Available at: <https://www.totalmateria.com/page.aspx?ID=steelproperties&LN=EN>

[Accessed 9 March 2021].

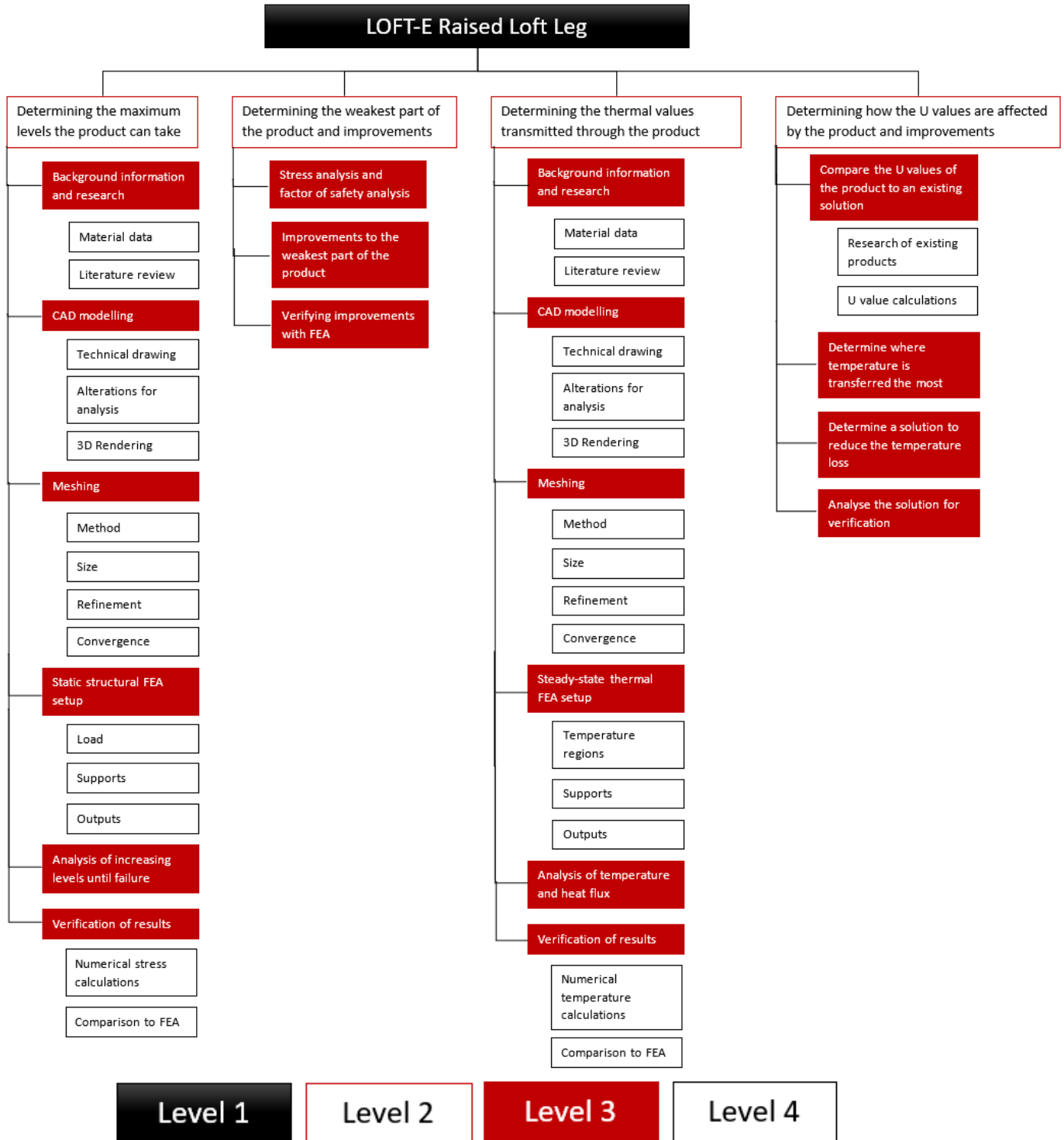
Tubecon, n.d. *Mechanical Properties of Steel*. [Online]

Available at: <http://www.tubecon.co.za/en/technical-info/tubecon-wiki/mechanical-properties-of->

[common-steel.html](#)

[Accessed 9 March 2021].

Appendix B – Work Breakdown Structure



Appendix C – Gantt Chart



LOFT-E raised loft leg strength, stress, and thermal simulation tests

HARRISON BEAUMONT, COLE CHESTERTON, MACKENZIE CLARK, NAEEM KHAN, GREG WRAY

1

Topics to Be Covered

CAD Replication

Mechanical Analysis

- Yield Stress
- Stability
- Bending

Thermal Analysis

- Loft Section
- Thermal Expansion
- Material Testing

Recommendations

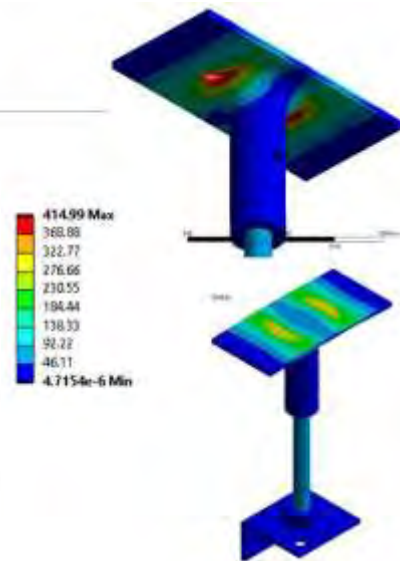
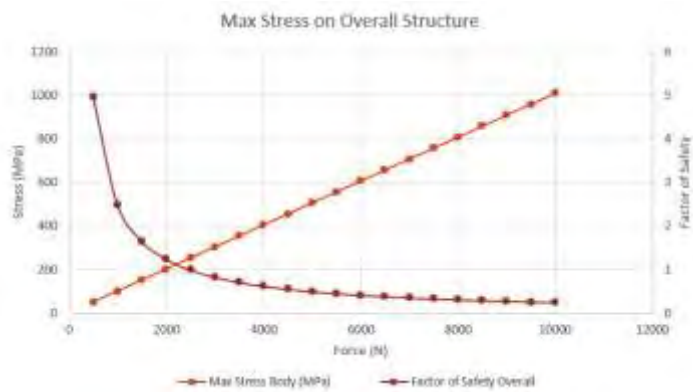
2

CAD Replication



5

Yield Stress Analysis



6

Loading of An Array



With a factor of safety of 2 a single leg is capable of holding 126.3kg

Meaning an array of 6 legs over a 4x4 foot area can hold 757.8kg

7

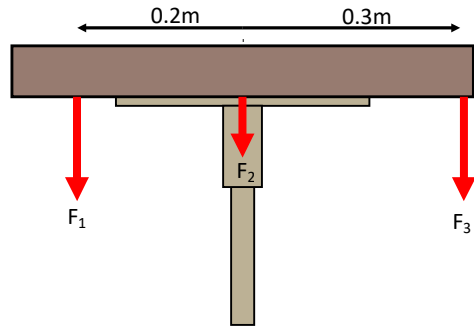
Stability Analysis

- Will the rod buckle under loading?
- The critical buckling load: $P_{cr} = \frac{\pi^2 EI}{L^2}$ was calculated
- The maximum load the rod could withstand prior to buckling
- The critical buckling load was found to be 47386.07N
- Much higher than the load that would result in yielding of the material

8

Stress Due to Bending

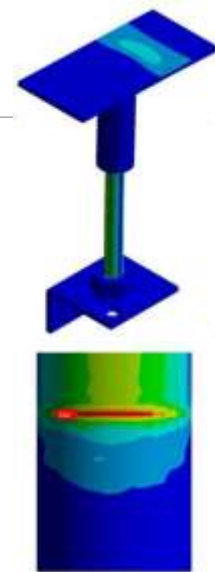
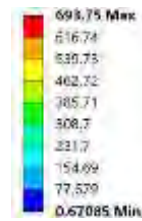
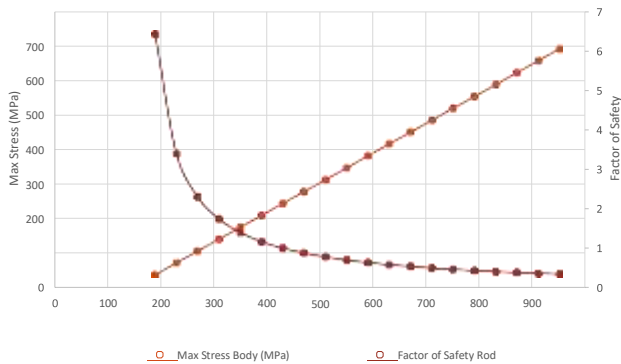
- Could occur when additional loads are applied away from the saddle face
- Weight of the timber
- Additional forces cause moments that increase the stress
- Main focus was the threaded rod



9

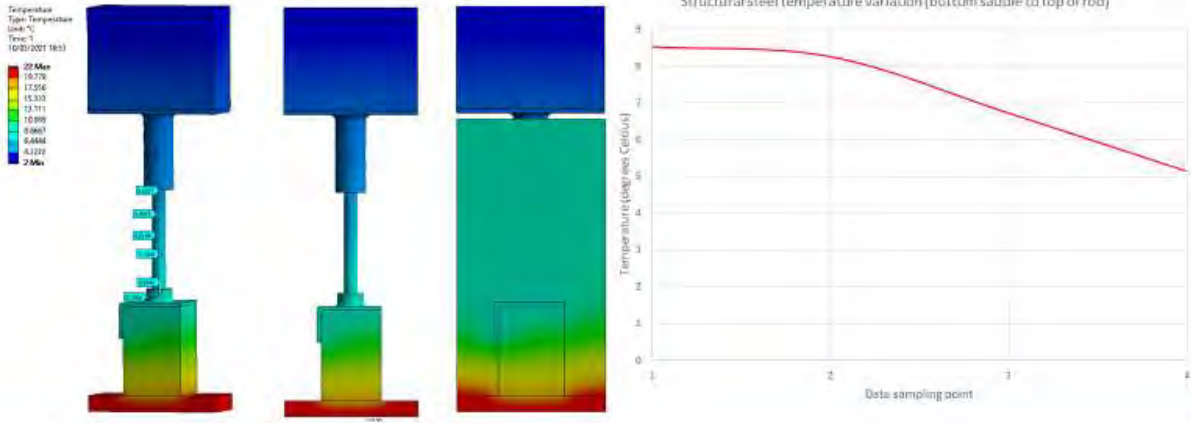
Stress Due to Bending

Maximum Stress Experienced When Uneven Loads Are Applied



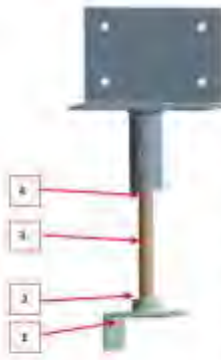
10

Steady State Thermal - Loft Section



11

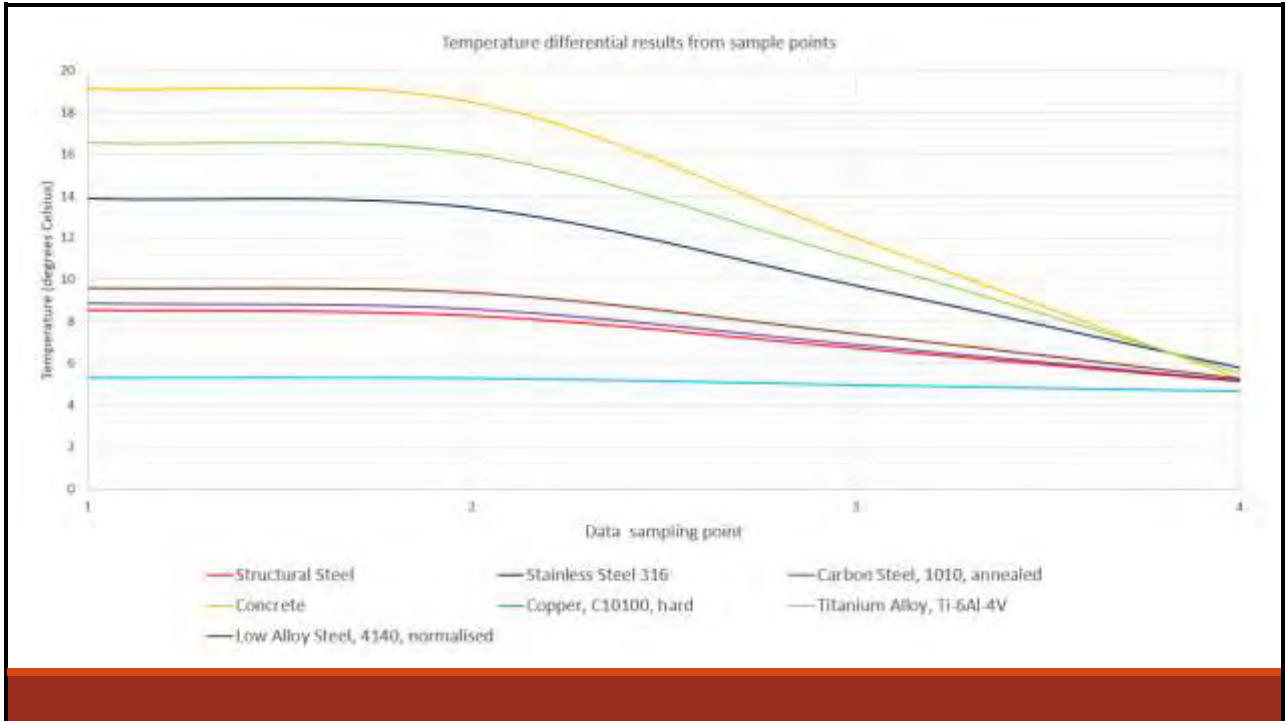
Thermal Material Analysis - 1



- Part Labeling:**
- 1 = Connecting surface of bottom saddle
 - 2 = Top surface of bottom saddle/beginning of rod boundary
 - 3 = Mid length of rod
 - 4 = Top of rod/upper saddle boundary

Material	Data Point			
	1	2	3	4
Structural Steel	8.5373	8.2660	6.7235	5.1379
Stainless Steel 316	13.853	13.427	9.6983	5.7629
Carbon Steel, 1010, annealed	8.8634	8.5879	6.8812	5.1707
Concrete	10.155	18.500	11.086	5.2558
Copper, C10100, hard	5.3215	5.2887	4.9716	4.6734
Titanium Alloy, Ti-6Al-4V	16.566	16.02	11.013	5.538
Low Alloy Steel, 4140, normalized	9.5899	9.367	7.4015	5.2518

12



13

Steady State Thermal – Thermal Expansion

Assuming linear expansion

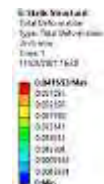
$$\alpha = \frac{1}{L_0} \frac{\Delta L}{\Delta T}$$

$$\epsilon = \frac{\Delta L}{L_0}$$

$$E = \frac{\sigma}{\epsilon}$$

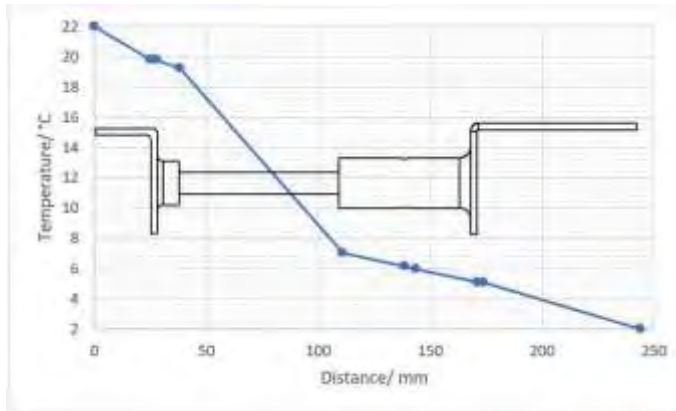
$$\sigma = E \epsilon = E \frac{\Delta L}{L_0}$$

$$\sigma_{dt} = E \alpha \Delta T$$



14

Steady State Thermal – Numerical Calculations



Fourier's law of conduction:

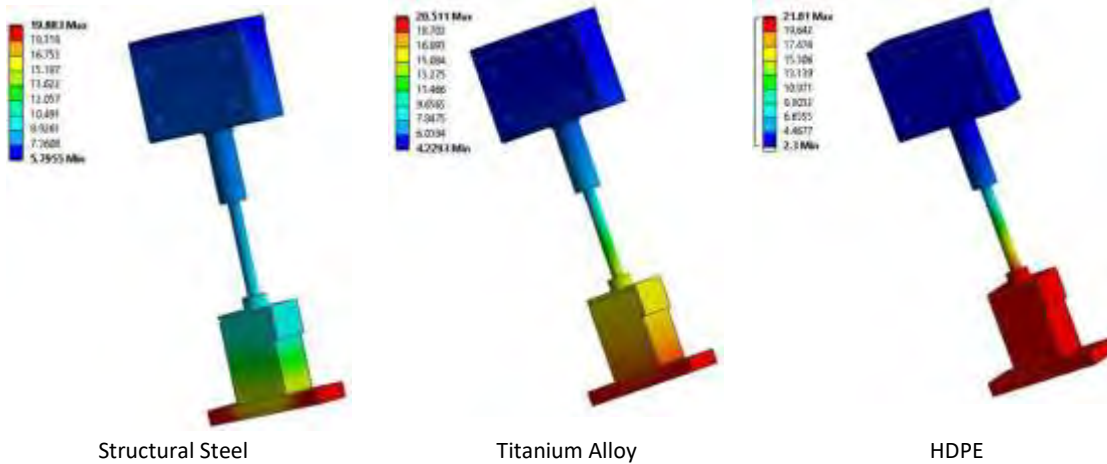
$$\dot{Q} = \frac{\Delta T}{\sum R} \text{ where } R = \frac{x}{kA}$$

As \dot{Q} (heat transfer) is constant:

$$T_2 = T_1 - \dot{Q}R \text{ where } T_2 < T_1$$

15

Steady State Thermal – Conductive Heat Transfer with Ambient Temperatures



Structural Steel

Titanium Alloy

HDPE

16

Thermal Analysis – U values 1

$$U = 1/(R_1+R_2+...)$$

where R_x = thickness of layer/thermal conductivity of layer

$$U = \vec{\phi}_q / T$$

where $\vec{\phi}_q$ = directional heat flux and T = temperature difference

$$\text{Overall } U = (U_1 * A_1 + U_2 * A_2) / (A_1 + A_2)$$

Target U < 0.16 W/m²K

Thermal conductivity for support < 0.95 W/m.K

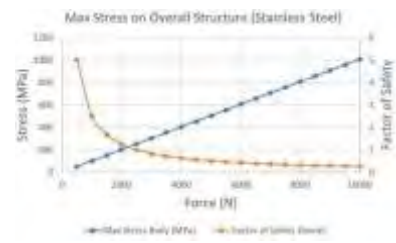
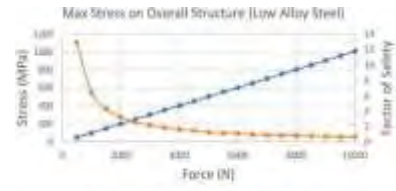
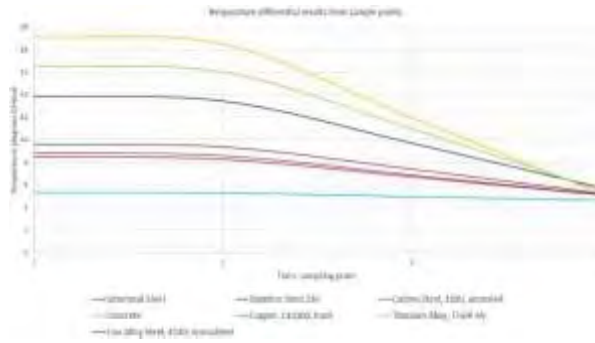
17

Thermal Analysis - U values 2

Material	Average directional heat flux	U value
Structural steel	323.82	0.25941
Stainless steel 316	227.59	0.226
Carbon steel 1020, annealed	318.55	0.25758
Concrete	93.582	0.17947
Copper, C10100, hard	369.46	0.27526
Titanium alloy, Ti-6Al-4V	164.66	0.20415
Low alloy steel, 4140, normalised	306.9	0.25353
HDPE	20.451	0.15407

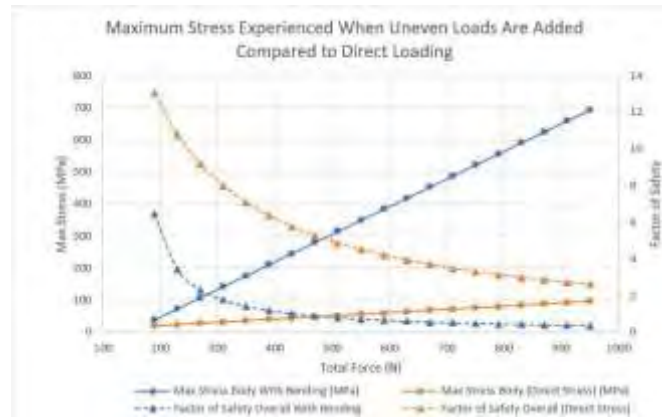
18

Recommendations – Material

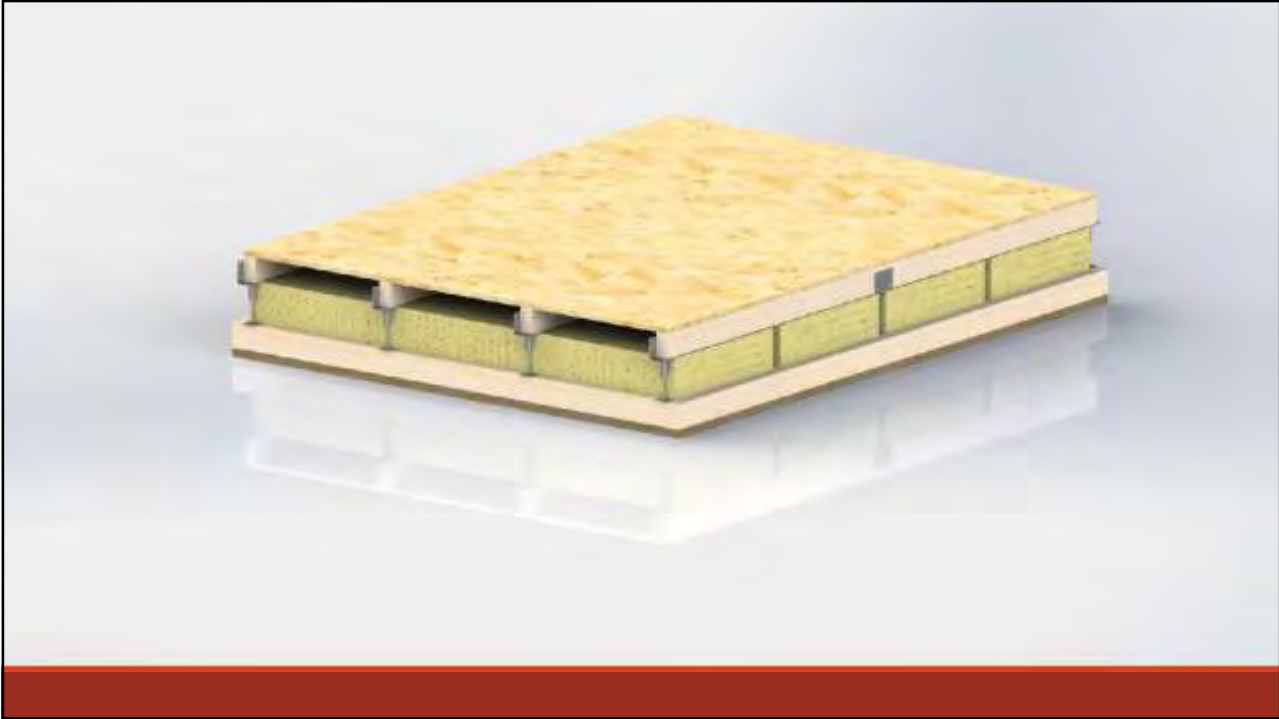


19

Recommendations - Structural



20



21

Appendix E – Initial Meeting Agenda

Introduction:

- Names
- Deliverables

Technical Content:

- Ask for him to run over the brief and his expectations from his perspective
- How is the component utilised (I.e. just for installation of the floor or throughout the loft lifespan)
- Complete run down on how the component is installed
- Clarification on what is meant by the U values mentioned in the brief
- Request for dimensions and materials of component (do they already have the CAD model?)
- Request array set up
- What potential material options are available for thermal analysis?
- Are there any design weak points already identified by yourselves, and as a result any design optimisation ideas already investigated?
- Suggest weak points identified by looking at the component image currently
- Suggest our initial thought process on how we will deliver their targets

Timescales and Organisation:

- Suggest we give daily updates on progress throughout project
- Outline deliverable milestones and estimated dates (excel table with dates showing tasks. From exemplar report)

Project Management:

- Work breakdown structure
- Pugh matrix
- Gantt chart
- Mind mapping